

**INNOVATION AND COMPUTATIONAL MODELING OF
SMALL-SCALE ENERGY HARVESTING WITH
ELECTROMAGNETIC INDUCTION WHILE
CONVERTING ROTATIONAL INPUT TO LINEAR
MOTION WITH A CRANK-SLIDER MECHANISM**

by

Jamshid “James” Farzidayeri

A Dissertation in Partial Fulfillment of the Requirements for the Degree of
Doctor of Philosophy in Computational and Data Science

Middle Tennessee State University

May, 2023

**INNOVATION AND COMPUTATIONAL MODELING OF
SMALL-SCALE ENERGY HARVESTING WITH
ELECTROMAGNETIC INDUCTION WHILE
CONVERTING ROTATIONAL INPUT TO LINEAR
MOTION WITH A CRANK-SLIDER MECHANISM**

by

Jamshid “James” Farzidayeri

Approved by:

Dr. Vishwas Bedekar, Chair

Dr. Joshua Phillips, Member

Dr. William Robertson, Member

Dr. John Wallin, Program Director

DEDICATION

To my beautiful soon-to-be wife, Lisa, who has helped me through this journey every step of the way. Without her optimism, resolution, and proofreading I would have certainly fallen. My friends and loved ones with their support and encouragement. BDH who is sadly no longer with us, Matter, and Z thank you for the great friendship. To my mother, I know you would be proud of me.

ACKNOWLEDGEMENTS

I wish to thank Dr. Vishwas Bedekar, my committee chair, for his patience, innovative ideas, and feedback. Many thanks to Dr. Joshua Phillips, Dr. William Robertson, and Dr. John Wallin for your time, guidance, and expertise during this academic journey. Thank you to Mr. Rick Taylor for your time and craftsmanship.

ABSTRACT

Ambient power sources such as wind and vibrations are resources harvested to provide clean and renewable energy to offset the use of fossil fuels. Experimental energy harvesting from fluid flow, specifically from airflow, is typically restricted to rotational movement combined with a rotor and stator design or a model that periodically strikes a piezoelectric. Alternatively, energy harvesting from mechanical vibrations routinely uses the linear motion of a magnet passing through a coil or vibrating piezoelectric elements. Although wind harvesting is typically relegated to large-scale production, significant research has gone into creating innovative small-scale wind harvesters. The viability of these harvesting mechanisms, both wind and vibration, are highly dependent upon their power density, which is determined by the amount of voltage generated per device or per volume.

Utilizing such an approach, we have designed, developed, and extensively tested rotational to linear harvesting which utilizes a crank-slider mechanism. Our study includes computational modeling utilizing COMSOL, established kinematic and transduction formulas as a method to provide theoretical predictions of the design and validation of our final output. Furthermore, our research highlights the advantages over alternative designs, demonstrating the more consistent and higher average voltage output, lower wind speed operation, and ability to increase output by easily incrementing the number of dynamo cylinders without expanding the overall footprint.

At 0.5 Hz, a single crank-slider generated a voltage of 0.176 V_{pp} with an output power of 0.147 mW, whereas the reference harvester generated 0.14 mW at 1.0 Hz with a

0.432 V_{pp}. A single crank-slider operating at regulated frequencies of 0.5, 1, 2, and 3 Hz, with a stroke length of 50 mm generated continuous power of 0.147, 0.452, 2.00, and 4.48 mW, respectively. When joining two crank-sliders into the V-Twin formation, we found that under ambient wind speeds of 3.4 and 4.1 m/s, with the optimized configuration, in which the coils and loads were both connected in series, the device generated 27.0 and 42.2 mW, respectively.

The multicylinder design incorporates six crank-slider mechanisms into a low profile harvester by modifying the crank portion. This allows the device to output higher power while operating at lower wind speeds. Furthermore, this device included a rectifier to convert from AC to DC, a capacitor to clean the output signal, a 5 V regulator, and a smaller diameter copper wire that allowed for more turns in each coil. Under a regulated low wind speed of 2.4 m/s and across a 305 ohm load, the device had a rotational frequency of 0.76 Hz and a power output of 1.2 mW. At a regulated wind speed of 4.9 m/s the rotational frequency was 7.25 Hz and the output 421.9 mW. Additional tests were performed under real world conditions. First, at a rotational frequency of 6 Hz the device was used to charge a 3.7 V 46 mAh smart watch and a 10,000 mAh 10.5 W power bank charger. The smart watch took approximately 1.4 minutes to charge 1% and the power bank took 1.1 hours. A second real word test was done by placing the device outside in uncontrolled windy conditions. In one scenario, at an average wind speed of 2.39 m/s, the harvester was able to charge the smart watch 1% in approximately 1 hour. The second scenario used a 305 ohm load in wind speeds reaching 10.1 m/s at which point the harvesters output peaked at 1.21 W resulting in a power density of 19.98 W/m³.

TABLE OF CONTENTS

	<i>Page</i>
Acknowledgement	iv
Abstract	v
List of Tables	x
List of Figures	xii
<i>Chapter</i>	
1. Introduction	1
1.1. Motivation	1
1.2. Introduction to Energy Harvesting	2
1.2.1 Small-Scale Energy Harvesting	3
1.2.2 Significance of Energy Harvesting	4
1.2.3 Energy Harvesting Efficiency	5
1.2.4 Vibration and Oscillation	9
1.2.5 Shaping and Interacting Magnetic Fields	10
1.2.6 Modeling Magnetic Fields	12
2. Objectives of Research	14
2.1. Understanding Energy Conversion Using Dynamo Effect	14
2.2. Design of V-Twin Wind Energy Harvester and Analysis	15
2.3. Design of Multicylinder Harvester and Analysis	16
3. Methods of Research	18
3.1. Experiments	18

3.2. Measurement Tools	19
3.2.1 Magnetometer	19
3.2.2 Multimeter	20
3.2.3 Oscilloscope.....	20
3.2.4 Tachometer	22
3.2.5 Anemometer	22
3.2.6 Caliper and Tape measure	22
3.2.7 COMSOL.....	23
3.3. Measurement Analysis.....	23
3.4. Limitations	24
3.5. Preliminary Data and Analysis	24
4. Design of a V-Twin with Crank-Slider Mechanism Wind Energy Harvester	
Using Faraday’s Law of Electromagnetic Induction for Powering Small Scale	
Electronic Devices	30
4.1. Introduction.....	30
4.2. Materials and Methods	40
4.3. Results and Discussion	50
4.3.1 Single Crank-Slider Harvester	50
4.3.2 V-Twin Harvester Utilizing Two Crank-Slider Mechanism	55
4.4. Conclusion	61
5. Multicylinder Harvester	63
5.1. Introduction.....	63
5.2. Materials and Methods	66

5.3. Results and Discussion	80
5.3.1 Output with Single Coil	80
5.3.2 Two Cylinders Compared.....	82
5.3.3 Output with All Six Cylinders	83
5.3.4 Recharging a Device	87
5.4. Comparison to Other Small-Scale Harvesters	89
6. Comparison of Energy Harvesters	91
6.1. Single Crank-Slider Compared to Rotor Stator	91
6.2. Comparable Experimental Harvesters	91
7. Conclusions	93
8. Future Work.....	95
8.1. Improving Output of Each Cylinder	95
8.2. Improving Output by Increasing the Number of Cylinders.....	95
8.3. Design Change Using the Crank-Slider.....	96
8.4. Computational Prediction	96
References	97

LIST OF TABLES

<i>Table</i>	<i>Page</i>
1. Sample COMSOL data from a stationary output.....	28
2. Output of V-Twin harvesters in both series and parallel configuration at 2 Hz. (a) each cylinder and its respective load resistance of $8.2\ \Omega$ were wired in series as units. The resulting total load resistance was $16.4\ \Omega$. (b) the output leads of the right cylinder were interchanged from the system shown in image (a). (c) each cylinder and its respective load resistance of $8.2\ \Omega$ in parallel as units. (d) the output leads of the right cylinder were switched from the system shown in image (c). In (e), each cylinder was wired in series and both loads were wired in series; however, both cylinders were kept in parallel with both loads. In (f), the output leads of the right cylinder were switched with those from the system shown in image (e).	58
3. Harvester wind speed testing comparison.....	61
4. V_{rms} output with oscilloscope under no load and 305 Ohm load at frequencies from 0.5 to 8 Hz	81
5. Comparison of rectified voltage output when incorporating smoothing capacitor at 2 Hz with no load	81
6. Voltage output at 5 Hz under no load. A smoothing capacitor is added to the system to compare with all six cylinders	85

7. Output of harvester with all six cylinders and powered by ambient wind under no load, an optimized load of 305 Ohm, and a non-optimized load of 997 ohm	87
8. Experimental wind harvesters ranked by their power to wind speed ratio from lowest conversion to highest	90
9. Experimental wind harvester's energy density. Fourth column list energy density for the size of the conversion mechanism only, using dimensions given as a guide. Fifth column list energy density for the entire footprint of each device. Due to some dimensional information missing, this column represents our closest approximation for volume.	92

LIST OF FIGURES

<i>Figure</i>	<i>Page</i>
1. Common design of levitation-based harvester where the device vibrates along the z-axis. The Fixed magnets repel the central moving magnet acting as a spring on each end.	7
2. Representation of a magnetic core with an air gap as seen in a study by Zhu et. Al. [16].	7
3. Pen vibration harvester with cross-section view of a pen harvester presented by Bedekar et. Al [18].....	9
4. Measurements for physical components of a sample cylinder magnet with axial magnetized field.	20
5. AC voltage waveforms showing a description of values measured by the oscilloscope.....	21
6. Measurements for dimensions of a coil where the inside diameter is the inside measurement of the coil and not of the coil housing.	22
7. COMSOL representation of three aligned magnets.....	25
8. Sample output from COMSOL with three stationary magnetic fields and no B-Field range limitations	27
9. Sample output from COMSOL with three stationary magnetic fields and with the field limited to enhance the range where a coil may sit around one of the coils.....	27

10. Sample COMSOL 2-D output from Time Variant With no B-Field	
Restrictions	29
11. Example of a common small-scale electromagnetic energy harvester, which typically uses one degree of freedom along the axis of oscillation as a method of harvesting energy using vibrations	35
12. Example of a rotational energy harvester that has the magnets rotating at a radius similar to that of the fan blades [47, 55]. Here, although the magnets are not attached directly to the blades, they still have a significantly large mass spinning at a relatively fast velocity and at a large radius from the axis of rotation	38
13. Example of a rotational energy harvester that has the magnets attached to the fan blades [56-58]. In this design, the mass of the magnets at such an extreme radius has a significant effect on the stability, inertia, and structural integrity of the system	38
14. (a) Front section of the harvester which includes the crank-slider mechanism, along with the reference harvester as indicated in the style presented in Figures 12 and 13. (b) Back section showing the crank-slider mechanism.....	41
15. Crank slider mechanism in which the slider is aligned along the axis of rotation for the crank.....	44
16. Schematic of wind harvesting process	44
17. Sample velocity (\dot{x}) and acceleration (\ddot{x}) of the magnet portion of the crank-slider harvester with ω of 2π , $r = 2.5$ mm, and $l = 222$ mm, using Formulas 22 and 24, respectively [60]......	45

18. Reference turbine-style harvester with magnets attached to the tips (max radius) of the blades and coil attached to the stationary surface, similar to the designs presented by [47, 55].....47
19. COMSOL-generated field based on two N52 axially magnetized disk magnets with a diameter of 25.4 mm and a thickness of 3.175 that are attached for a total thickness of 6.35 mm and a B_r max of 1.48 T along the z-axis, as referenced in Figure 15 and 18. (a) Isometric view with the original boundary conditions of -150 mm to 150 mm used for the data simulation process and theoretical predictions. (b) Emphasis of the field at close proximity to the magnet surface along the ZY plane47
20. A sample of values for B through the coil along the axis of oscillation. The measured values were physically collected using a WT10 Teslameter at the indicated distances. The COMSOL values were extracted from Figure 19 at a distance of 15 mm from the z-axis (the center of the magnet) and along the axis of oscillation extending ± 25 mm from the XY-plane49
21. Representation of the transduction coefficient (Φ) based both the measured and COMSOL prediction values from Figure 20 with the l value for the crank-slider harvester. This image represents a one-half stroke from 0 to π of the crank, which would originate at ± 25 mm and extend to $+25$ mm from the center of the coil.....49
22. Sample of open circuit voltage output from the crank-slider harvester at 1 Hz. These data represent a full stroke of the crank starting at 0 and ending at 2π , which includes 2 passes through the coil. The first pass occurs from 0 to π as

the slider extends. The second pass through the coil occurs when the slider retracts as the crank moves from π to 2π . The measured-theoretical and COMSOL theoretical values were both evaluated using the data generated from Figure 21. The experimental measured values are the physically measured values generated by a RIGOL oscilloscope for each of the data points. All measurements and predictions were evaluated at 1 Hz	50
23. Voltage and power outputs for the crank-slider harvester at 0.5, 1.0, 2.0, and 3.0 Hz. The devices depicted in each Figure (a–d) had a 50 mm stroke length with the coil located at the center of oscillation. The coil had an internal resistance of $8.1\ \Omega$	51
24. Output at 2 Hz across a $8.4\ \Omega$ resistor for the crank-slider harvester vs. the reference harvester, as measured using an RIGOL DS1054 oscilloscope. The crank-slider oscillates across its coil twice for every single pass of the reference harvester. The reference harvester also has a higher peak voltage and a smaller curve area	53
25. Measured peak-to-peak voltage demonstrating that the reference harvester had higher values than the crank-slider harvester at 0.5, 1, 2, and 3 Hz with a $8.4\ \Omega$ load, signifying that the crank-slider harvester would have a greater range of wire gauge available	55
26. Power output demonstrating that the reference harvester had a lower power output than the crank-slider harvester at 0.5, 1, 2, and 3 Hz with a $8.4\ \Omega$ load	56
27. Front (a) and back (b) V-Twin harvester formation	56

28. Wind harvesting process used for multicylinder device	67
29. CAD drawings. Left: Full assembly showing the planned angle between each cylinder. Right: Enhanced view of how the blue arm for cylinder A is fixed in its connection to the crank portion and how all the yellow arms have a point of rotation for their connection to the crank portion	68
30. Actual build. Left: Front view of harvester without the fan portion showing the six cylinders with cylinder A being fixed to the crank portion. The remaining cylinders B, C, D, E, and F have a rotational point connected to the crank portion. Weights attached at different locations to balance the system. Angle θ_{cyl} as the angle between each of the cylinders. Center: Side view showing the pitch of the blade, depth of the total device, coils, location of magnet within each coil, and axis of rotation. Right: Front view with fan attached with fan radius, harvester height and width.....	68
31. Left: Cylinder A demonstrating the fixed connection between the crank adapter and shaft (l_A). Right: Cylinders that are not A. This demonstrates how cylinders B, C, D, E, F, and G have a point of rotation between the primary crank at the axis of rotation as seen in Figures 29, and 30	69
32. Enhanced CAD drawing for the crank portion demonstrating the axis of rotation for cylinder A along with the crank length for cylinder A. This image does not include the crank adapter portion.....	69
33. Crank-slider mechanism for cylinder A with kinematic values for Formulas 37 through 42	70

34. Theoretical COMSOL field estimating one N52 axially magnetized disk magnets with a diameter of 2.54 cm and a thickness of 0.635 cm and a $B_r max$ of 1.48 T along the z-axis	73
35. Comparison of COMSOL theoretical values and physically measured values for Magnetic Flux Density along the Z-axis in a line through the coil and along the axis of oscillation. Values measured with a WT10 Teslameter at the specified distances. COMSOL values gathered from the field in Figure 34 along the XY-plane	73
36. Transduction coefficient (Φ) using theoretical COMSOL values and physically measured values from Figure 35 from the motion of travel for the magnet if it travelled from 0 to π with a crank radius of 2.54 cm	74
37. Crank-slider with crank adapter mechanism for all cylinders other than cylinder A.....	75
38. Minimum and maximum stroke lengths. Top left: maximum distance (x_A) for cylinder A. Bottom left: minimum distance (x_A) for cylinder A. Top right: maximum distance (x) for any cylinder that is not cylinder A. Bottom right: minimum distance (x) for any cylinder that is not cylinder A. In each of these states the crank radius (r) is aligned with the shaft (l) and in the cases of non A cylinder, the crank adapter radius (d) is also in alignment.....	76
39. Oscilloscope output for cylinder A with an additional cylinder B demonstrating the same output with a 60 degrees phase difference	77
40. Rectifier with smoothing capacitor and 5V regulator	78

41. Oscilloscope output for a single cylinder with full bridge rectifier and no smoothing capacitor	79
42. Oscilloscope output for single cylinder with rectifier and smoothing capacitor. Top Left: 10 nF smoothing capacitor, Top Right: 220 nF smoothing capacitor, Bottom Left: 4.7 μ F smoothing capacitor, Bottom Right: 47 μ F smoothing capacitor	79
43. Voltage and power output for a single harvester coil at 1, 3, 5, and 7 Hz. The coil has an internal resistance of 308 Ohms. The test loads ranged from 10.46 to 1792 Ohms. The stroke length of 5 cm from Figures 32, 33, and 38	80
44. Output of four levels of smoothing capacitor at 2 Hz with no load.....	82
45. Sample outputs of cylinder A and B. Left image shows the 60 degree phase difference with both cylinder outputs in the same orientation. Right image shows the output when cylinder B has its output connections reversed	82
46. Sample outputs of cylinder A and D. Left image shows the overlap of A and D when they are connected in phase due to their physical orientation being 180 degrees as seen in Figures 29 and 30. Right image shows the output when cylinder D has its output connections reversed so it is 180 degrees out of phase with cylinder A	83
47. Sample output at 2 Hz of the outputs for cylinders A, B, and C. Each output has a 60 degree phase difference	84
48. Sample output of all six cylinders together. Dashed lines indicated the in phase alignment for cylinders pairs: A and D, B and E, C and F. Vertical adjustment for	

each output does not represent amplitude. Each output's vertical adjustment is for visual clarity only	84
49. Sample output of all six cylinders under no load. Left image post rectifier at 6 Hz. Right image has 470 μ F smoothing capacitor	85
50. Voltage and power output for six cylinder output, rectifier, and smoothing capacitor over test loads ranging 10 Ohms to 5.6k Ohms and at frequencies 2, 4, 6, and 8 Hz	86
51. Outside wind speeds taken during real world test of device while charging a smart watch. Measurements taken every 10 seconds over 10 minutes. The average, maximum, and minimum wind speeds were 2.39, 5.1 and 0 m/s respectively	89

CHAPTER 1

INTRODUCTION

1.1 Motivation

One of the great difficulties faced while off world is power generation. It is not feasible to transport enough fossil fuels for long-term survival on other planets and there are no reserves awaiting those who arrive. Therefore, any exploration must take with them their own methods of generating power. For example, the earlier Mars rovers *Spirit* and *Opportunity* used approximately 100 W to operate, and their solar panels were able to provide 140 W of power for up to four hours [1]. Unfortunately, as time passes those panels become less efficient due to issues such as dust and they eventually decrease to a power output of 50 W. The newer rover, *Perseverance*, uses a radioisotope thermoelectric power source [2]. However, this too degrades each year with an expected lifetime of 14 years.

Agriculture requires electricity to power equipment such as electric fencing, automated feeding, and heated water sources. If the power grid goes down or a failure within the battery power source, the results are loss of protection, food source, and water access, all of which are detrimental to the crops and livestock. Due to this, many applications combine a battery source in combination with the typical recharging solar panel. However, solar is very dependent upon daytime sun exposure, orientation, and are subject to weather such as hail.

Remote backcountry areas in national parks regularly attract campers, hikers, and adventurers. During these activities, one might find themselves with no access to the

power grid for extended periods while at the same time using electronics such as a cell phone for a light source, emergency contact, and camera. The off-grid weigh stations and campgrounds could provide low power charging stations using either solar or wind for use in emergencies.

With each of these examples, a possible answer is energy harvesting. However, the major issue with selecting only one style of harvester be it solar, wind, or vibration, is when that form of ambient energy is limited for a prolonged period [3, 4]. This begs the question: are there other forms or combinations of power generation that are viable? What if additional innovative and practical energy harvesting technology were available to assist with some of the power needed in situations like space exploration, agriculture, or remote locations?

One available component is to focus on some unique qualities to combine methods of harvesting. It is given that the volume of the coil space restricts the stroke length, and it is expected that a harvester would use the full availability of the space to oscillate. Furthermore, the major space components of a wind harvester are the dimensions of the turbines.

1.2 Introduction to Energy Harvesting

Ambient energy is abundant, natural, and readily available. Its sources can be in the form of nuclear, wind, solar, hydro, thermo, biofuels, and even mechanical vibrations [4]. Society increasingly requires viable alternatives to fossil fuels, with consumers demanding cheaper, cleaner, and efficient sources of energy. Unfortunately, it must be

processed or harvested into electric power so that it can be used in our electronic devices. Some of the more familiar harvesting methods are large wind farms, solar farms, and water dams. The harvesting process for each of these has advantages and disadvantages; most significantly, each of these require a significant amount of investment to be sustainable. Fortunately, their outputs can reach up into the gigawatt range making the process worthwhile. Once established, they are successful in providing energy to communities, which in turn offsets the use of limited fossil fuels.

1.2.1 Small-Scale Energy Harvesting

The methods of small-scale energy harvesting include thermal, solar, and mechanical [4]. For example, self-winding watches use the motion of the human body to wind the mainspring to continually power the device, solar panels recharge batteries for electric fences, and windmills are used to pump water for farm use. This energy providing motion is readily available, not limited by our depleting natural resources, and easily offsets the power consumption used by the device otherwise. This small-scale energy, or power harvesting, is generally considered the collection of energy from external sources to be changed into a usable alternative to power small electronic devices from micro robots to wristwatches [5].

Some areas of research focus on utilizing mechanical energy from available motion, specifically vibrations and oscillations. Vibrations and oscillations can be coupled with piezoelectric, electrostatic, magnetostrictive, and electromagnetic devices to generate electricity [6, 7]. Typically, in energy harvesting, piezoelectric harvesters use an oscillating beam. The vibrations induced on the beam create a strain within the material

and this change in pressure due to strain induces a considerable voltage via the piezoelectric effect. For example, a piezo tile used in energy harvesting devices placed in a person's shoe can generate up to 39 V [8]. Electrostatic devices are also capable of high power output, with up to 549 μW using a 1 cm^2 chip with an acceleration of 0.6 g [9]. One major issue with electrostatic devices is that they require an external voltage source to charge the capacitor necessary for operation. Magnetostrictive harvesters utilize materials whose magnetic properties change when they undergo strain. As the strain varies, magnetic flux occurs and Faraday's Law states that magnetic flux through a conductive coil will induce a current. Like magnetostrictive harvesters, electromagnetic harvesters also utilize magnetic flux and a conductive coil to generate electromotive force. However, electromagnetic harvesters' change in magnetic flux occurs from the coil and permanent magnets changing position relative to each other. Customizing the harvesters allows for the utilization of a variety of frequencies, wavelengths, and orientations. Unfortunately, not all variations provide optimal output.

1.2.2 Significance of Energy Harvesting

With modern technologies, there are some devices that operate at microwatt energy levels, allowing for small amounts of power generated by ambient energy to become a viable commodity [10]. Modern low energy sensors and wearable instruments are capable of operating in the milliwatt range [11]. Innovative experimental energy harvesters that produce up to 42.2 mW, even under low ambience sources, it now possible to utilize them to charge low energy devices [12]. Even slightly reducing the

energy cost of charging the billions of cell phones can dramatically affect the impact of fossil fuel usage.

Additionally, as advancements in smaller more efficient energy harvesting technology progress, this will further expand the list of applications in which they can be utilized.

1.2.3 Energy Harvesting Efficiency

For a harvester to be efficient it must increase the energy per volume. As previously mentioned, electromagnetic harvesters have low voltage while piezoelectric and electrostatic devices have both high voltage and low current [13]. As with all devices, the magnetic field, oscillating orientation, frequency, and magnitude of the vibration are the primary contributors to the effectiveness. One way of improving energy harvesting efficiency is by improving the method of gaining power. A group was able to sufficiently power a 3.3 V sensor using magnetic energy harvested from electric power lines in factories using power conditioning modules [14].

The manufacture of electromagnetic energy harvesters has an impact on the efficiency of the device. Khan and Ahmad analyzed the various constructions and implementations of both piezoelectric and electromagnetic harvesting systems [6]. In their electromagnetic systems, they found neodymium magnets had the highest residual magnetic flux density.

In the study by Shad Roundy with LV Sensors, the efficiency of four types of harvesting devices: electromagnetic, piezoelectric, magnetostrictive, and electrostatic, were all evaluated [7]. The test was to provide a general theory to compare vibration-

based energy harvesters. This study analyzed the maximum transmission coefficient (λ_{\max}) and found it dependent only on the coupling coefficient (k) as seen in Formula 1. Since actual transmission can vary based on load conditions, it was determined that, the system must have a load that maximizes actual transmission to obtain optimal λ_{\max} . In their conclusion, the estimated power density for such devices ranged from 0.5 to 100 mW/cm³ with vibrations of 1 to 10 m/s² and frequencies of 50 to 350 Hz.

$$\lambda_{\max} = \frac{k^2}{4 - 2k^2} \quad (1)$$

Another group analyzed levitation-based energy harvesting by designing a less complex simulation using Simulink and MATLAB [15]. Their study focused on creating a common harvester design similar to the one presented in Figure 1. These styles of harvesters use fixed magnets at each end of the device that are oriented, so they repel the oscillating magnet creating a spring like reaction during vibrations. They determined that by using analytical analysis, it was superior to numerical field analysis when computing the magnetic field. They compared their Simulink simulation with equivalent modeling and were able to closely match the experiments.

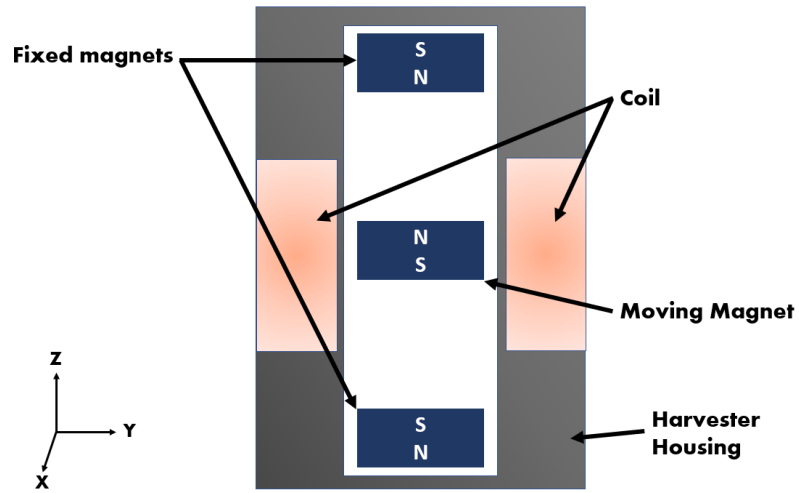


Figure 1: Common design of levitation-based harvester where the device vibrates along the z-axis. The Fixed magnets repel the central moving magnet acting as a spring on each end.

Some areas of study focus on design and improvements of magnetic cores by incorporating air gaps as seen in Figure 2 [16]. Along with testing various air gap widths, Zhou et al. tested three core materials: silicon steel, micro-crystal alloy, and Permalloy. They found that as the air gap increased, the magnetic conductivity would decrease.

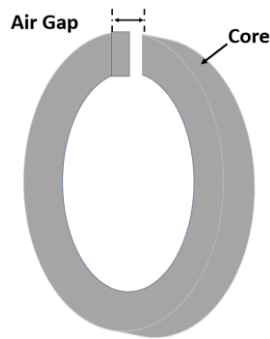


Figure 2: Representation of a magnetic core with an air gap as seen in a study by Zhu et. Al. [16].

A study on the different approaches to achieving self-powered systems using energy harvesting addressed the issue of how the intensity of the magnetic field directly affects the efficiency of energy harvesting [11]. They found that materials with high permeability, such as Metglass, concentrated the magnetic field within the material in an effect called magnetic flux concentration. This resulted in there being a higher magnetic flux density than free space, which would improve the performance of electromagnetic energy harvesting devices.

A group working to optimize the efficiency of harvesters by using a helical core, found the shape of the core had a significant impact on the power output by lengthening the path of magnetic flux [17]. This produced higher flux density and resulted in larger power density.

Bedekar, et al. has explored the topic of oscillating electromagnetic harvester using a Pen Harvester as seen in Figure 3 [18]. In their research, they built and measured the output of the harvester while varying the frequency. There they built a single model; however, they were limited in their ability to introduce multiple variables into their prototype. Similarly, a study by Soares dos Santos, et al. created a non-linear model of an oscillating electromagnetic harvester [15]. Although their modeling is well developed, like Bedekar, et al., they too have not explored how best to optimize their model. It is important to address the issue of optimization so that a working model minimizes input and maximizes output.

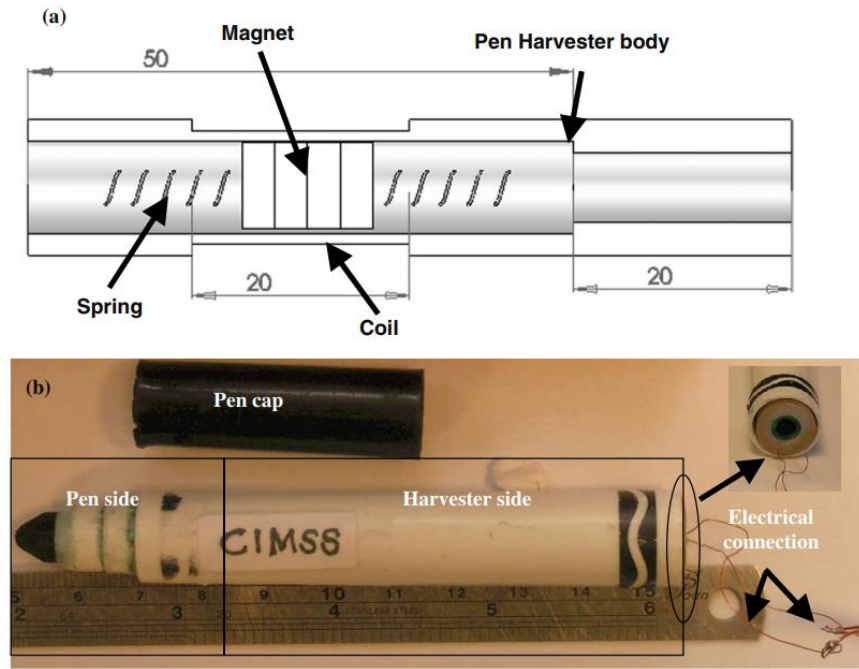


Figure 3: Pen vibration harvester with cross-section view of a pen harvester presented by Bedekar et. Al [18].

1.2.4 Vibration and Oscillation

In this study, it is assumed that the energy harvester's magnet movement is both in alignment with the coil and the direction of motion. Additionally, it is assumed that the stroke length of the harvester maximizes the space allowed. However, it is still critical to examine studies on the various effects oscillation patterns have on a harvester.

Mann and Sims addressed issues with vibration-based energy harvesting systems and the inefficiencies that occur when oscillation frequency does not align with the resonance frequencies of a device [19]. Their solution was to have a tune-able resonance for their device by adjusting the distance between the oscillating center magnet and the two outer magnets that provide the repulsion forces.

Electromagnetic energy harvesting is a promising way to convert mechanical vibration energy into electrical energy at low frequencies that can be easily implemented in practical applications. When finding a design that will produce the most optimized electromagnetic harvester, one problem that arises is the inability to adjust the parameters of a physical prototype: size of magnet, length and diameter of coil, gauge of wire, and frequency. Furthermore, it requires a significant number of resources to produce an optimized physical model of an idea through trial and error. This applies particularly for a system like an electromagnetic harvester that requires copper coils up to the order of thousands of turns. A far more efficient method would be to produce a program that would assist such an experiment where single or multiple variables could be altered without having to produce a physical model.

1.2.5 Shaping and Interacting Magnetic Fields

The shape of a magnetic field can be altered in several methods. In a permanent magnet, the shape and strength of the magnet itself determines how its field behaves. Any nearby changing magnetic fields may either improve or be detrimental to how the harvester operates.

A group of researchers from the University of Denver and the University of Chicago Medical Center utilized magnet and gradient coil systems to improve a uniform magnetic field for in vivo imaging [20]. Although their methods used magnetic coils as opposed to permanent magnets, the theory still applies. Their work allowed for positioning and aligning the four Helmholtz coil pairs to align the z directional component along the axis.

In another study, a three-coil set is used in place of the traditional Helmholtz coil configuration to create uniform magnetic fields [21]. This group was able to generate an area of uniformity six times larger than an equally sized Helmholtz coil. One additional note, during their experiments, any nearby metal objects would disturb the uniformity of the field further signifying the ability and scope of altering magnetic fields.

One group, working with the Sandia's lab, dealt with high magnetic field strengths [22]. However, within their research they outlined the manipulation of magnetic fields to achieve desired flux lines.

A patent by Tu and Yeh addresses losses in electromotive force in linear electric generators caused by the resistance of motion due to the diamagnetic effect [23]. They state that although there are several methods to alter magnetic lines, such as adding permeable materials to the magnet, these methods create complexity and contribute to the diamagnetic effect or are otherwise too expensive or too large to manufacture for portable devices. Their solution was to join magnets in such a way that their poles face each other to form pole structures N-S alternately. From this, they produced a much higher flux density than other similar magnetic arrangements.

In another patent, this one by Günter Ries, a system of magnetic coils produced an alterable magnetic field with five gradients [24]. This set of devices uses the shape of the coil along with certain patterns to allow for contactless control of devices with outside magnetic forces.

As a method to create uniform magnetic fields, one study used a series of hexagonal loops [25]. They modeled their hexagonal coil systems using Biot - Savart's

Law, Maclaurin series, and superposition. They used MATLAB to verify the experiments, which achieved 99% uniformity.

In a paper by Coey, permanent magnet structures are used to create multiple pole fields, gradients, and flux variations [26]. This study addresses the different applications that these arrangements are used in including motors, sensors, separators, and other miscellaneous items. The author concludes by stating that the possibilities of a viable flux permanent magnet source are invaluable.

1.2.6 Modeling Magnetic Fields

A major difficulty in studying magnetic fields is effectively modeling them with a method that is easily evaluated when incorporated with other studies. One way is to use a magnetometer and physically measure each magnet at given points. The issue here is the human error and time it takes to measure enough points for an effective evaluation. Involving time varying fields compounds the problem. Therefore, a thorough investigation requires a computer simulation. There are several ways researchers have developed their models, each with their own strengths and weaknesses.

A study from Sweden developed a model for estimating magnetic fields in complex and noisy environments using a Gaussian Process [27]. Their method estimates the shape of objects by measuring variances in magnetic fields around the object. Using a magnetometer and measuring at randomly spaced locations surrounding an object, they looked for noise within the measurements. The noise was evaluated with fields estimated using a uniformly magnetized sphere, diagonally squared exponential kernels, and their proposed kernel to reproduce a true B-field.

A group studying permanent magnet motors made their calculations using analytical models rather than finite element [28]. This study included analysis of magnetic field density for multiple magnets positioned around a rotor. They were able to include many calculations not typically performed with finite element analysis such as cogging torque, ripple torque, and back-emf form prediction using Formula 2.

$$B_{PM}(\theta) = B_{PMsless}(\theta_2) \cdot \lambda_{rel}(\theta) = B_{PMsless}(\theta - \theta_1) \cdot \lambda_{rel}(\theta) \quad (2)$$

CHAPTER 2

OBJECTIVES OF RESEARCH

2.1 Understanding Energy Conversion Using the Dynamo Effect

The dynamo effect is the process of converting mechanical energy into electrical energy [29, 30]. In this case of this study, mechanical energy is the rotational motion, and electrical energy is produced from a magnet passing through the center of a copper coil of wire. The output of this style of harvesters depends upon several factors:

- Speed of rotation
- Properties of the fan blades as to how efficiently they transfer wind energy into rotation
- Magnet size and strength
- Range of motion as the magnet moves through the coil
- Coil properties including the wire diameter, length of the wire, how close coil is to the moving magnet, and the length and width of the coil

Some additional factors include the internal resistances within the system, such as friction, which includes friction of the magnet within the coil, and housing the friction associated with moving components and bearings, as well as any inertial forces when the fan blade is at a full stop and then begins its initial movement. In our research, we evaluated a single crank-slider then went to two in the V-Twin and six in the multicylinder harvesters as a method of increasing output while restricting the total volume.

2.2 Design of a V-Twin Wind Energy Harvester and Analysis

The purpose of the V-Twin harvester is intended to be low cost, made from readily available materials, have a small footprint, and still be an effective method of way of transferring ambient wind energy at a low speed into usable power for small-scale electronic devices. As a method of keeping costs low, many of the components were either 3D printed, cut from acrylic, or easily sourced. The portions of the device that were 3D printed included the crank, shaft arm, slider, and cylinder housing. The parts that were cut from acrylic material were the front and back of the housing which was bolted together with aluminum and nylon nuts and bolts to avoid any interference with the magnet during operation. The magnets were N52 axial magnetized magnets ordered from K&J Magnetics. The harvester utilizes a single fan as the source of ambient to rotational conversion.

An initial experiment was performed using only a single crank slider mechanism to provide the motion of a magnet through a coil as a method to induce voltage across a load. Once the method was established, the V-two design transferred rotational energy into linear motion by using two sets of crank-slider mechanisms.

While conducting experiments with the V-Twin harvester, two design flaws were observed. First, component failures were experienced where the crank and shaft connect. This portion of the device failed several times during testing and was repaired with adhesive. Second, both cranks were oriented in the same position causing the crank to settle with both cranks in the furthest down position.

A more detailed discussion of the V-Twin harvester is covered in Chapter 4.

2.3 Design of a Multicylinder Harvester and Analysis

As with the V-Twin harvester, the multicylinder is designed to be built with low-cost, readily available materials, and has a small footprint. In addition, the multicylinder harvester was also designed to incorporate real world testing, including converting from AC to DC, smoothing the output, and regulating the output voltage. Although the V-Twin already operated at low wind speeds, the improved design was to operate at even lower wind speeds. Furthermore, as a design improvement on the V-Twin harvester, the multicylinder harvester addressed four significant issues.

First, we improved the power output by increasing the number of turns of the wire within the coil, adding additional cylinders, and decreasing the wire diameter. The design reduced the wire gage from 32 AWG wire to 36 AWG and increased the number of turns from 150 to 2000. The multicylinder increased the number of cylinders used to six total.

Second, the multicylinder resolved the settling issue by modifying the crank mechanism portion so that cylinders are not combined on a single crank location. Instead, each of the cylinders are offset by sixty degrees in a circle around the crank portion. Additionally, a set of weights were added to balance the system so that no point would settle to the lower position.

Third, we reduced the volume of the device by decreasing the depth dimension of the harvester by placing all cranks on the same plane. In previous crank-slider versions, the depth of the device was increased whenever an additional cylinder was added due to each requiring their own crank. However, the addition of the novel modified crank mechanism allowed for all six cylinders in the system to utilize the same crank.

Finally, we increased the durability of the device by changing the material used in critical components. Primarily, the crank material was changed from 3D printed to cut acrylic. The multicylinder harvester did not experience component failure due to breakage during testing.

A more detailed discussion of the multicylinder harvester is covered in Chapter 5.

CHAPTER 3

METHODS OF RESEARCH

3.1 Experiments

The experiments in this research can be broken into three categories: purely theoretical, controlled, and real world. For each experiment, the goal was to evaluate the harvester design for output at various low wind speeds. As a method of providing a variety of results, the parameters in which the experiments are conducted can be manipulated. In this project, we modified various aspects including wind speed, coil dimensions, wire diameter, number of turns, and the magnets' strength, circumference, and diameter.

The theoretical evaluation used the multiphysics software COMSOL in combination with the kinematic formula for crank-slider motion using the dimensions of the physical device to predict the potential output for a harvester with a given set of parameters for coil, magnet, and motion. The theoretical evaluation only evaluated the conversion of rotation to electrical output and did not consider any properties of wind speed, fan shape, friction, or other non-ideal properties. A further discussion on the theoretical prediction is evaluated in Chapter 4.

As a method to measure output under a consistent and regulated environment, controlled experiments were run using a speed-regulated motor to control the rotation of the crank portion in place of a fan. The rotational frequency, voltage output, and load resistances were all physically measured using a tachometer, oscilloscope, and multimeter respectively. Measurements were taken at various low speeds ranging from 1

to 8 Hz depending on the experiment, different configurations including one-, two-, and six-cylinder outputs, and different coil arrangements.

Two real tests were used to evaluate the devices' output under real world conditions. In the first test a household fan generated the ambient wind source. This allowed regulation and measurement of the ambient wind without having gust and direction change. For the second test, the harvester was placed outside in an uncontrolled environment at wind speeds up to 10.1 m/s. The device was less than one meter off the ground and aligned with the wind direction.

3.2 Measurement Tools

A variety of measurement tools were used throughout the research, planning, trials, and experiments during this research process.

3.2.1 Magnetometer

The magnetometer, also referred to as a teslameter or gaussmeter, was used for measuring the strength of the magnetic field. Specifically, this device was used for gathering field strength values at set intervals along the axis of movement for the magnet to both compare the values with the COMSOL predictions and to calculate the theoretical analysis of output for a dynamo style harvester. Additionally, the teslameter was used to verify individual magnet's surface strengths as seen in Figure 4, for comparable uniformity amongst the magnets used as well as for ensuring the correct north and south facing direction of magnets when used in the experiments.

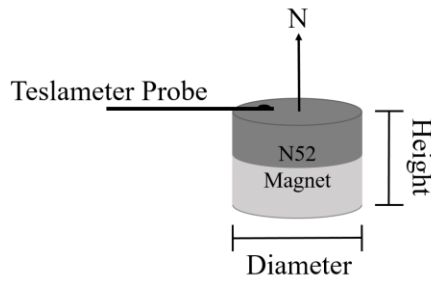


Figure 4: Measurements for physical components of a sample cylinder magnet with axial magnetized field.

3.2.2 Multimeter

This device was used in measuring several electrical characteristics including continuity, resistance, and voltage. Continuity was checked for each of the coils to ensure the copper wire had no breaks or burnouts while performing test. When measuring the resistance, two components were evaluated. The first was the resistance of the copper wire that makes up the coil portion of the harvester. The resistance measured in the copper was then used to compare to the expected resistance given the American Wire Gauge (AWG) and length of the wire. Due to the tolerances within the values of resistors used in the experiments, the second use was to verify the resistance of the load, which was comprised of either a single resistor, resistors in parallel, or in series. When used to measure voltages, the multimeter was used post rectifier to verify the DC voltage output when compared to the oscilloscope values.

3.2.3 Oscilloscope

Although an oscilloscope can measure a variety of electrical properties, in this research it was used to measure max or peak voltage (V_{\max}), peak-to-peak voltage (V_{pp}),

and root-mean-square voltage (V_{rms}) as seen in Figure 5 and Formula 3. When measuring V_{max} , the measured value was used along with a resistor having a known value to determine current through the system. Since V_{rms} is the method of determining equivalent voltages between AC and DC values, the measurements take for V_{rms} were used as a comparison when evaluating comparable DC outputs between these experiments and other similar style experiments.

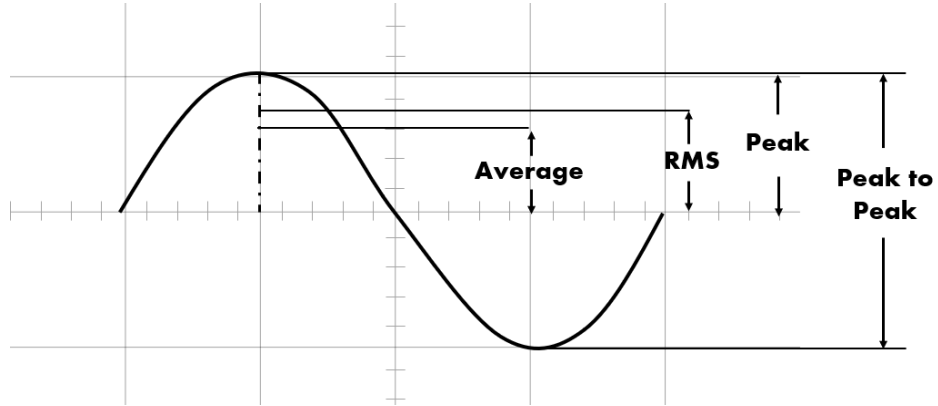


Figure 5: AC voltage waveforms showing a description of values measured by the oscilloscope.

$$V_{rms} = \frac{1}{\sqrt{2}} V_{max} = \frac{1}{2\sqrt{2}} V_{pp} \quad (3)$$

3.2.4 Tachometer

A tachometer was used for measuring the rotational frequency of the crank in revolutions per second (Hz) of both the fan and crank driving mechanism for the various harvesters.

3.2.5 Anemometer

The anemometer was used for the exterior measurement of ambient wind speeds as well as the wind speeds provided by a fan during controlled testing.

3.2.6 Caliper and Tape Measure

The caliper was used for validating dimension measurements for the coil and magnet. After manufacturing and winding the coil manually, the width, inside, and outside diameter were measured and compared to an expected, calculated value as an additional method of verifying the windings as seen in Figure 6. During manufacture of the coil, the length of copper wire was measured. This value was used along with the AWG values for resistance per meter as a check for the total resistance of the wire.

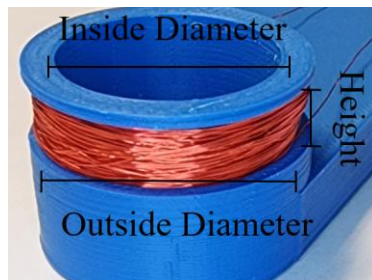


Figure 6: Measurements for dimensions of a coil where the inside diameter is the inside measurement of the coil and not of the coil housing.

3.2.7 COMSOL

For a given magnet or set of magnets, physical dimensions were gathered including diameter, height, and magnetic field strength at the face of the magnet as seen in Figure 4. These values were then used in combination with COMSOL to generate the field values used in calculating theoretical output of the harvester.

3.3 Measurement Analysis

When evaluating the physical properties of the previously listed components, there exists the possibility of a zero amount, therefore those values measured fall within the ratio measurement scale. Multiple measurements of each dimension were taken during the process as a method of validating accuracy during the measuring process, averages were calculated when appropriate. Additionally, when applicable, these measurements were compared to an expected value through either the ordering process or predefined tables. For example, before using one of the magnets, the values measured by the teslameter during the experiment were compared to website specifications along with the spatial dimensions from the caliper. Another example, when measuring the resistance of the coil with the multimeter, the value was compared to a theoretical value using the measured length of the wire and the AWG specifications for resistance per unit length. Finally, averages were taken in situations such as using the anemometer for wind speeds around the harvester. In such cases, multiple measurements were taken at various points across the plane of rotation for the fan blades and the average value was used.

3.4 Limitations

The devices used in these studies were not ISO/IEC 17025 calibrated. Each physical measurement was restricted to the precision and accuracy of the measuring device as delivered. Only a single measuring device was used in each tool category.

3.5 Preliminary Data and Analysis

The first step in this study is to observe how a limited number of magnetic field sources interact. This was done using COMSOL Stationary set up with the 'Magnetic Fields, No Current Interface'. In order to represent a physical experiment, this step used an air space and three objects representing axially magnetized cylinder magnets with a diameter of 19.05 mm and height of 6.35 mm as seen in Figure 7. The three magnets stay in line along the x-axis with the outer two magnets spaced 50.8 mm center to center from the central magnet. The outer two magnets are varied in height along the z-axis, which represents how the fields would appear if the central magnet were oscillating through the outer magnet's fields. The area surrounding the three magnets is assigned a material with a relative permeability of one representing the airspace.

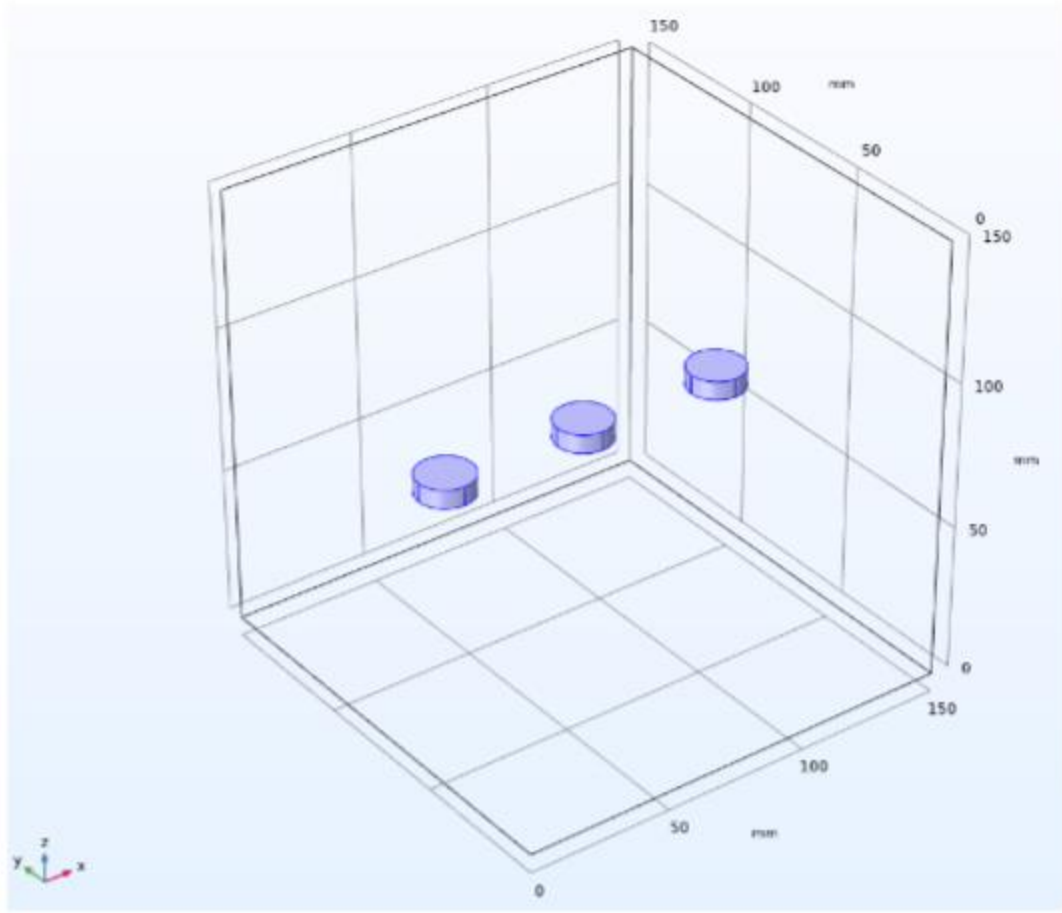


Figure 7: COMSOL representation of three aligned magnets.

The three magnets are assigned properties using Magnetic Flux Conservation. Formula 4 represents the magnetization model used for the remanent flux density. The recoil permeability μ_{rec} is assigned from the material. The remanent flux density norm $||\mathbf{B}_r||$ is user defined and set to 0.350 T, which closely represents the available permanent magnets that will be used in the physical experiment. Since the purpose of this portion of the experiment is to only observe how the fields interact, the magnetic fields are all held at constant values. Remanent flux direction \mathbf{e} for the center magnet is set to

positive z direction. However, the outer two magnets will have their direction set in both the positive and negative z direction in order to observe the difference in magnetic fields.

$$\mathbf{B} = \mu_0 \mu_{rec} \mathbf{H} \mathbf{B}_r, \quad \mathbf{B}_r = ||\mathbf{B}_r|| \frac{\mathbf{e}}{||\mathbf{e}||} \quad 4$$

This shows no input on magnetic flux when having nearby stationary magnetic. In our research, we focused on energy conversion using Faradays' Law as part of various harvester designs.

A sample output for magnetic flux density norm seen in Figure 8 is a slice along the zx-plane. In Figure 9, the range of the field is limited to enhance the critical areas where a coil might be placed.

The raw data can be extracted from the simulation as seen in Table 1. This data can further be evaluated for areas that are more specific. For example, when evaluating the theoretical output of a harvester, we can remove all unneeded information and only plot the data that represents the magnetic field at a point where a coil would be.

In addition to stationary analysis of magnetic fields, COMSOL can also evaluate time variant fields by using the Time Dependent Solver along with selecting AC/DC Magnetic Fields. In the time variant simulation, the build is created around a central axis where each of the geometries are rotated. Figure 10 is a sample output after assigning a Relative Permeability μ_r from material as seen in Formula 5.

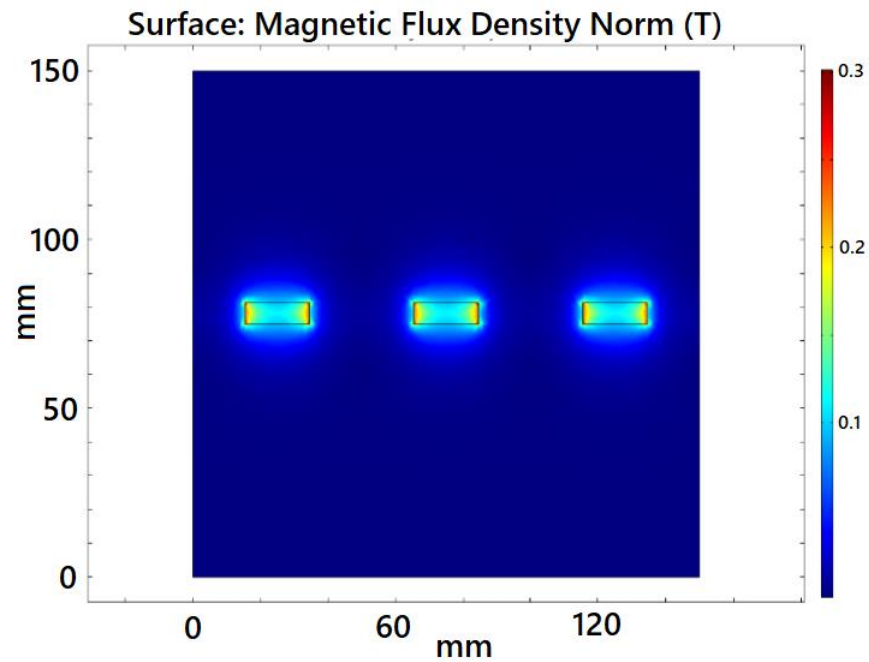


Figure 8: Sample output from COMSOL with three stationary magnetic fields and no B-Field range limitations.

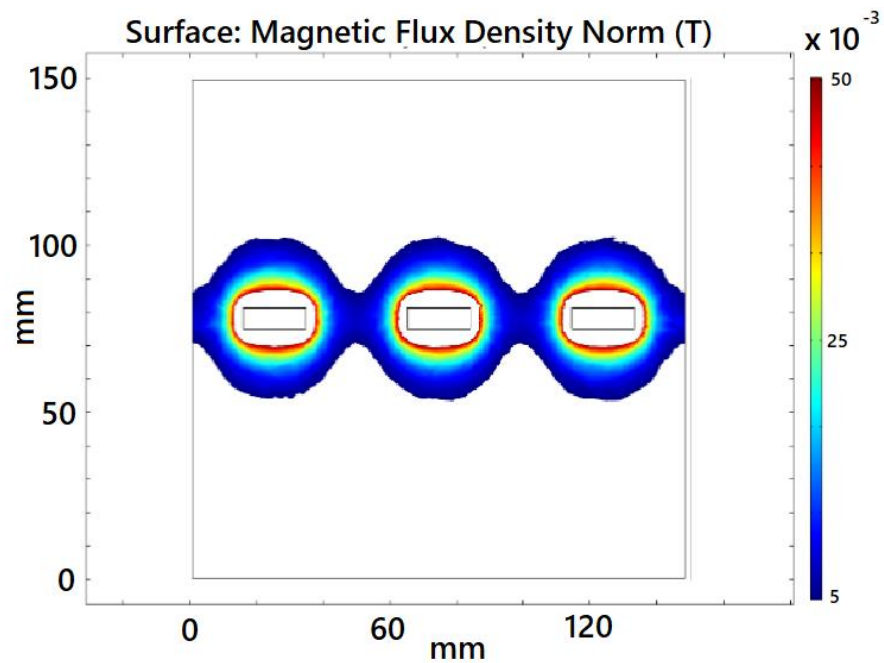


Figure 9: Sample output from COMSOL with three stationary magnetic fields and with the field limited to enhance the range where a coil may sit around one of the coils.

Table 1: Sample COMSOL data from a stationary output.

Model:	three cylinder magnets	pointing pos zaxis inline.mph
Version:	COMSOL	5.6.0.341
Date:	Apr 1 2021, 14:57	
Dimension:	2	
Nodes:	19664	
Expressions:	1	
Description:	Surface	
cpl4x	cpl4y	Color
15.170762695327841	76.84254782153741	0.11605544696954112
15.170762695327841	76.45451205001908	0.12415591656187275
15.266443439313534	76.46252660201188	0.12773814720646007
15.266443439313537	76.96213502907773	0.11800527512374395
...
...

$$\mathbf{B} = \mu_0 \mu_r \mathbf{H} \quad (5)$$

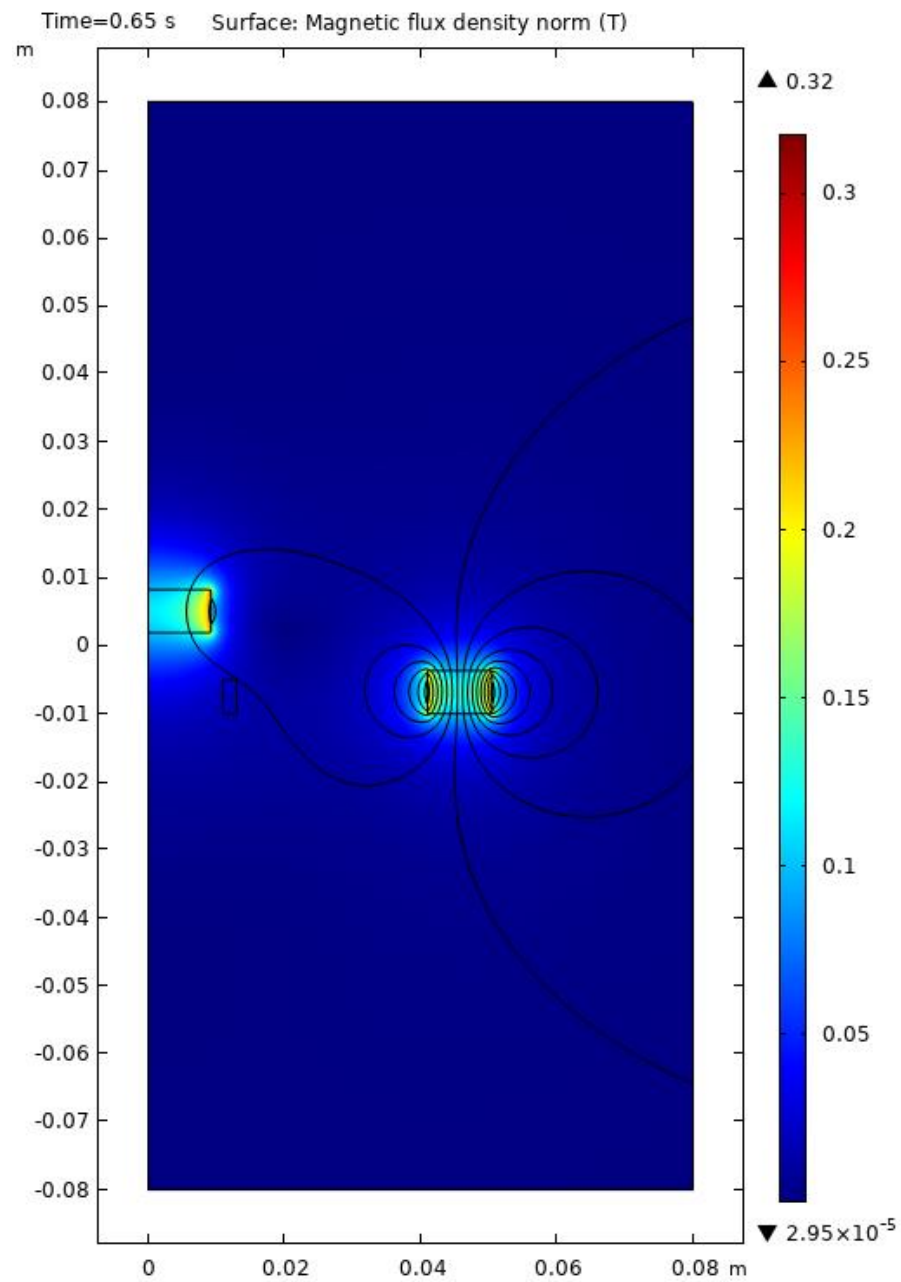


Figure 10: Sample COMSOL 2-D output from Time Variant With no B-Field Restrictions.

CHAPTER 4

DESIGN OF A V-TWIN WITH CRANK-SLIDER MECHANISM WIND ENERGY HARVESTER USING FARADAY’S LAW OF ELECTROMAGNETIC INDUCTION FOR POWERING SMALL SCALE ELECTRONIC DEVICES

This section is taken from our paper submitted to Energies in 2022 with nominal changes to chapter, formula, table, and reference numbers and to remove repeated information.

4.1 Introduction

The quantity of electronic devices used in our everyday interactions creates a significant demand for electrical power. However, that power comes at a cost, be it monetary, pollution, radiation, or resource depletion. Since 1950, the volume of retail sales of US electricity has increased from 0.3 trillion kWh to 4.0 trillion kWh [31]. A major concern is whether civilization will be able to globally sustain this rate of consumption. Current estimates suggest that the world’s oil reserves may last for only the next 50 years [32]. This limited supply of resources has pushed society to look towards alternative and innovative methods of developing usable energy. The most common large-scale energy alternatives used today are nuclear, wind, solar, hydro, thermo, and bio-fuels. Each of these alternatives has its own benefits and drawbacks. One of the major

limitations of each of these is the scope and scale in which they are viable. These listed alternatives require a significant investment in order to be sustainable but their outputs can reach the gigawatt range.

Although power can and is harvested from the previously mentioned alternative sources in order to satisfy the needs of large-scale consumption, there are options available for small-scale devices to harvest their own energy. For example, self-winding watches use the motion of the human body to self-wind the mainspring in order to continually power the device. This energy-providing motion is readily available, not limited by our depleting natural resources, and easily offsets the power consumption that would otherwise be used by the device. A small-scale energy harvesting device is, by definition, a mechanism that converts energy from an external source into useful electric energy that can provide on-board energy solutions to micro-robots, wrist watches, etc. [33]. Several of the options that are readily available to the average consumer have the following shortcomings:

- Wind/hydro/fluid flow: Requires adequate wind speed, orientation, and a very high contact area.
- Solar: Requires ideal conditions with no cloud cover and a proper angle. Additionally, its components have a high decay rate.
- Electromagnetic: Has size requirements and its moving components can experience failure.
- Piezoelectric: Outputs a high voltage with a low current and its moving components can experience failure.

- Vibration/linear: Must be in line with the device, operate at natural resonance for the maximum output, and its moving components can experience failure.
- Rotational: Produces significant forces when the masses rotate at a large radius, has moving components that can experience failure, and is generally associated with fluid flow, which has several additional restrictions (see above).

Electromagnetic energy harvesting is one such small-scale harvesting method that utilizes mechanical vibrations and oscillations coupled with piezoelectric, electrostatic, magnetostrictive, and electromagnetic devices to generate electricity [6, 7, 34]. For example, a piezoelectric tile used in an energy harvesting device placed in a person's shoe can generate up to 39 V [8]. Electrostatic devices are also capable of high power output, obtaining up to 549 μW using a 1 cm^2 chip with an acceleration of 0.6 g [9]. At the current state of development, small-scale devices can range in power consumption from 1 μW for microbots up to 10 mW for wireless sensors and hearing aids [11]. With optimization, there are now energy harvesters that generate over 0.1 mW/cm^3 [35]. Myers et al. designed a small-scale windmill, harvesting 5 mW of continuous power at an average wind speed of 10 miles per hour [34]. Dinulovic et al. developed a rotational electromagnetic harvesting transducer that generated 4 mJ at a load of 10 ohm [36]. Luong et al. used a magnetic force exciter to vibrate a piezocomposite generating element in a small-scale windmill [37]. It was able to charge a 40 mA battery in approximately 3 h using natural wind in an urban area. Wang et al. developed a wind energy harvester that generated high power at a high wind speed of 20.3 m/s [38]. Based on several of these

experimental designs, an energy harvester the size of a shoe box would have the capacity to charge a cell phone which would use approximately 2 W when charging. Considering the fact that there are over 4 billion cell phones in the world, energy harvesters have the potential to dramatically offset the usage of limited resources. A barrel of oil represents approximately 1700 kWh of energy [39]. Assuming that each cell phone user only charged their device once per week for two hours, harvesters would save roughly half a million barrels of oil per year.

Even though energy harvesters do not fulfil the role of providing energy storage, due to improvements in electronics efficiencies, cost, demand, and flexibility [40], they present an interesting option for creating self-powered electronics, emergency energy assistance, supplemental energy, and so on. A long-term and resilient self-powered device that requires little or no maintenance would serve not only to offset resource consumption but would provide devices that fit a variety of unique situations. For example, medical implants and sensors that monitor or assist in human bodily functions would greatly benefit from a long-term alternative to recharging the device externally and periodically by utilizing piezoelectric or similar devices [41]. Additionally, with ongoing expansion in space exploration, there is a potential demand to develop self-powered electronics. Currently, many such devices have focused on solar power dependence [42-44], yet other sources remain widely unexplored for space applications.

Although the abovementioned mechanisms, such as the piezoelectric effect, the magnetoelectric effect, and magnetostriction, can utilize mechanical vibrations or mechanical energy and convert that into electrical energy [34, 45, 46], the actual power output and efficiency of these devices is much lower compared to the energy

requirements of electronic devices (on the order of several milliwatts) [35, 47, 48].

Hence, in order to harvest high power at lower frequencies, inductive energy harvesting becomes a more reliable solution. Of all the vibration-based electromagnetic harvesters, perhaps one of the most common and simplest is the permanent magnet and coil configuration, which is a linear harvester, as shown in Figure 11. In this arrangement, a coil experiences a changing magnetic field resulting from an oscillating permanent magnet. It is well known from Faraday's law that electromotive force (ε) is effected by the number of coils (N) in a changing magnetic flux (Φ) over a change in time (t), as seen in Formula 6. When keeping the volume of the coil space constant, ε can be increased by decreasing the diameter of the wire gauge, which in turn increases the number of turns of the coil. Additionally, increasing the frequency of oscillation also increases ε . Finally, improving $\Delta\Phi$ will also increase the output of the harvester. An advantage of this type of harvester is that it can also be easily magnetically coupled or even have its dampening tuned to increase the overall output [48, 49].

$$\varepsilon = -N \frac{\Delta\Phi}{\Delta t} \quad (6)$$

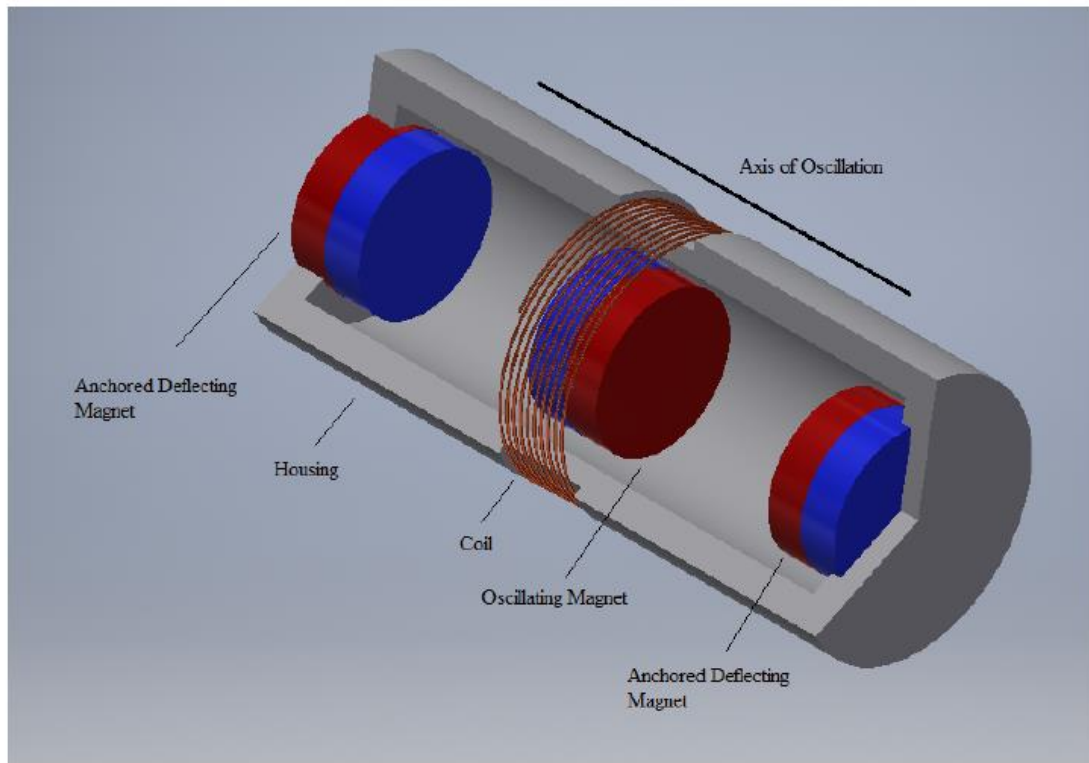


Figure 11: Example of a common small-scale electromagnetic energy harvester, which typically uses one degree of freedom along the axis of oscillation as a method of harvesting energy using vibrations.

Magnetism and magnetic materials have been studied for several centuries for their unique properties and applications. Using Faraday's law of induction, an electromotive force is generated when an electrical conductor is subjected to a changing magnetic field. Several studies have been carried out to investigate energy generation using electromagnetic induction from a variety of sources, such as mechanical vibrations, fluid flow, wind, and mechanical movement. In this study, we investigated the conversion of small-scale rotational energy into electricity using Faraday's law of electromagnetic induction by incorporating a crank-slider design with a linear electromagnetic energy

harvesting system. We believe that the energy generated by such a device can be used for powering small-scale electronic devices.

Researchers are continually exploring several additional styles of experimental harvesting devices. One such design, which uses the typical magnet and coil configuration, is the swing-magnet type, which is used in harvesting bicycle vibrations [50]. Another more common and established configuration of energy harvesting is the previously mentioned large-scale harvesting systems using turbine-style harvesters with wind or water. The most common and recognizable wind harvesters are the large two- and three-bladed versions of the horizontal-axis wind turbines (HAWT) [51, 52] generally seen in large wind farms. Similarly to how an airplane flies, these systems use aerodynamic lift to turn the blades to rotate a shaft that turns the generator [53]. With this type of system, the blades, shaft, and generator are all aligned on the same axis of rotation along the central hub holding the blades and through the generator [52, 53].

One of the major uncertainties associated with these HAWT-style systems, or any similar-style harvester, is where to locate the magnets and coils required for electromagnetic harvesting. A rotating object is subject to significant forces (F_c) that are directly proportional to the location of mass (m) and the square of the velocity (V) at the point of rotation, as shown in Formula 7. Furthermore, as shown in Formula 8, the inertia (I) is also greatly affected by the location of mass (m). Therefore, attaching a dense material such as a neodymium magnet or a copper coil with densities of approximately 7300 kg/m^3 and 8920 kg/m^3 , respectively, as part of the spinning blades would be unfavorable compared to the commonly used carbon epoxy composite or graphite epoxy composite, which have respective densities of 1446.2 kg/m^3 and 1580 kg/m^3 [54].

$$F_c = m \frac{V^2}{r} \quad (7)$$

$$I = mr^2 \quad (8)$$

Some novel smaller designs have attempted to attach the magnets as part of the blades or as separately rotating components at a radius equivalent to the blades. In these designs, presented in Figure 12 and 13, the magnets move about the axis of rotation at some relatively significant radius. Although they are effective, these designs introduce problems with rotational forces and inertia, as presented in Formulas 7 and 8. As a method to further evaluate our proposed crank-slider design, in this paper we construct and analyze a rotor/stator device based on the designs presented in Figure 12 and 13 and refer to it as the reference harvester.

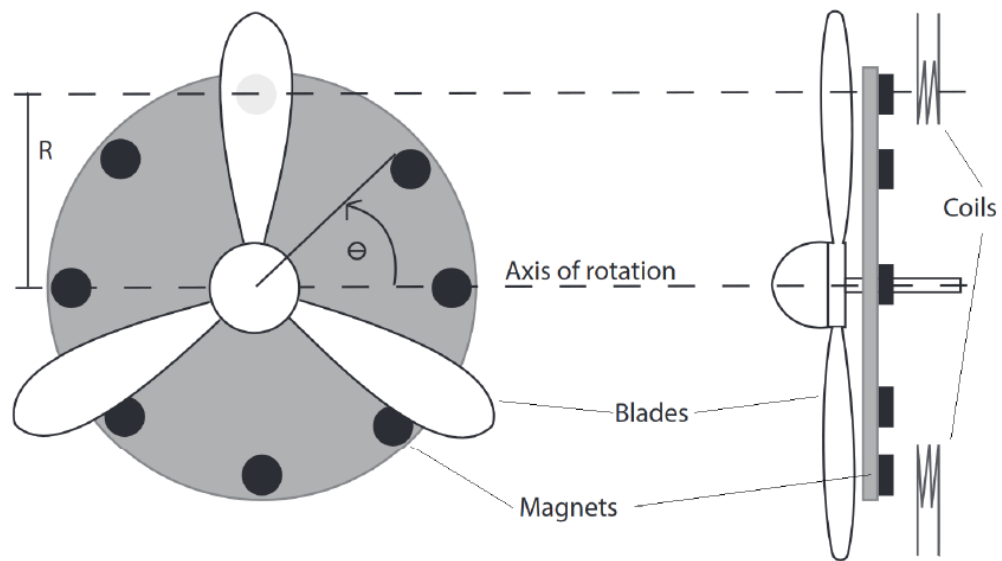


Figure 12: Example of a rotational energy harvester that has the magnets rotating at a radius similar to that of the fan blades [47, 55]. Here, although the magnets are not attached directly to the blades, they still have a significantly large mass spinning at a relatively fast velocity and at a large radius from the axis of rotation.

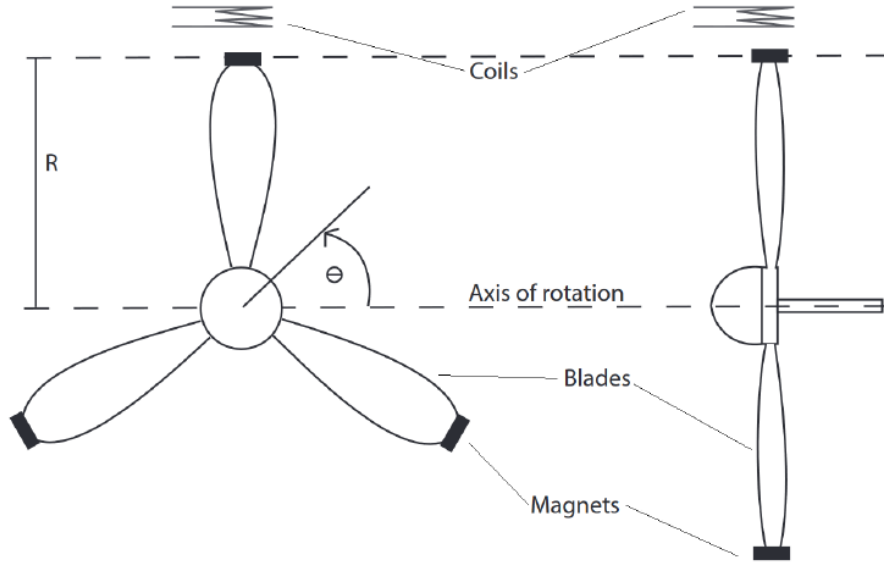


Figure 13: Example of a rotational energy harvester that has the magnets attached to the fan blades [56-58]. In this design, the mass of the magnets at such an extreme radius has a significant effect on the stability, inertia, and structural integrity of the system.

This paper is organized as follows. In the introduction we present a background on electromagnetic harvesters, the need for innovative designs, and the current state of small-scale energy harvesting. In the Section 4.3, we cover the proposed design, the kinematics of a crank-slider, and the design of the reference harvester. Additionally, in the Section 4.3, we discuss the formulas used for the evaluations and theoretical outputs of the design. In this section, the formula and kinematics presented are used in combination with COMSOL Multiphysics software for the simulation and modeling of magnetic fields as a method to generate computer-driven predictions for theoretical

outputs for the system. For further theoretical evaluations, in the Section 4.3 we provide a measured prediction, obtained using a Teslameter to physically gather data from the magnetic field. These data were used as the inputs for the formulas to provide an additional set of theoretical outputs for the system. The Section 4.4 comprises two subsections which separate the single crank-slider harvester topic from the modified V-Twin harvester. The first subsection covers the plots produced by the experimental device, including optimized values for power production for the single crank-slider harvester alone. This subsection also presents a comparison of the crank-slider design with the reference harvester, along with their strengths and weaknesses. The second subsection presents a V-Twin harvester that utilizes two of the crank-slider harvesters. This subsection provides several output arrangements and compares them to obtain the optimal configuration. Finally, in the Section 4.5, we present the reader with a novel expansion of the experimental crank-slider harvester, obtained by modifying the design to include the addition of a second crank-slider in the form of a V-Twin-style harvesting device. The Conclusions include relevant data gathered from the V-Twin harvester, along with its possible applications. The final V-Twin harvester configuration proposed in this study consists of the following:

- A wind harvester that has the capacity to function at low speeds (3.4 m/s);
- A novel way of converting rotational motion to linear motion via a crank-slider mechanism in a harvester;
- A harvester that is easily transported and small-scale;
- A harvester design that can be easily adapted for higher output by adding more crank-slider mechanisms to the system;

- A rotational design that experiences lower detrimental forces on its components compared to similar designs; and
- A configuration that has a comparable power output to other similar devices, without experiencing potentially damaging high peak voltages.

4.2 Materials and Methods

Figure 14 shows the crank-slider harvester prototype, along with a reference harvester similar to the ones presented in Figure 12 and 13. The crank-slider kinematics for the dimensions in Figure 15 are outlined in Formulas 9 through 15. The crank-slider harvester has a crank radius (r) of 25.3 mm, an arm length (l) of 222 mm, and a piston distance (d) of 13.9 mm. Formulas 16 through 19 express the rotational mechanics associated with the experimental reference harvester. The experimental reference harvester has a radius (R) of 192 mm. Both the crank-slider and the reference harvester each have two N52 axially magnetized disk magnets with a diameter of 25.4 mm and a thickness of 3.175 that are attached for a total thickness of 6.35 mm and a B_{rmax} of 1.48 T. Both coils (one for the crank-slider and one for the reference harvester) are composed of coated AWG32 wire, with 150 turns, an inner coil diameter of 29.2 mm, a width of 7.5 mm, a resistance of 8.1 Ω , and a wire length of 14.03 m. In Figure 16, the components included in this device are included within the “Harvester Collection” portion. In order to operate the device, it can be placed on a flat surface and it will operate under wind speeds as low as 3.4 m/s. Furthermore, it can be incorporated with a “conversion and storage” system, which is not included as part of this study, as a method to power or recharge small devices and low-energy sensors and to provide supplemental clean energy.

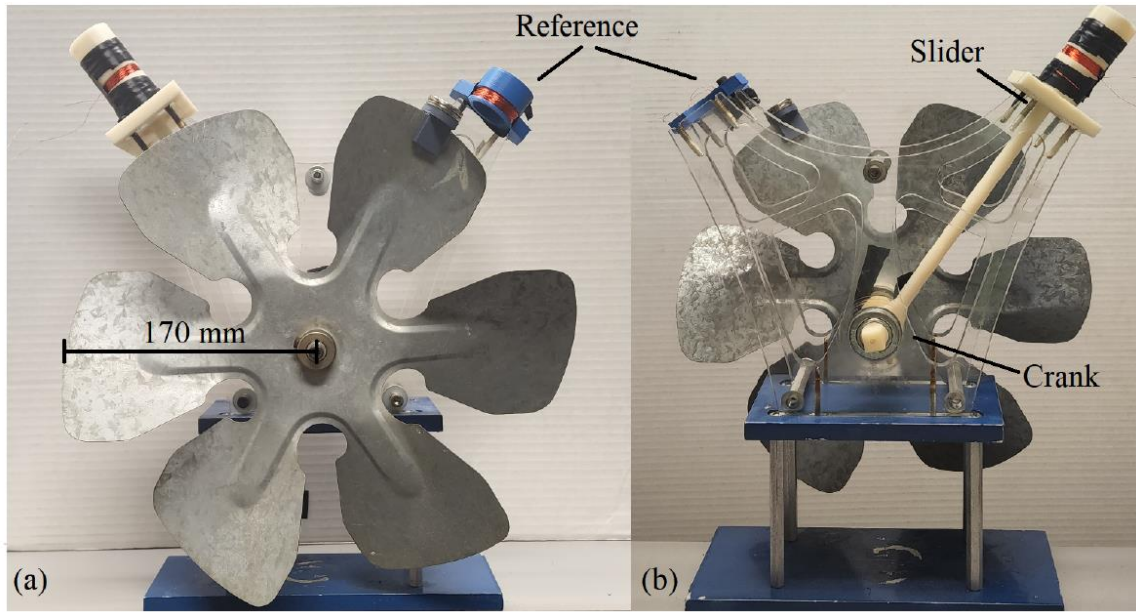


Figure 14: (a) Front section of the harvester which includes the crank-slider mechanism, along with the reference harvester as indicated in the style presented in Figures 12 and 13. (b) Back section showing the crank-slider mechanism.

The kinematic analysis for the magnet attached to the piston of the crank-slider along the axis of oscillation is as follows. The point x in Figure 15 represents where the crank-slider harvester's magnet is in relation to its distance from the axis of rotation from the driving wheel and is represented as x in Formula 9. This does not take into account the position of the coil, which could be theoretically placed anywhere along the travel path of x . It does include the additional mechanical components required to attach the magnet to the slider, which are represented as d , the distance from the center of the magnet along the axis of travel connecting at the point l .

$$x = r\cos(\theta) + \sqrt{l^2 - r^2\sin^2(\theta)} + d \quad (9)$$

The velocity (\dot{x}) of the magnet at point x along the travel path in Figure 15 is represented by Formula 10. As shown in Figure 15, the relation of ϕ and θ is expressed in Formula 11 and rearranged into Formula 12. Using Formula 12, ϕ in Formula 10 is replaced, resulting in Formula 13.

$$\dot{x} = -r\omega \left(\sin(\theta) + \frac{r\sin(2\theta)}{2l\cos(\phi)} \right) \quad (10)$$

$$r\sin(\theta) = l\sin(\phi) \quad (11)$$

$$\cos(\phi) = \sqrt{1 - \left(\frac{r\sin(\theta)}{l} \right)^2} \quad (12)$$

$$\dot{x} = -r\omega \left(\sin(\theta) + \frac{r\sin(2\theta)}{2l \sqrt{1 - \left(\frac{r\sin(\theta)}{l} \right)^2}} \right) \quad (13)$$

In this paper, l will always be assumed to be at least four times greater than r ; therefore, the acceleration (\ddot{x}) of the magnet at point x at along the travel path in Figure 15 can be approximated with Formula 14, here ϕ is no longer a component [59].

$$\ddot{x} = -r\alpha \left(\sin(\theta) + \frac{r\sin(2\theta)}{2l} \right) - r\omega^2 \left(\cos(\theta) + \frac{r\cos(2\theta)}{l} \right) \quad (14)$$

Furthermore, it is assumed that the propulsion of the fan is at a constant velocity in order to evaluate the system. With a constant velocity, the angular acceleration (α) is zero and the first component of Formula 23 can be eliminated, resulting in the reduced Formula 15 [59].

$$\ddot{x} = -r\omega^2 \left(\cos(\theta) + \frac{r\cos(2\theta)}{l} \right) \quad (15)$$

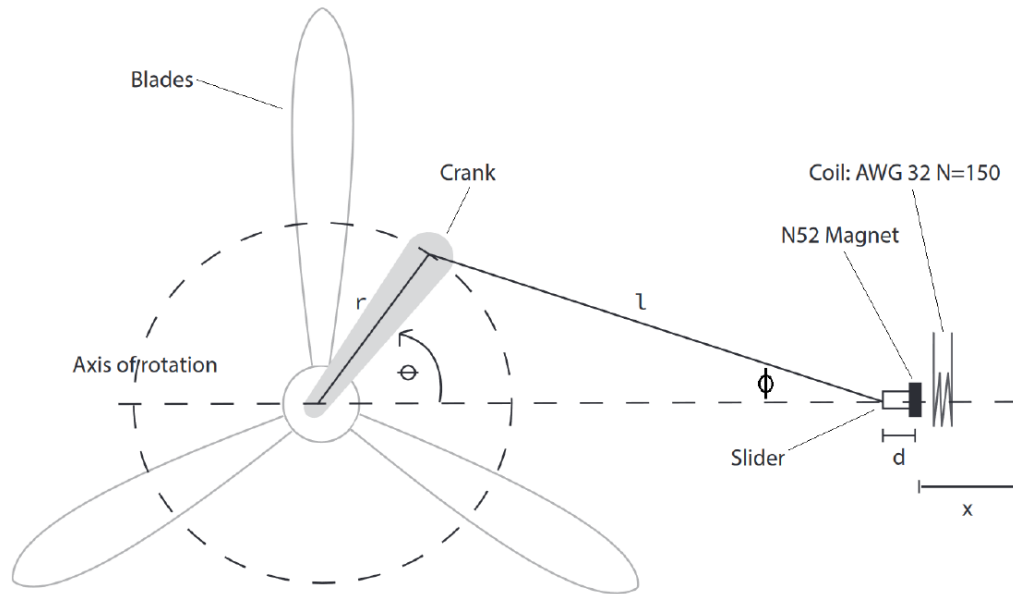


Figure 15: Crank slider mechanism in which the slider is aligned along the axis of rotation for the crank.

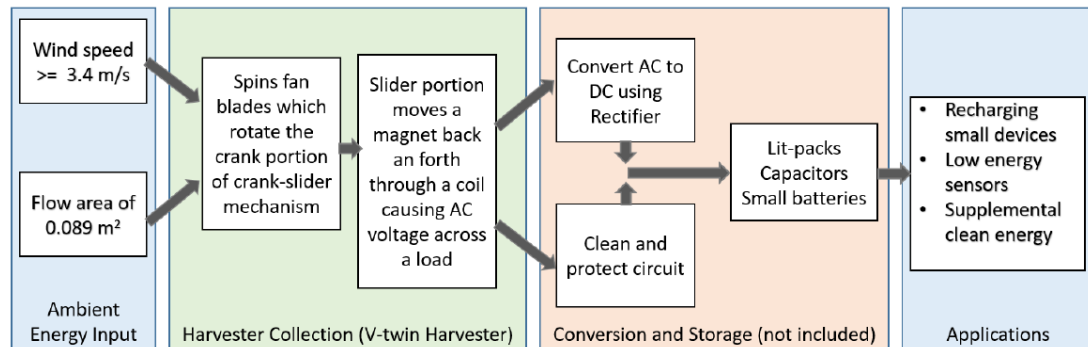


Figure 16: Schematic of wind harvesting process.

Figure 17 is a sample output of \dot{x} from Formula 13 and \ddot{x} from Formula 15 with the given values for ω , r , and l for this experiment. It is significant to note the critical components of motion for the magnet. At θ values equal to 0 or 2π and multiples thereof, the magnet is outside the coil, its \dot{x} is zero, and the magnet is at its minimum and maximum positions relative to the crank. At θ of π , 3π , and their multiples, the magnet's

\dot{x} is zero and this is where the theoretical and experimental central position of the coil is mounted. Additionally, the maximum acceleration of the magnet portion of the crank-slider harvester occurs when θ is 0, where the mechanism is at its elongated maximum, and the magnet is outside the coil.

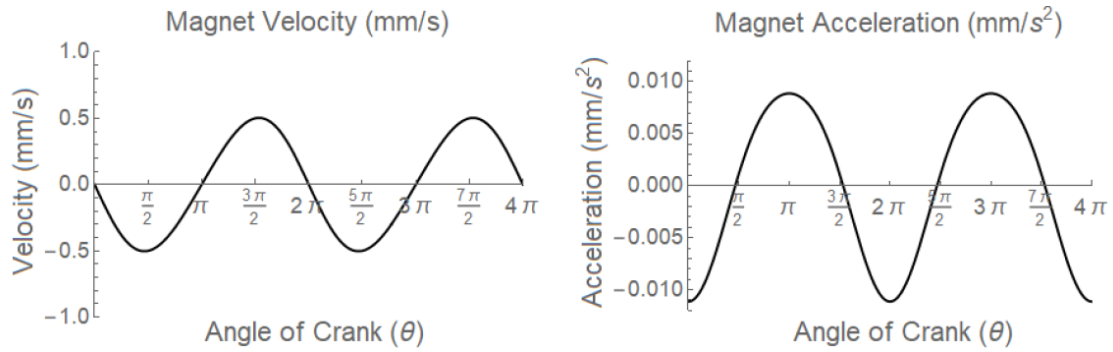


Figure 17: Sample velocity (\dot{x}) and acceleration (\ddot{x}) of the magnet portion of the crank-slider harvester with ω of 2π , $r = 2.5$ mm, and $l = 222$ mm, using Formulas 13 and 15, respectively [60].

An evaluation of magnet's movement when rotating at the circumference of the edge of the fan blade, as shown in Figure 14 and 18, was performed using the following well known formulas. The arc distance traveled (D) by the magnet from the initial position is given in Formula 16. The speed (V) of the magnet in Figure 18, given a uniform circular motion, is represented in Formula 17. The centripetal acceleration (a_c) and force (F_c) on the magnet due to a_c are given in Formulas 18 and 19, respectively.

$$D = R\theta \quad (16)$$

$$V = \omega R \quad (17)$$

$$a_c = \frac{V^2}{R} = R\omega^2 \quad (18)$$

$$F_c = m_{magnet} R\omega^2 = m_{magnet} \frac{V^2}{R} \quad (19)$$

For a crank-slider harvester which utilizes the style presented in Figure 11, the induced voltage (U_v) from the motion of a conductor within a magnetic field (\mathbf{B}) over a length of wire (L) at a velocity (\dot{x}) is shown in Formulas 20, 21 and reduced to 22 [18]. The values for \mathbf{B} are assessed for theoretical analysis in two ways: using the COMSOL values seen in Figure 19 and using the physical readings from a WT10A Teslameter. Those values are plotted in Figure 20.

$$dU_v = (\vec{x} \times \vec{B}) \cdot d\vec{L} \quad (20)$$

$$U_v = \oint (\vec{x} \times \vec{B}) \cdot d\vec{L} \quad (21)$$

$$U_V = BL\dot{x} \quad (22)$$

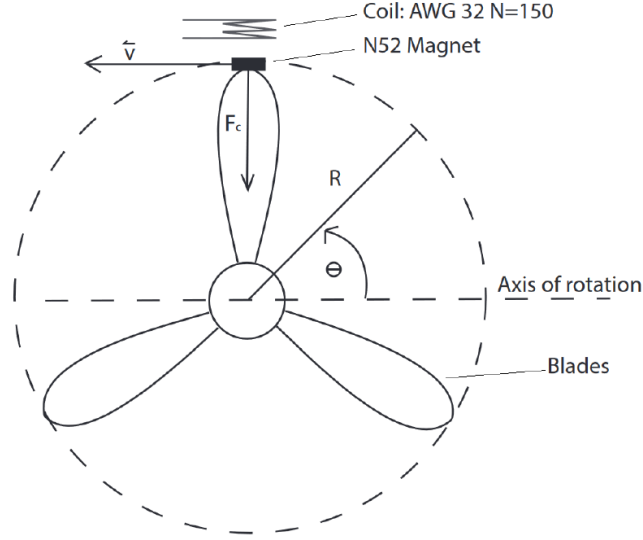


Figure 18: Reference turbine-style harvester with magnets attached to the tips (max radius) of the blades and coil attached to the stationary surface, similar to the designs presented by [47, 55].

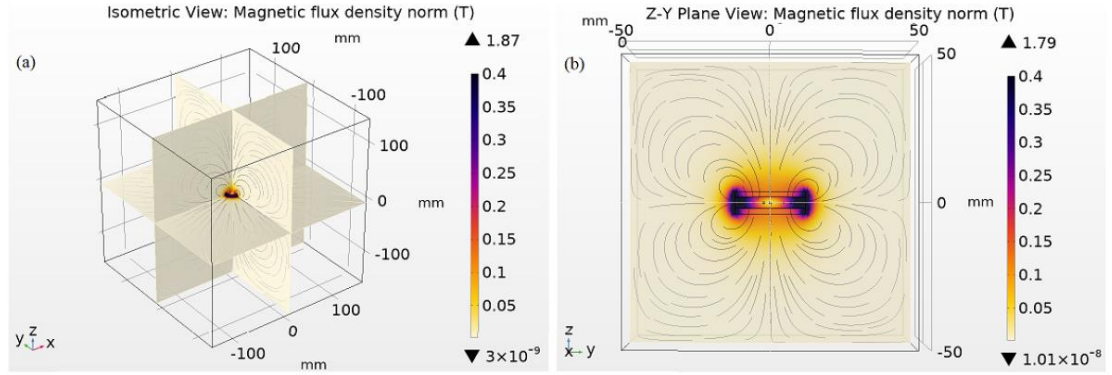


Figure 19: COMSOL-generated field based on two N52 axially magnetized disk magnets with a diameter of 25.4 mm and a thickness of 3.175 that are attached for a total thickness of 6.35 mm and a $B_{r,max}$ of 1.48 T along the z-axis, as referenced in Figure 15 and 18. (a) Isometric view with the original boundary conditions of -150 mm to 150 mm used for the data simulation process and theoretical predictions. (b) Emphasis of the field at close proximity to the magnet surface along the ZY plane.

In Formula 22, BL is also referred to as the transduction coefficient seen in Formula 23 [18]. The values for B from Figure 20 were used to generate Φ in Figure 21.

$$\Phi = BL \quad (23)$$

For the crank-slider harvester, the theoretical voltage is evaluated by replacing \dot{x} in Formula 22 with the non-linear kinematic evaluation presented in Formula 13 and Figure 15, resulting in Formula 24. In Figure 22, the theoretical voltage is represented using Formula 24 and both measured and COMSOL values for Φ from Figure 21 in comparison to the actual voltage, measured using a RIGOL DS1054 oscilloscope.

$$U_V = \Phi r \omega \left(\sin(\theta) + \frac{r \sin(2\theta)}{2l \sqrt{1 - \left(\frac{r \sin(\theta)}{l} \right)^2}} \right) \quad (24)$$

Although Formula 24 does not include the additional characteristics of the system, namely, the resistance, inductance, parasitic dampening (D_p), or number of turns (N), an electrical power system produces maximum power when coil impedance matches load impedance [18, 61]. In Formula 25, the optimal load occurs when the proportionality constant (k) is less than the first term [61].

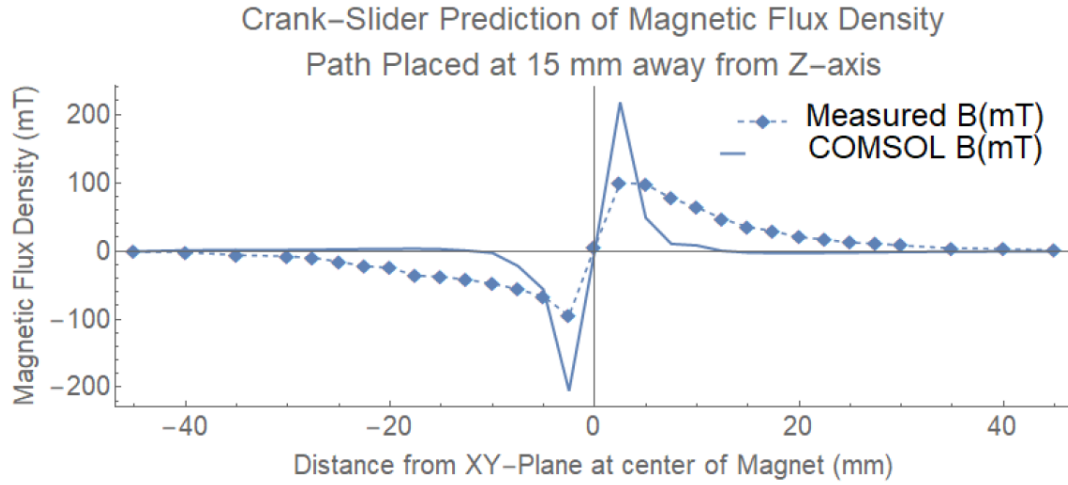


Figure 20: A sample of values for B through the coil along the axis of oscillation. The measured values were physically collected using a WT10 Teslameter at the indicated distances. The COMSOL values were extracted from Figure 19 at a distance of 15 mm from the z -axis (the center of the magnet) and along the axis of oscillation extending ± 25 mm from the XY -plane.

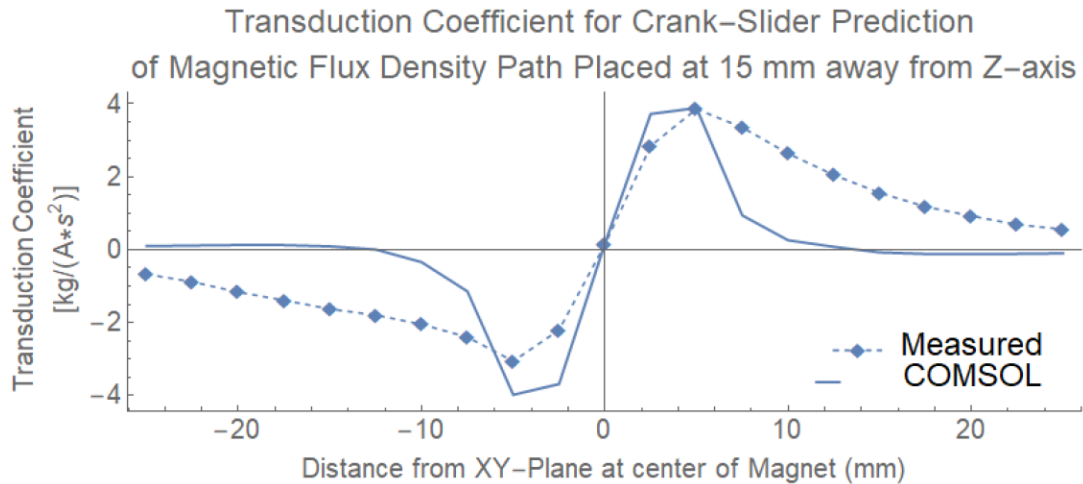


Figure 21: Representation of the transduction coefficient (Φ) based both the measured and COMSOL prediction values from Figure 20 with the l value for the crank-slider harvester. This image represents a one-half stroke from 0 to π of the crank, which would originate at ± 25 mm and extend to $+25$ mm from the center of the coil.

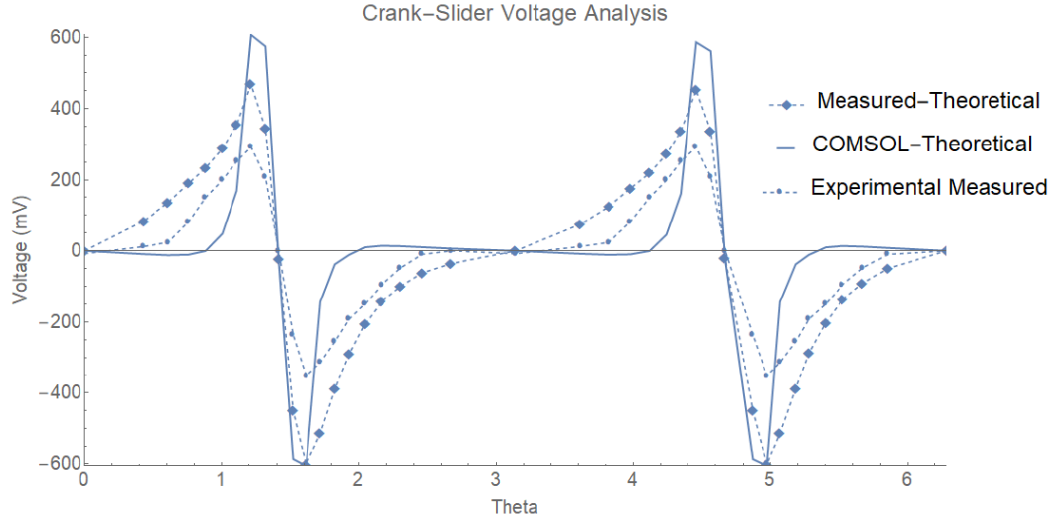


Figure 22: Sample of open circuit voltage output from the crank-slider harvester at 1 Hz. These data represent a full stroke of the crank starting at 0 and ending at 2π , which includes 2 passes through the coil. The first pass occurs from 0 to π as the slider extends. The second pass through the coil occurs when the slider retracts as the crank moves from π to 2π . The measured-theoretical and COMSOL theoretical values were both evaluated using the data generated from Figure 21. The experimental measured values are the physically measured values generated by a RIGOL oscilloscope for each of the data points. All measurements and predictions were evaluated at 1 Hz.

$$R_{optimal} = \left(\frac{1}{D_p} \left(\frac{d\phi}{dx} \right)^2 - k \right) N^2 \quad (25)$$

4.3 Results and Discussion

4.3.1 Single Crank-Slider Harvester

In Figure 12, the actual output of the crank-slider harvester is lower than the theoretical COMSOL and predicted measured values under the outlined conditions. This is typical of many experimental electromagnetic energy harvesters due to a variety of conditions, such as sub-optimal conditions, the exclusion of friction, and parasitic

dampening [18, 61, 62]. The measured experimental voltage and power results for the crank-slider harvester at 0.5, 1, 2, and 3 Hz each with a stroke length of 50 mm are shown in Figure 23. In each of the Figures, the optimal power can be observed around 8 Ω , which is close to the measured resistance of the coil used, and this is consistent with what was predicted [18, 61]. The maximum power produced for the device at regulated frequencies of 0.5 Hz (30 rpm), 1 Hz (60 rpm), Hz (120 rpm), and 3 Hz (180 rpm) were 0.147, 0.452, 2.00, and 4.48 mW, respectively.

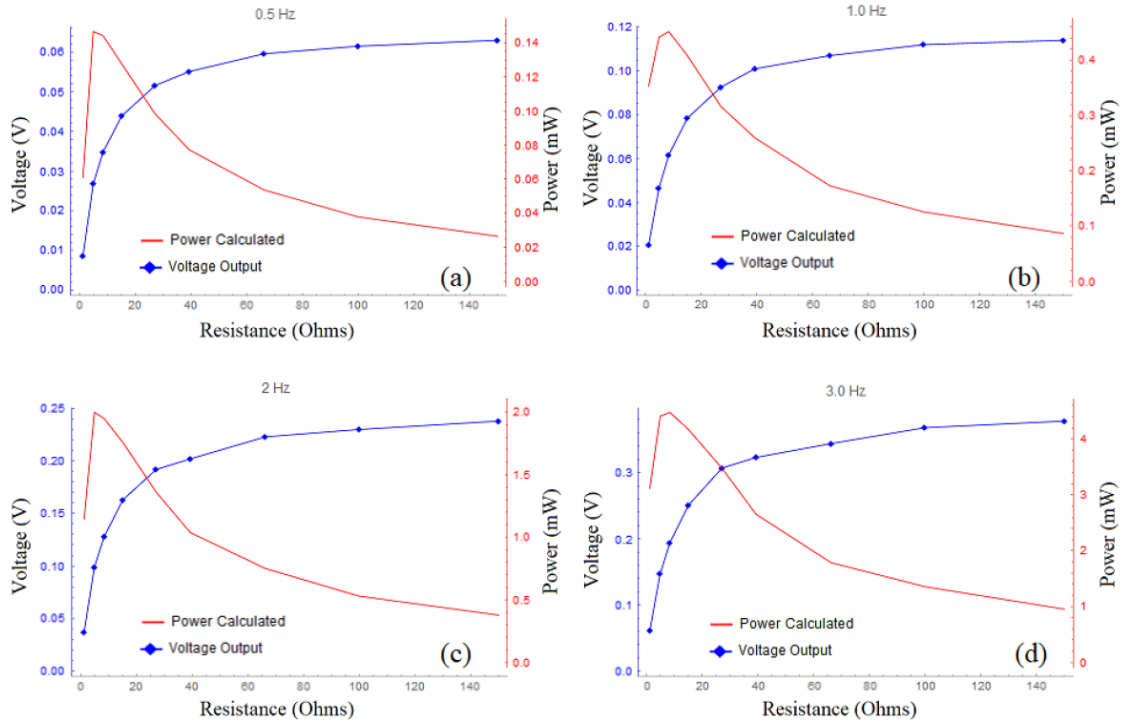


Figure 23: Voltage and power outputs for the crank-slider harvester at 0.5, 1.0, 2.0, and 3.0 Hz. The devices depicted in each Figure (a–d) had a 50 mm stroke length with the coil located at the center of oscillation. The coil had an internal resistance of 8.1 Ω .

The reference harvester was measured under similar conditions in order to analyze how the crank-slider style of harvester compared to the existing experimental harvester techniques shown in Figures 12 and 13 [47, 55-57]. The coil size, wire length, ω , load resistance, and magnet strength of the reference harvester were consistent with the crank-slider during each measurement. The distance R in Figure 18, representing the rotational radius of the rotor's magnet portion in that style of harvester, was measured at 190 mm. In Figure 24, a sample output of the crank-slider was compared to that of the reference harvester at 3 Hz across a load of $8\ \Omega$ to indicate several key factors. First, due to the mechanical nature of the crank-slider mechanism, during each rotation of the driving fan, the stroke cycle of the crank-slider's magnet passes through its coil twice for every single pass the reference harvester makes across its coil, respectively. Second, the peak voltage and peak-to-peak voltage (V_{pp}), and thus the peak current of the reference harvester were significantly higher than those of the crank-slider harvester, as shown in Figure 25. Finally, in Figure 26, while still under all the same conditions, the crank-slider produced more power than the reference harvester. It could be argued that the reference harvester was not optimized to compete against the crank-slider. Therefore, one could evaluate the data in Figure 26 at a point at which both systems had a similar power output. At 0.5 Hz, the crank-slider produced 0.147 mW, which matched the power output of 0.14 mW that the reference harvester generated at 1.0 Hz. At those chosen points, the crank-slider has 0.176 V_{pp} and the reference harvester has 0.432 V_{pp} at a coil resistance of $8.1\ \Omega$, which equates to an instantaneous current of 21.5 mA and 53.3 mA, respectively. One way to improve the output of any harvester is to use a smaller gauge wire with more turns (N) for the coil. These significantly larger voltage and current

spikes on the part of the reference harvester restrict the allowable wire gauges usable for the system. For example, AWG 38 wire has a max current rating of 22.8 mA, which is out of range for use in the reference harvester under these conditions, yet is still usable by the crank-slider design [63].

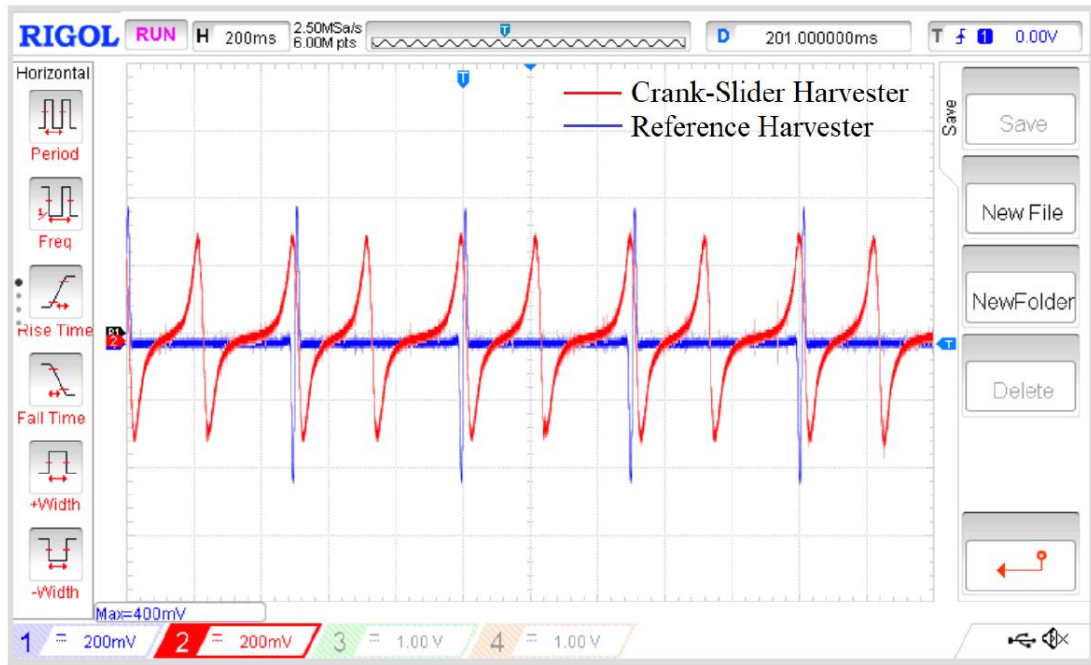


Figure 24: Output at 2 Hz across a $8.4 \, \Omega$ resistor for the crank-slider harvester vs. the reference harvester, as measured using an RIGOL DS1054 oscilloscope. The crank-slider oscillates across its coil twice for every single pass of the reference harvester. The reference harvester also has a higher peak voltage and a smaller curve area.

Finally, due to the previously discussed mass disparity between the very dense neodymium ($7000 \, \text{kg/m}^3$) and much less dense connecting materials, such as the ABS plastic ($1020 \, \text{kg/m}^3$) used, we only compared the forces encountered only by the action of magnet mass measured at 23.57g. This excludes the additional forces of friction, gravity,

and resistance, as well as excluding any masses of the material used to connect the magnets to the rest of the system. In the reference case, using Formula 19 at 1 Hz, the outward force was 0.177 N. Using Formula 26 and substituting \ddot{x} from Formula 13 to obtain Formula 27, we can evaluate the force of the magnet on the crank-slider. However, in Figure 17, it can be observed that in this case, where l is much greater than r , the max acceleration occurred when r and l were extended to their longest range, which was when θ equaled zero. The resulting crank-slider harvester maximum force at that moment was 2.35×10^{-3} N. Based on Formula 19 compared to Formula 27, these 1 Hz force calculations increased equivalently for both models at a value of ω^2 . Therefore, in all cases of ω for this experiment, the reference harvester would have significantly larger forces acting upon it. Having dense materials located at critical points such as the tips of the blades on the reference harvester, similarly to those presented in Figures 12 and 13, would be problematic considering the fact that the majority of failures for wind turbines are due to mass imbalances [64].

$$F = ma \quad (26)$$

$$F = mr\omega^2 \left(\cos(\theta) + \frac{r\cos(2\theta)}{l} \right) \quad (27)$$

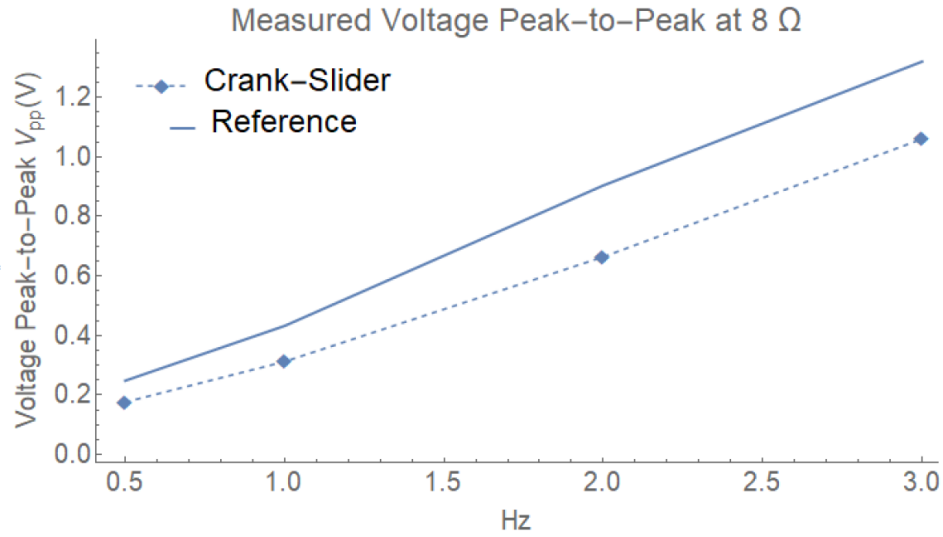


Figure 25: Measured peak-to-peak voltage demonstrating that the reference harvester had higher values than the crank-slider harvester at 0.5, 1, 2, and 3 Hz with a 8.4Ω load, signifying that the crank-slider harvester would have a greater range of wire gauge available.

4.3.2 V-Twin Harvester Utilizing Two Crank-Slider Mechanisms

Figure 27 depicts a combination of two crank-slider harvesters in a V-Twin formation similar to common designs used in motorcycle engines. Due to the magnets being positioned at a large distance relative the drop in magnetic field strength, it is assumed that neither magnet interferes with the other's coil when referring to $\Delta\Phi$ in Formula 6. This configuration allows for several methods of analyzing the output of the system by re-configuring the wiring of the two load resistors and two coils according to the wiring diagram column in Table 2.

This proposed device is simple in design, easily transported, and could be readily re-manufactured with most components being 3D-printed. In addition, the V-Twin has the potential to be used in various remote, hazardous, or emergency locations or

situations. This design has room to be improved by adding more crank-slider harvesters to the V-Twin design, including a rectifier and an energy storage system, or improving the coil structure by using a smaller-gauge wire with more turns.

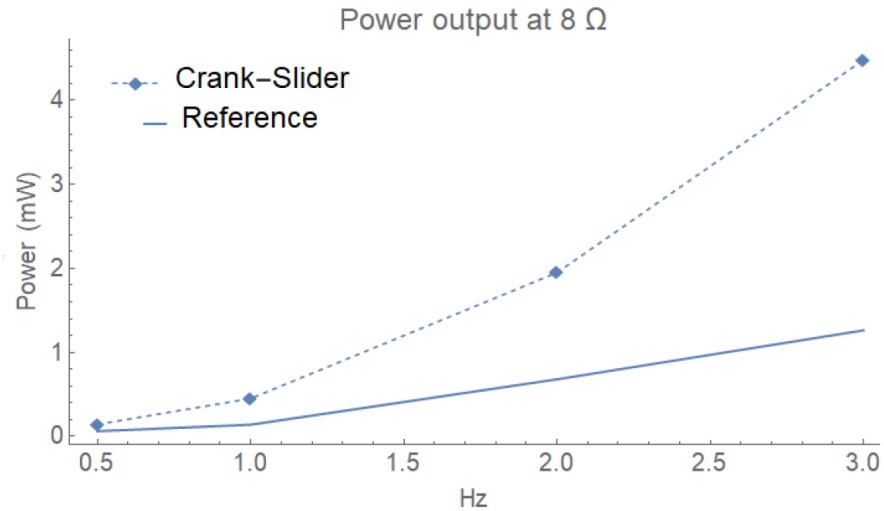


Figure 26: Power output demonstrating that the reference harvester had a lower power output than the crank-slider harvester at 0.5, 1, 2, and 3 Hz with a 8.4 Ω load.

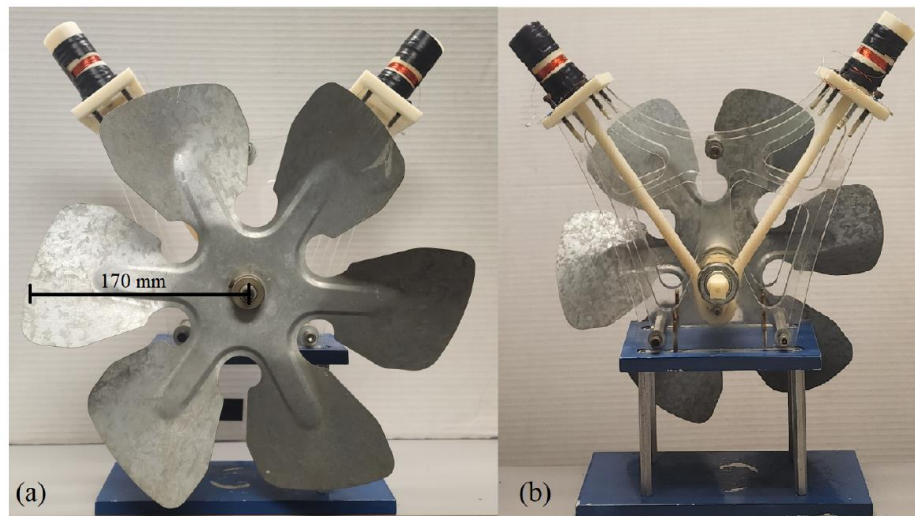


Figure 27: Front (a) and back (b) V-Twin harvester formation.

In Table 2, each measurement was made at 2 Hz for all configurations. In each configuration, the main difference when swapping the leads was observed when using the in- and out-of-sync patterns for the output. For example, in the first configuration image (a) under the oscilloscope output column in Table 2, the output from the V-Twin system was reminiscent of a typical sine wave output generated by the typical linear oscillating electromagnetic harvester akin to that in Figure 11. However, swapping the leads, as in image (b), resulted in an interesting output that showed improved performance across all configurations.

In the first configuration, which includes images (a) and (b) from Table 2, both cylinders and their loads were wired together in series with the other cylinder. In (b), the leads from the right cylinder were swapped with those from (a). In the second configuration, which includes images (c) and (d), each cylinder along with its load were wired in parallel with the other cylinder and load. These four configurations performed poorly, with the power output of both harvesters under-performing when having only a single harvester in operation. The highest power was generated in the third configuration, in which the system was wired with the coils in series with each other, and the loads in series but in parallel with the coils as shown in (e) and (f). Considering that a single crank-slider harvester under these conditions generated 2 mW, then it would be reasonable to assume that the standard for two would be 4 mW due to series stacking on phase output. However, as shown in image (f), with an output of 7.30 mW, this configuration produced 45.2% more power than what would be expected by the standard. Conversely, having the system in parallel reduced the overall output, with image (c) showing the poorest performance due to parallel stacking.

Table 2: Output of V-Twin harvesters in both series and parallel configuration at 2 Hz. (a) each cylinder and its respective load resistance of 8.2Ω were wired in series as units. The resulting total load resistance was 16.4Ω . (b) the output leads of the right cylinder were interchanged from the system shown in image (a). (c) each cylinder and its respective load resistance of 8.2Ω in parallel as units. (d) the output leads of the right cylinder were switched from the system shown in image (c). In (e), each cylinder was wired in series and both loads were wired in series; however, both cylinders were kept in parallel with both loads. In (f), the output leads of the right cylinder were switched with those from the system shown in image (e).

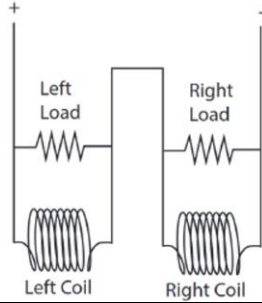
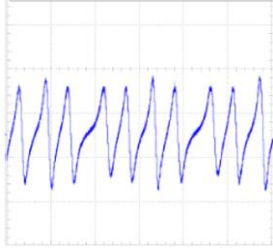
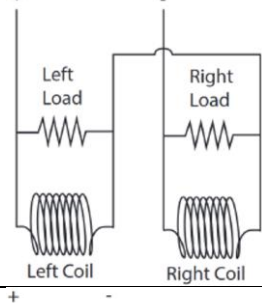
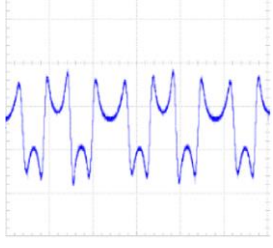
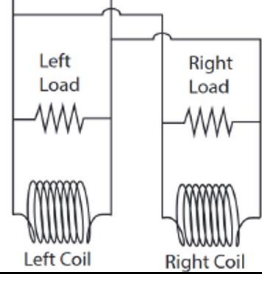
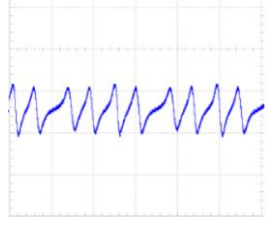
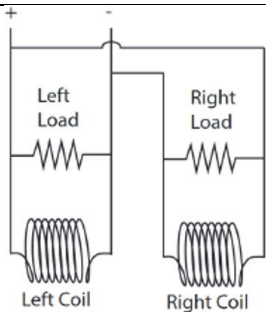
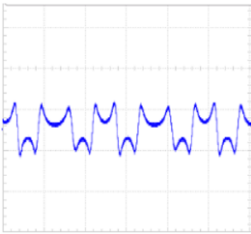
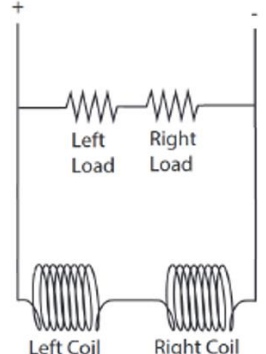
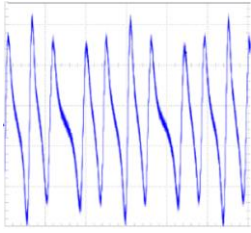
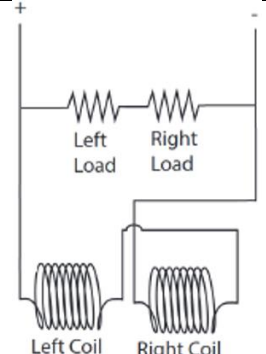
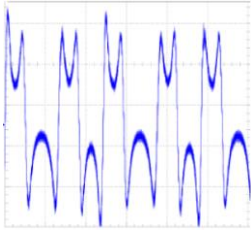
Image	Wiring Diagram	Oscilloscope Output	V_{rms} (mV)	Power (mW)
(a)			184	2.05
(b)			210	2.7
(c)			92.5	0.5

Table 2: Continued				
(d)			105	0.65
(e)			308	5.78
(f)			346	7.30

A residential fan was used to supply input wind energy to the device using three standard speeds—3.2, 3.4, and 4.1 m/s—measured at 65 mm from the surface using an XRCLIF-818 Anemometer. We found that the threshold speed fell between 3.2 and 3.4 m/s. At 3.2 m/s, the V-Twin harvester would require a small force to overcome initial resisting forces. However, at 3.4 m/s the system could start harvesting with only the residential fan acting upon it.

Table 3, summarizes the performances of comparable style and size for the harvesting devices and indicates that the proposed V-Twin harvesters displayed the highest wind speed to power conversion. As shown in Table 3, the V-Twin system presented in this paper used the optimal set up shown in image (f) in Table 2 across a load of 16.3Ω and had measurements taken at 3.4 and 4.1 m/s. The small-scale windmill design by Myers et al. [34] utilizes wind energy harvesting in combination with piezoelectric bimorph transducers. We compared the highest readings (from lab results) listed in a study on highway bridge vibrations by Peigney and Siegert [65]. Both vehicle-mounted harvesters developed by Li et al. utilize wind harvesting to excite a piezoelectric device [66]. In their designs, the difference between FPEH and EVEH was that of a ‘fluttering’ device versus a linear electromagnetic harvester. A triboelectric-hybrid study by Ye et al. developed multiple devices and configurations; however, the highest performance was observed for the FBEMG design that used a rotor and stator to harvest wind energy [67]. The outdoor IoT harvester designed by Fang et al. is similar to our reference harvester, utilizing rotating magnets at a large radius to harvest wind [55]. For the galloping wind harvester studied by Wang et al., the SHPTWEH had the highest performance, out of the several versions that were developed [68]. Cao et al. developed a Canyon Bridge system that used a combination of both piezoelectric and electromagnetic harvesters in their design [69].

Table 3: Harvester wind speed testing comparison.

Design	Reference Number	Winds Speed (m/s)	Harvester Frequency (Hz)	Power (mW)	Conversion Mechanism
V-Twin	(f)	3.4	6.38	27.0	Dynamo with Rotation
V-Twin	(f)	4.1	7.72	42.2	Dynamo with Rotation
Small Scale Windmill	[34]	4.47	4.5	5	Piezoelectric with Vibration
Highway Bridge Vibrations	[65]	N/A	4.1	1.8	Piezoelectric with Vibration
Vehicle-Mounted Harvester (FPEH)	[66]	18	N/A	14.5	Piezoelectric with Vibration
Vehicle-Mounted Harvester (EVEH)	[66]	18	N/A	31.8	Dynamo with Vibration
Triboelectric-Hybrid (FB-EMG)	[67]	6.96	N/A	4.23	Rotor/Stator with Rotation
Outdoor IoT Harvester	[55]	12	4.45	62	Rotor/Stator with Rotation
Galloping Wind Harvester (SHPTWEH)	[68]	14	N/A	0.238	Piezoelectric – Triboelectric with Vibration
Canyon Bridge (WEHS)	[69]	6.5	40.56	19.24	Hybrid using both Piezoelectric Electromagnetic with Rotation

4.4 Conclusion

Based on the analysis of the crank-slider design presented in Section 4.4, in this study we designed and fabricated a novel V-Twin-shaped energy harvester to convert rotational energy from wind into electrical energy using inductive energy harvesting. From the single magnet and coil crank-slider system operating at a regulated 2 Hz across an optimized load of 8.4Ω , the average power generated was 2.0 mW. In order to improve the power output at low frequency, a V-Twin harvester was designed. This

improved design combined two of the crank-slider designs into a single harvester output and it was evaluated under several operating conditions. We experimentally observed that the V-Twin system wired in a series configuration produced 7.30 mW at the same regulated frequency of 2 Hz. The results demonstrate an increase in performance over two crank-slider harvesters of 45.2%. We also found that the V-Twin harvester generated 27.0 and 42.2 mW of power at wind speeds of 3.4 and 4.1 m/s for the optimized configuration, i.e., series-series electrical connections for coils and loads.

The results show that this is a promising solution for the harvesting of low-to-high-speed wind energy as a method of powering small-scale electronic devices such as cell phones or smart devices. We believe that the energy harvester design proposed here is much cleaner, with less interface, than those of commercially available wind energy harvesters used for generating electricity on a large scale.

CHAPTER 5

MULTICYLINDER HARVESTER

This section is a compilation of research as prepared to be submitted on a multicylinder harvester that uses a modified crank-slider mechanism.

5.1 Introduction

Several issues affect the sustainability of global energy resources. The first, and possibly most critical, is the estimated fifty years of global oil reserves remaining [32]. Second, the demand for electricity has increased dramatically from 0.3 trillion kWh to 4.0 trillion kWh since 1950 in the U.S alone [31]. Third, electronics, specifically small energy consuming devices such as smartphones, laptops, Bluetooth devices, etc. are an increasingly significant and necessary component of our everyday lives [70, 71]. As a method to address these energy issues without reducing consumption, significant resources have gone into finding and improving energy harvesting substitutions in the form of wind, solar, thermo, vibration, and other forms of ambient energy sources [71, 72]. Many of these substitutions are already implemented on a large scale in the form of wind farms, solar farms, and nuclear plants. Unfortunately, the scale of the devices used on these farms and their method of power transportation are not viable as power sources in some remote or hazardous locations, as emergency power backups in instances where the power grid is compromised, or as supplemental power for small applications such as

recharging electric livestock fences. It is these smaller applications in which an alternative such as small-scale energy harvesters become an attractive option.

Although small-scale harvesters have improved over the years, they still have shortcomings. For example, turbine style wind or water harvesters and solar panels depend on the orientation of the devices in order to optimize their power output. Some of solar power harvesting's challenges are conversion issues, solar prediction, and intermittency [73], and as expected, solar harvesters do not produce during the night. With wind and water turbine harvesters, low output correlates to slow fluid speed, compounded by the losses due to internal resistances of the device as well as overcoming the high start-up torque at slow fluid speeds. Both styles of devices are also dependent upon the contact area of either the surface area of the solar panel or size of rotor blades for increasing the outputs. Vibration harvesters are restricted by the alignment of the device and the frequency of the vibrations. Another issue with smaller devices is the need to reduce their footprint while still maintaining or preferably increasing the power output.

Small scale solar power harvesting is typically restricted to well established pre-manufactured panels and kits. On the other hand, experimental electromagnetic energy harvesting methods have been published combining various methods of harvesting from wind, fluid, and vibration harvesters in combination with induction and piezoelectric devices. As advances are made, these devices show more promise as alternative energy sources with some harvesters generating 8 mW per cm³ [35]. Other examples have included devices using piezoelectric in shoes which have generated 38V [8], a small 1 cm² electrostatic device which generated 549 μ W [9], and a dynamo with rotation device which generated 42.2 mW under a wind speed of 4.1 m/s [12].

For induction harvesters, Faraday's law describes how a changing magnetic field through a coil of wire produces an electromotive force. That changing field is produced in several ways; however, the most recognizable are the rotor-stator and magnet through coil style. With the rotor-stator harvester, a permanent magnet travels across a coil without passing through, whereas a magnet through coil style harvester has a magnet that passes through a coil of wire. Each has their own benefits and limitations; however, given similar conditions, same strength and size of magnet and coil, the magnet through coil will produce higher root-mean-square Voltage (V_{rms}) whereas the rotor-stator will have higher peak-to-peak voltage (V_{pp}) [12].

When charging small energy devices, sensors have power consumption less than a microwatt [74] as low as $100\ \mu\text{W}$ [75] and smart devices can be in the low milliwatts [76] ranging from $20\ \text{mW}$ to $1.3\ \text{W}$ [75]. One issue with electromagnetic harvesters is that they produce an alternating current (AC) [77] when the devices they are generally intended to charge require direct current (DC). A rectifier converts AC to DC by inverting the negative portion of the output. A capacitor can be added to smooth any variances in the rectified output. Once rectified, smoothed, and within a device's tolerances, the power produced can be used to power a sensor [77], charge a smart device, or be stored in a battery power supply for later use. In this paper, we will evaluate a magnet through coil wind harvester utilizing a modified crank-slider mechanism for smaller footprint, operating at low wind speeds of $2.3\ \text{m/s}$, capable of producing $421\ \text{mW}$ at higher wind speeds, and can be used to charge small electronic devices.

This section is organized as follows. The introduction covers the background for why there is a demand for innovation in alternative energy, what ways small-scale

harvesting can offset certain the demand in certain applications, how limitations and designs effect these harvesters, and an overview of the induction with rotation style designs. The second section, we discuss the design, methods of measuring, analysis techniques, and specifically the major difference between how the two styles of cylinders are connected to the crank and how the output is rectified and smoothed. The third section includes the single coil analysis, maximized power transfer, no load and loaded output along with different frequencies and various smoothing capacitors. Additionally, this section covers how two cylinders at various positions interact regarding phase angle and inverted output. Finally, section three evaluates the output of all six cylinders including average output voltage real-world testing including outdoor ambient wind harvesting to charge a smart watch, and a comparison to other similar works. The final section concludes with a summary of the main findings, importance and relevance of the study.

5.2 Materials and Methods

Figure 28 represents the small-scale wind harvesting process from ambient energy sources to applications. This project evaluates portions from each step in the process. The device is operated by placing it on a flat surface and exposed to a minimum wind speed of 2.3 m/s. The airflow rotates the fan blades of the device, which in turn moves the induction components. The AC wave produced is converted to DC via a full bridge rectifier whose output is sent through a 5 V regulator. The cleaned 5 V is either stored or

used. For the purpose of this research project, the storage devices used were a smart watch and a 5 V battery power supply.

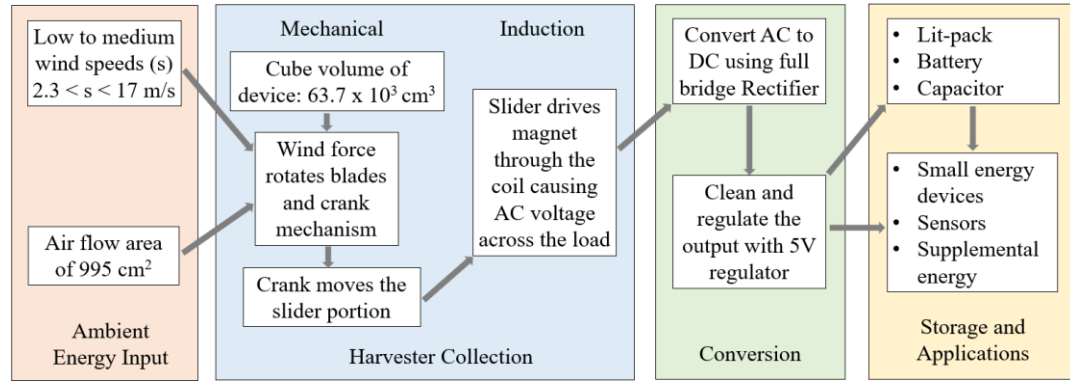


Figure 28: Wind harvesting process used.

The multi-cylinder harvester located in the Harvester Collection portion of Figure 28, is represented in Figure 29 and 30. It includes up to six crank slider mechanisms with electromagnetic harvesting cylinders. Figure 29 right is the crank adapter portion of the mechanism along with the fixed rod for cylinder A in the vertical position and an additional crank with rotation as represented in an angled position. For cylinder A in Figure 31 (left), the crank portion is bound as a fixed connection to the crank adapter. The fixed portion of the shaft is enhanced in Figure 32. One additional benefit of this modified crank-slider mechanism is how the modification allows for the cylinders to all be aligned in the same plane, as seen in Figure 30 center. This style of connection is a typical crank-slider, allowing for cylinder A to operate under the same kinematics for a crank-slider mechanism as outlined in Figure 33 with Formula 28 through 33. The crank for cylinder A has a crank radius (r_A) of 2.54 cm and an arm length (l_A) of 15.24 cm.

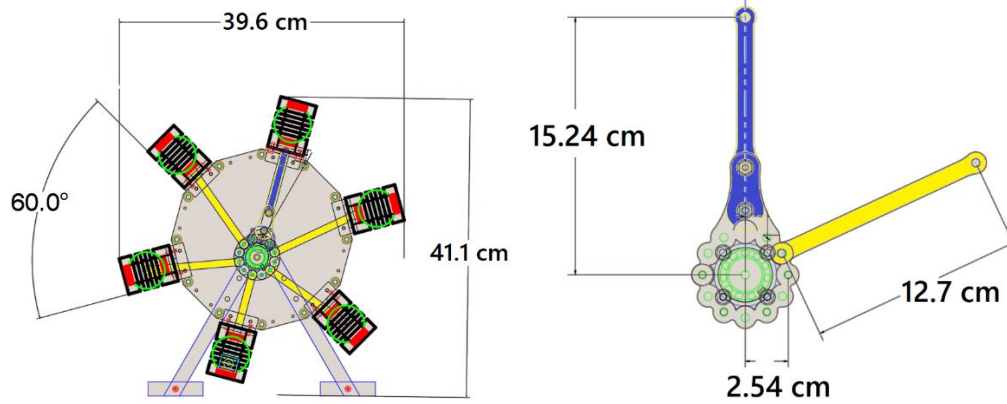


Figure 29: CAD drawings. Left: Full assembly showing the planned angle between each cylinder. Right: Enhanced view of how the blue arm for cylinder A is fixed in its connection to the crank portion and how all the yellow arms have a point of rotation for their connection to the crank portion.

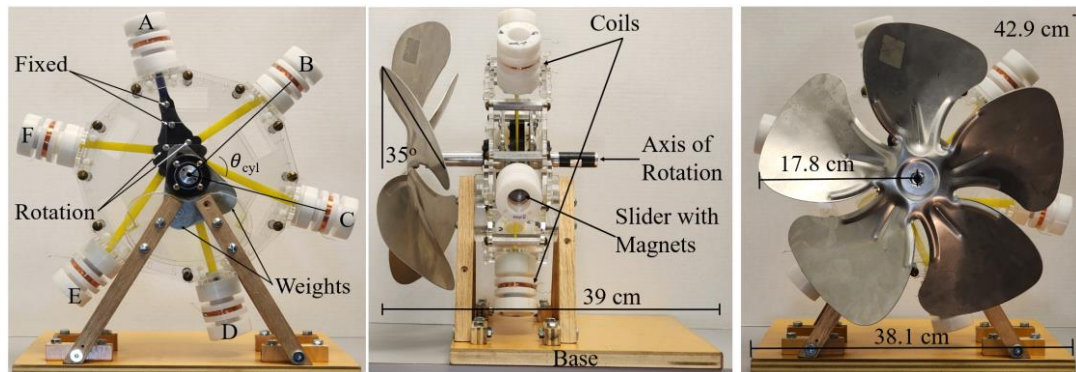


Figure 30: Actual build. Left: Front view of harvester without the fan portion showing the six cylinders with cylinder A being fixed to the crank portion. The remaining cylinders B, C, D, E, and F have a rotational point connected to the crank portion. Weights attached at different locations to balance the system. Angle θ_{cyl} as the angle between each of the cylinders. Center: Side view showing the pitch of the blade, depth of the total device, coils, location of magnet within each coil, and axis of rotation. Right: Front view with fan attached with fan radius, harvester height and width.

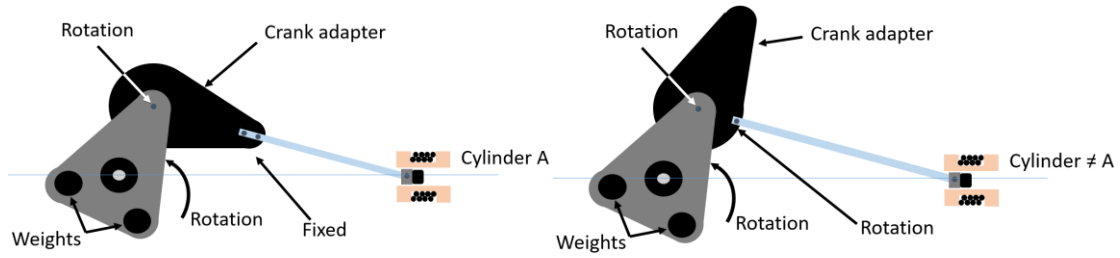


Figure 31: Left: Cylinder A demonstrating the fixed connection between the crank adapter and shaft (l_A). Right: Cylinders that are not A. This demonstrates how cylinders B, C, D, E, F, and G have a point of rotation between the primary crank at the axis of rotation as seen in Figures 29, and 30.

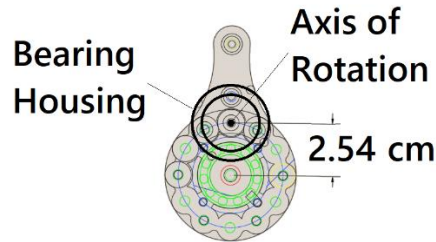


Figure 32: Enhanced CAD drawing for the crank portion demonstrating the axis of rotation for cylinder A along with the crank length for cylinder A. This image does not include the crank adapter portion.

The kinematic analysis for the magnet associated with cylinder A which is attached to the slider portion as depicted in Figure 33 is as follows. The point (x_A), which travels irrespective to the coil, in Figure 33 and Formula 28, represents the position of the magnet for cylinder A with respect to the axis of rotation. For cylinder A, its mechanical components consist of the crank depicted in Figure 32 with radius (r_A) of 2.54 cm and the shaft portion (l_A) with a length of 15.24 cm.

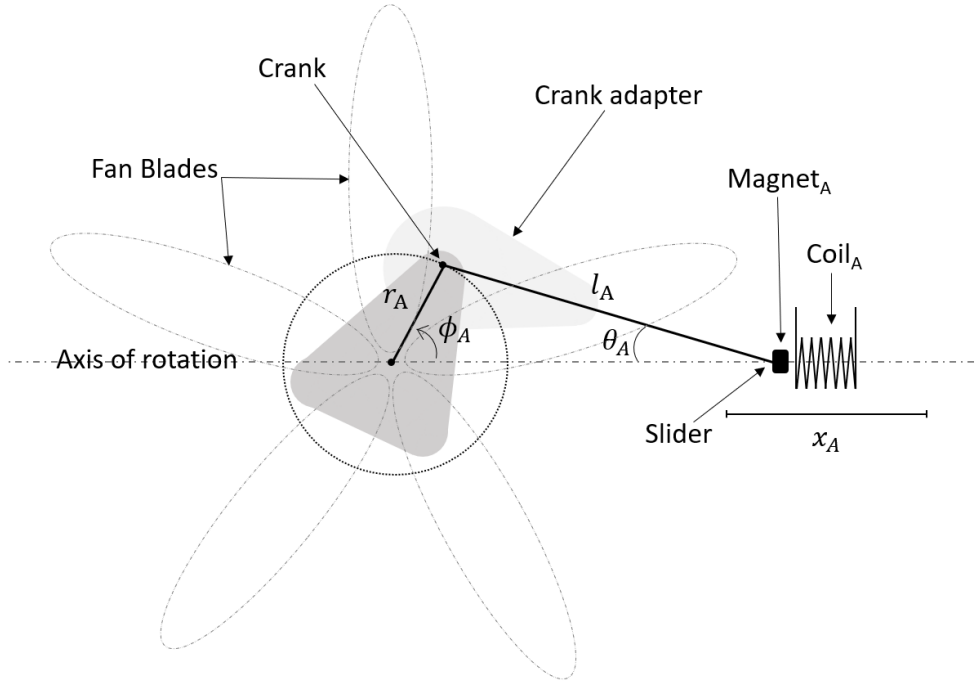


Figure 33: Crank-slider mechanism for cylinder A with kinematic values for Formulas 37 through 42.

The velocity (\dot{x}_A) for the magnet associated with cylinder A is represented in Formula 29. By using the relationship between θ_A and ϕ_A in Formula 30, $\cos(\phi_A)$ can be replaced in Formula 29 as a method to remove ϕ_A so that the angle to solve for \dot{x}_A is dependent upon θ_A as seen in Formula 31.

$$x_A = r_A \cos(\theta_A) + \sqrt{l_A^2 - r_A^2 \sin^2(\theta_A)} \quad (28)$$

$$\dot{x}_A = -r_a \omega \left(\sin(\theta_A) + \frac{r_A \sin(2\theta_A)}{2l_A \cos(\phi_A)} \right) \quad (29)$$

$$\cos(\phi_A) = \sqrt{1 - \left(\frac{r_A \sin(\theta_A)}{l_A}\right)^2} \quad (30)$$

$$\dot{x}_A = -r_A \omega \left(\sin(\theta_A) + \frac{r_A \sin(2\theta_A)}{2l_A \sqrt{1 - \left(\frac{r_A \sin(\theta_A)}{l_A}\right)^2}} \right) \quad (31)$$

From Figures 29 and 32 regarding the components for cylinder A, the value for l_A of 15.24 cm is greater than four times that of 2.54 cm for r_A , this allows for the acceleration (\ddot{x}_A) of the magnet for cylinder A in Figure 33 to be represented as Formula 32 [59].

$$\ddot{x}_A = -r_A \alpha \left(\sin(\theta_A) + \frac{r_A \sin(2\theta_A)}{2l_A} \right) - r_A \omega^2 \left(\cos(\theta_A) + \frac{r_A \cos(2\theta_A)}{l_A} \right) \quad (32)$$

Additionally, in Formula 32, the leading portion contains the acceleration component (α) of the solution. The data collected during this research under operating conditions assumes that the driving velocity, provided by wind, of the mechanism at the axis of rotation is constant, therefore, the leading portion of Formula 32 containing α is removed to give the approximated value for \ddot{x}_A as Formula 33 [59].

$$\ddot{x}_A = -r_A \omega^2 \left(\cos(\theta_A) + \frac{r_A \cos(2\theta_A)}{l_A} \right) \quad (33)$$

Using the given values for r_A and l_A for cylinder A, the remaining value for angular velocity is determined by the input from the crank. The points of interest are where the linear velocity and acceleration are either zero or at an absolute maximum, either a positive or negative value indicating the direction. For \dot{x}_A , the maximum occurs at the 90 and 270 degree position. At these locations, the slider is at the halfway point between the minimum and maximum stroke length. Additionally, at this same position, \ddot{x}_A is at zero. Conversely, when the crank is at the 0 and 180 degree position, where the slider is at a maximum and minimum length, \dot{x}_A is zero and \ddot{x}_A is at its maximums.

The theoretical induced voltage U_V given by Formula 34 is dependent upon the velocity of the magnet (\dot{x}_A), the magnetic field (\mathbf{B}), and length of wire (L) for the coil [59]. The values of \mathbf{B} can be evaluated using either multiphysics software such as COMSOL as seen in Figure# 34 or using physical readings with a Teslameter. A comparison of both COMSOL and physical readings for a given line of travel along the Z-axis where the coil would align, are plotted in Figure 35.

$$U_V = BL\dot{x}_A \quad (34)$$

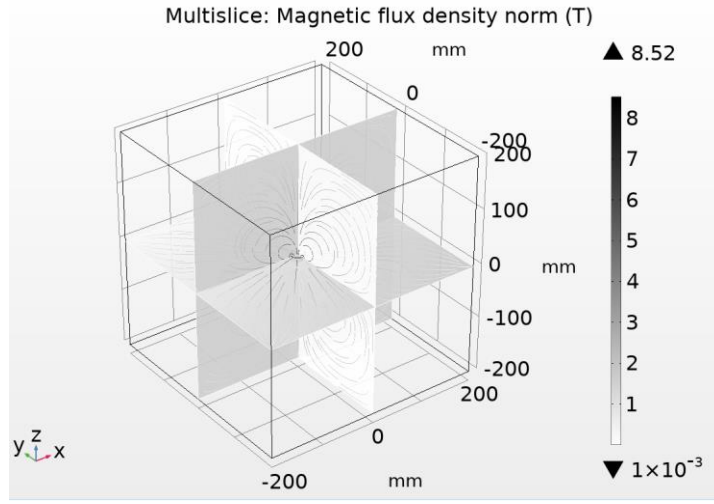


Figure 34: Theoretical COMSOL field estimating one N52 axially magnetized disk magnets with a diameter of 2.54 cm and a thickness of 0.635 cm and a B_r max of 1.48 T along the z-axis.

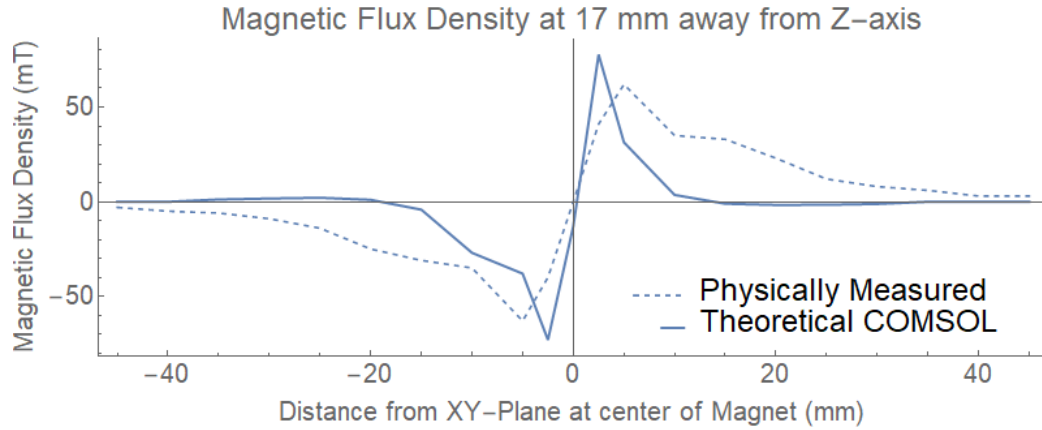


Figure 35: Comparison of COMSOL theoretical values and physically measured values for Magnetic Flux Density along the Z-axis in a line through the coil and along the axis of oscillation. Values measured with a WT10 Teslameter at the specified distances. COMSOL values gathered from the field in Figure 34 along the XY-plane.

The transduction coefficient (Φ) in Formula 34 and 35 [18] are substituted with \dot{x}_A from Formula 30 resulting in Formula 36. Figure 36 is a sample output of Φ with both

the COMSOL generated theoretical values from Figure 35 and the experimental values measured with a telsameter.

$$\Phi = BL \quad (35)$$

$$U_V = \Phi r \omega \left(\sin(\theta) + \frac{r \sin(2\theta)}{2l \sqrt{1 - \left(\frac{r \sin(\theta)}{l}\right)^2}} \right) \quad (36)$$

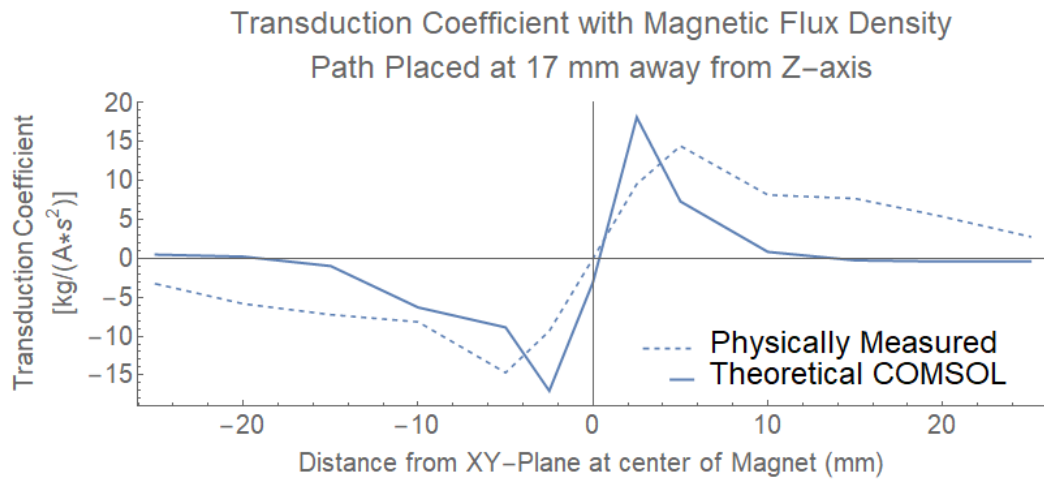


Figure 36: Transduction coefficient (Φ) using theoretical COMSOL values and physically measured values from Figure 35 from the motion of travel for the magnet if it travelled from 0 to π with a crank radius of 2.54 cm.

In Figures 29 and 32, the cylinders other than cylinder A have a different method of motion due to how they are connected. Figure 37 demonstrates the additional connection including the length (d) located in the crank adapter.

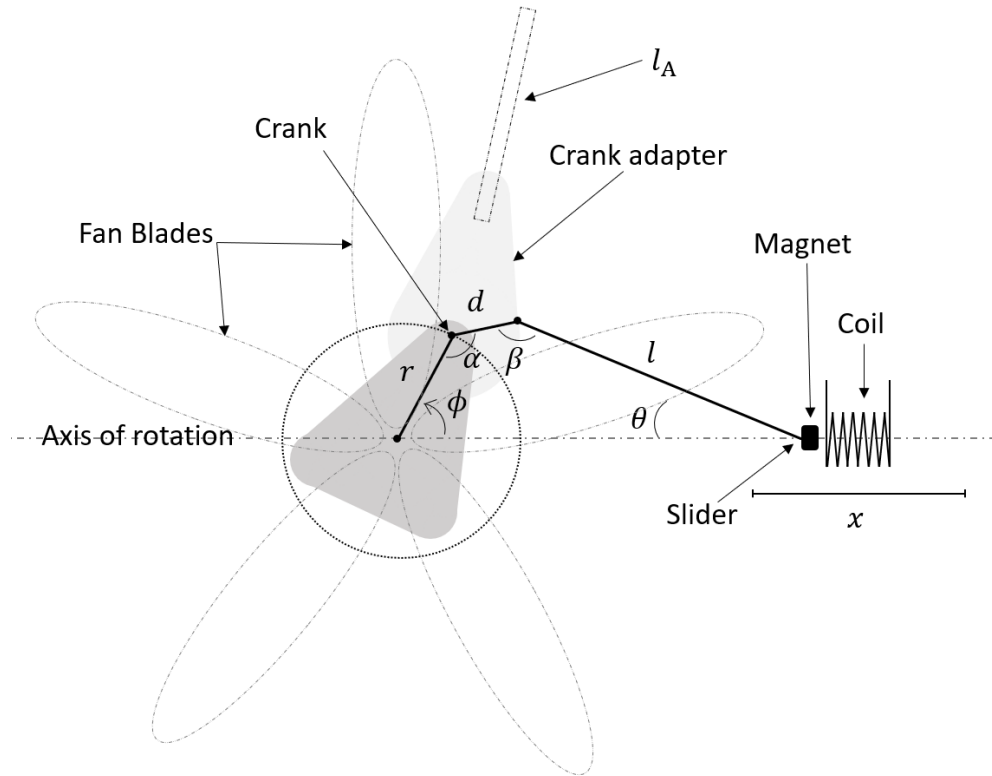


Figure 37: Crank-slider with crank adapter mechanism for all cylinders other than cylinder A.

In Figure 38, the left images show the maximum extended and minimum retracted lengths for cylinder A. This occurs at 0 and 180 degrees for the crank. Assuming the starting position is when the point x_A is at the fully extended position, a full rotation results in the position going from fully extended at 0 degrees, through the magnet to the retracted 180 degrees, then back to the extended position at 360 or 0 degrees. This all

occurs within some set time (t) and total travel distance of $4r_A$. During the same time (t) all other cylinders also travel 360 degrees for a total travel distance of $4r$, seen in the right images of Figure 38. With r_A and r being the same distance, the resulting average velocity for all cylinders is the same.

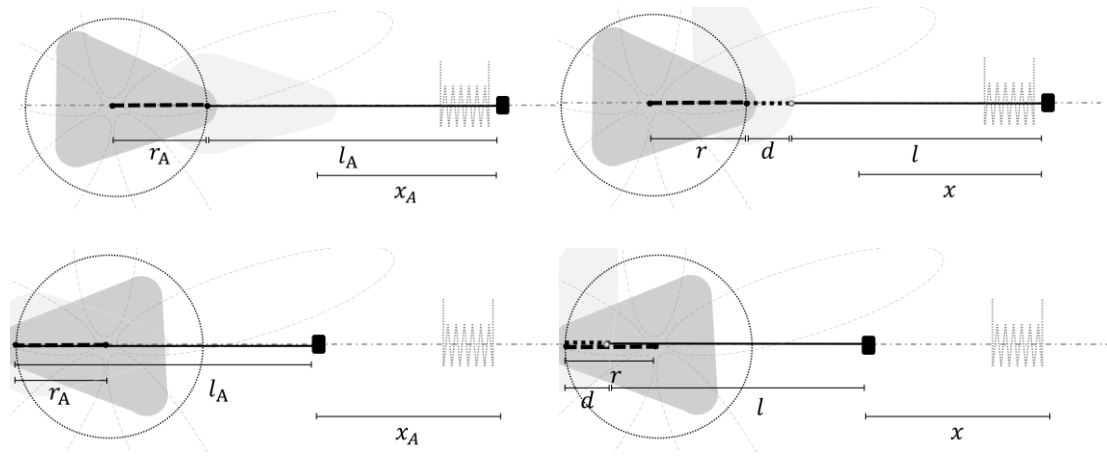


Figure 38: Minimum and maximum stroke lengths. Top left: maximum distance (x_A) for cylinder A. Bottom left: minimum distance (x_A) for cylinder A. Top right: maximum distance (x) for any cylinder that is not cylinder A. Bottom right: minimum distance (x) for any cylinder that is not cylinder A. In each of these states the crank radius (r) is aligned with the shaft (l) and in the cases of non A cylinder, the crank adapter radius (d) is also in alignment.

Furthermore, the output of cylinder B when compared to cylinder A has a similar output only offset by a phase difference of 60 degrees as seen in Figure 39. Each cylinder's output is offset based on their position relative to cylinder A, see Figure 30 compared to Figure 39. Additionally, each complete rotation of the fan results in two passes of the magnet through the coil. In this study, one rotation of the fan blade, also known as the ordinary frequency or rotational frequency, will be referred to as one Hz.

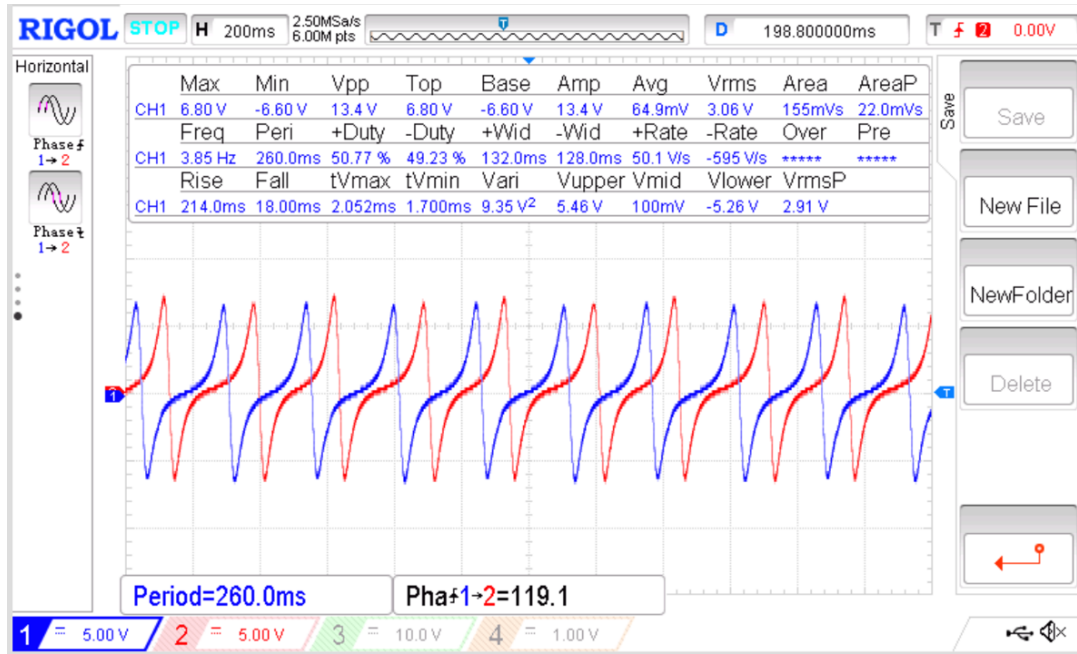


Figure 39: Oscilloscope output for cylinder A with an additional cylinder B demonstrating the same output with a 60 degrees phase difference.

The magnets for all cylinders are N52 axial magnetized disk magnets with a diameter of 2.54 cm, a thickness of 0.635 cm, and have a $B_{r,max}$ of 1.48 T as indicated by the purchasing website through K&J Magnetics. The coils are wound from coated 36 AWG with 2000 turns resulting in a total wire length of 233.2 m, inner coil diameter of 2.84 cm, an outer coil diameter of 4.4 cm, and with an average resistance of 308 ohms. The resistance, number of turns, and wire length was verified by calculating an expected total resistance (R_{total}) using the average length of wire (l_{wire}) for each coil and AWG standard resistance of that wire per meter (R_m) as seen in Formula 37. The result is 318 ohm, which was close to the average measured resistance of 308 ohm.

$$R_{total} = l_{wire} R_m \quad (37)$$

In addition to the mechanical and electromechanical components presented in Figure 30, this research included a rectifier and voltage regulator as outlined in Figure 28. The AC voltage from Figure 39 is sent through the AC Voltage In where it is rectified to the DC Voltage Out seen in Figure 41. The DC voltage is smoothed with a capacitor resulting in Figure 42 where the smoothness is dependent upon the capacitor size. However, increasing the size of the capacitor results in an increase in reactive power. Therefore, increasing the capacitor does not optimize the true power. Finally, the smoothed DC voltage is sent through a 5V regulator before being used by the small electronic device.

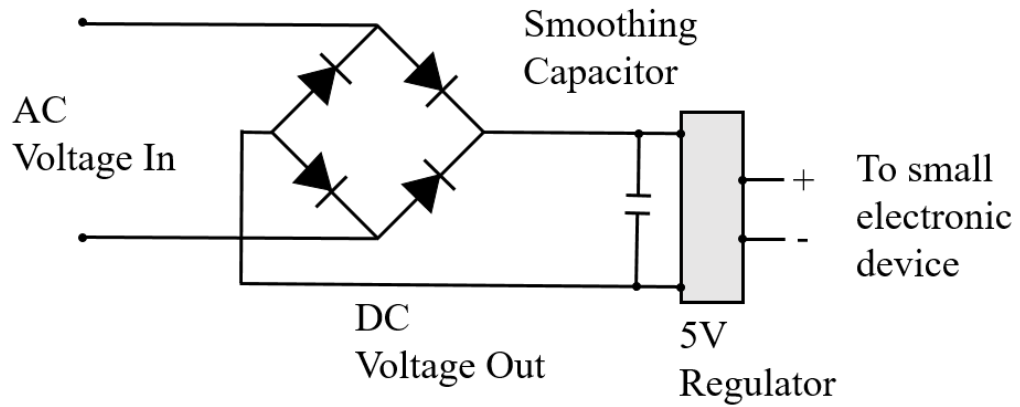


Figure 40: Rectifier with smoothing capacitor and 5V regulator.

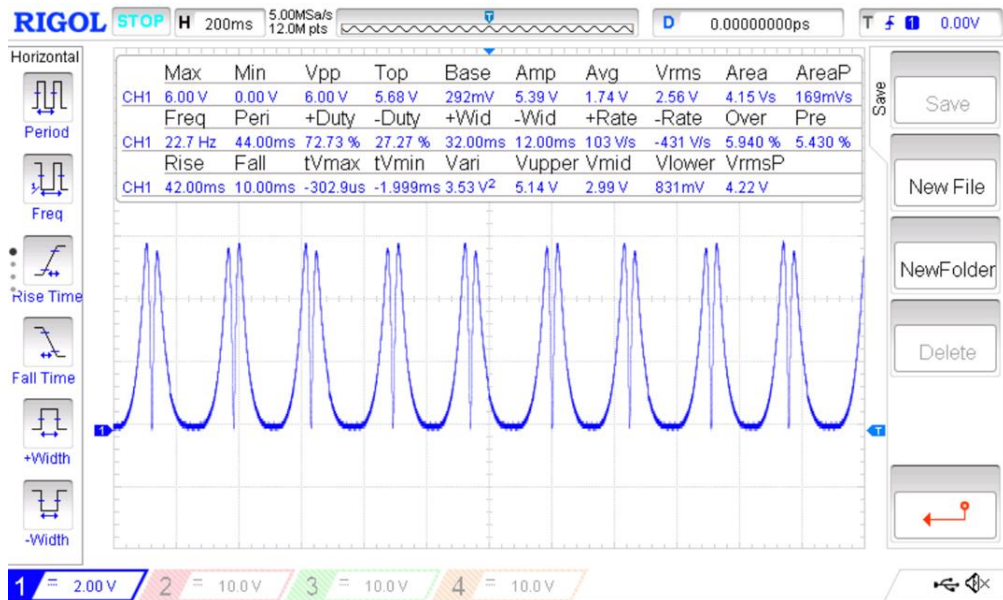


Figure 41: Oscilloscope output for a single cylinder with full bridge rectifier and no smoothing capacitor.

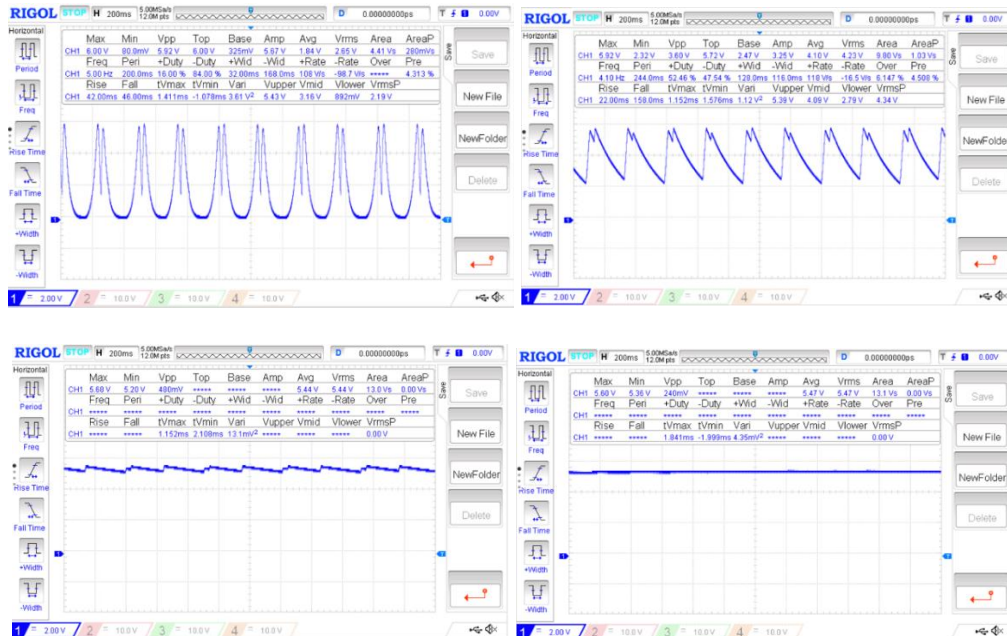


Figure 42: Oscilloscope output for single cylinder with rectifier and smoothing capacitor. Top Left: 10 nF smoothing capacitor, Top Right: 220 nF smoothing capacitor, Bottom Left: 4.7 μ F smoothing capacitor, Bottom Right: 47 μ F smoothing capacitor.

5.3 Results and Discussion

5.3.1 Output with Single Coil

When analyzing the output of a harvester, one of the first objectives is to evaluate the optimal load. For a single coil the internal resistance for this test was 308 Ohm.

Figure 43 demonstrates the optimal load given several test frequencies and various test loads. In each case the optimal power transfer occurred near 308 where coil and load impedance match [18, 61].

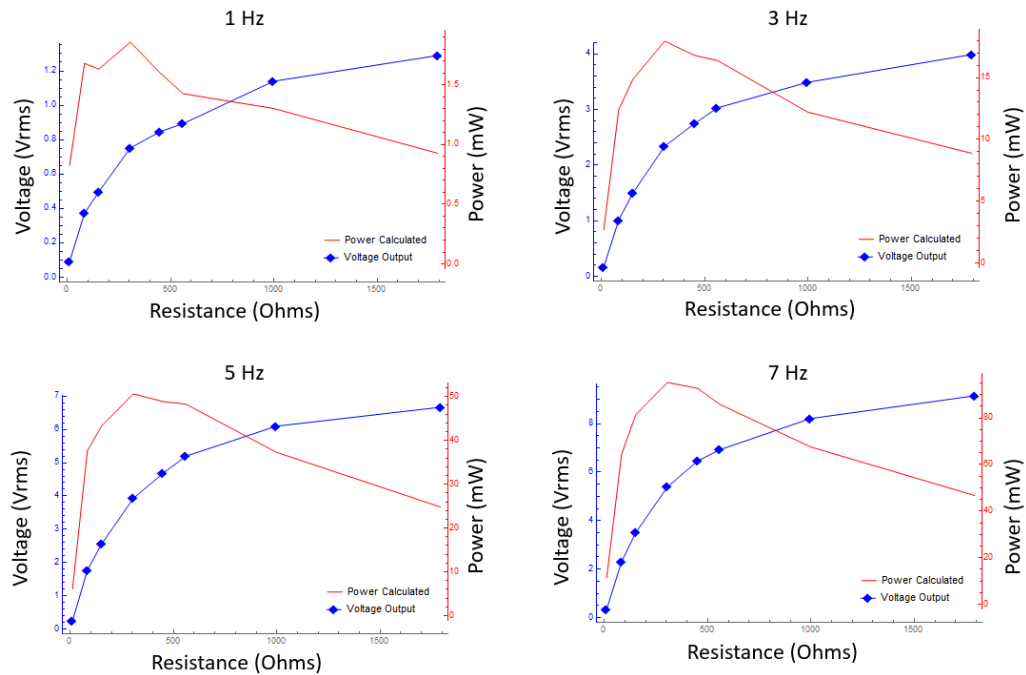


Figure 43: Voltage and power output for a single harvester coil at 1, 3, 5, and 7 Hz. The coil has an internal resistance of 308 Ohms. The test loads ranged from 10.46 to 1792 Ohms. The stroke length of 5 cm from Figures 32, 33, and 38.

According to Formula 34 and 36, as the fan rotates faster, the velocity of the slider increases thus increasing the voltage output. Table 4 verifies the expectation that the increase in V_{rms} for both the no load and optimized load states of a single harvester cylinder.

Table 4: V_{rms} output with oscilloscope under no load and 305 Ohm load at frequencies from 0.5 to 8 Hz.

Frequency	0.5	1	2	3	4	5	6	7	8
V_{rms} with no load (V)	1.12	1.54	2.96	4.49	6.14	7.71	9.19	10.9	12.5
V_{rms} with 305 Ohm Load (V)	0.779	0.811	1.52	2.26	3.1	3.83	4.62	5.43	6.2

Table 5 and Figure 44 are the output of a single cylinder with rectifier under a no load situation with a smoothing capacitor. As seen in Figure 44, as the smoothing capacitor value increases, the voltage output flattens. Table 5 compares the exact values measured by the oscilloscope for both the rms and average values of the output voltage. As the smoothing capacitor value increases, the rms and average output converge. For a single coil, the convergence occurs at 470 nF. Therefore, any capacitor value beyond 470 nF no longer provides improved smoothing and only contributes to increasing reactive power which is not an improvement to the system.

Table 5: Comparison of rectified voltage output when incorporating smoothing capacitor at 2 Hz with no load.

Capacitor(F)	0	10 p	1 n	10 n	68 n	220 n	470 n	4.7 μ	47 μ	470 μ
V_{rms} (V)	2.56	2.6	2.54	2.65	3.19	4.23	4.79	5.44	5.47	5.16
V_{avg} (V)	1.74	1.77	1.71	1.84	2.72	4.1	4.74	5.44	5.47	5.16

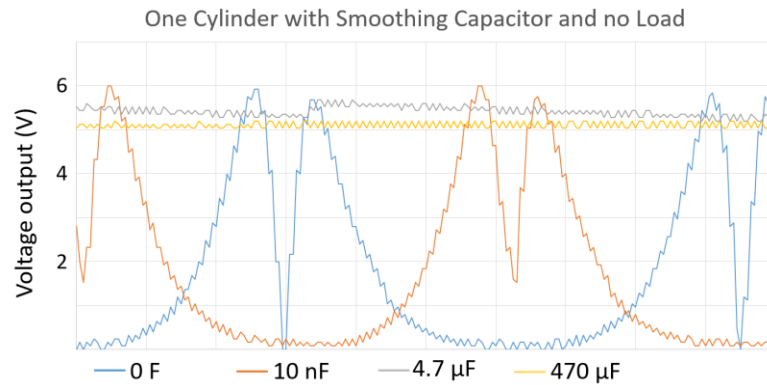


Figure 44: Output of four levels of smoothing capacitor at 2 Hz with no load.

5.3.2 Two Cylinders Compared

When connecting more than one cylinder, the orientation and connection of the two cylinders together can be either in phase or out of phase as seen in Figures 45 and 46. In the left portion of Figures 45 and 46, cylinder A and B are 60 degrees out of phase, however, by changing the electrical connections for cylinder B the output is inverted as seen in Figures 45 right and 46 right.

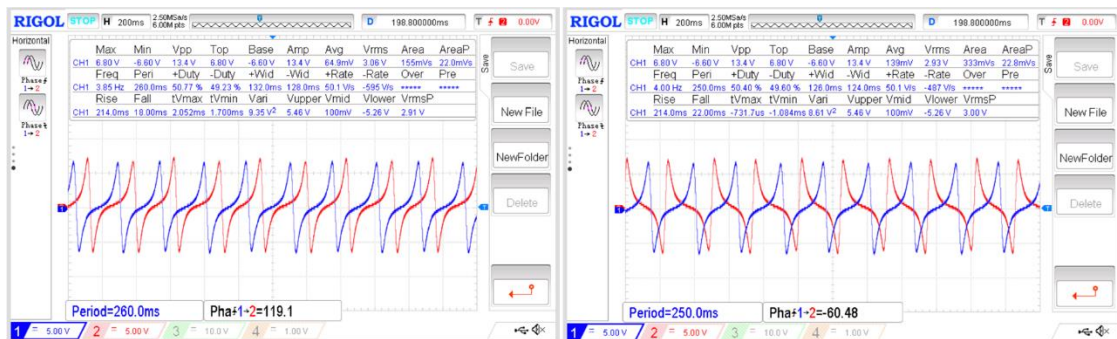


Figure 45: Sample outputs of cylinder A and B. Left image shows the 60 degree phase difference with both cylinder outputs in the same orientation. Right image shows the output when cylinder B has its output connections reversed.

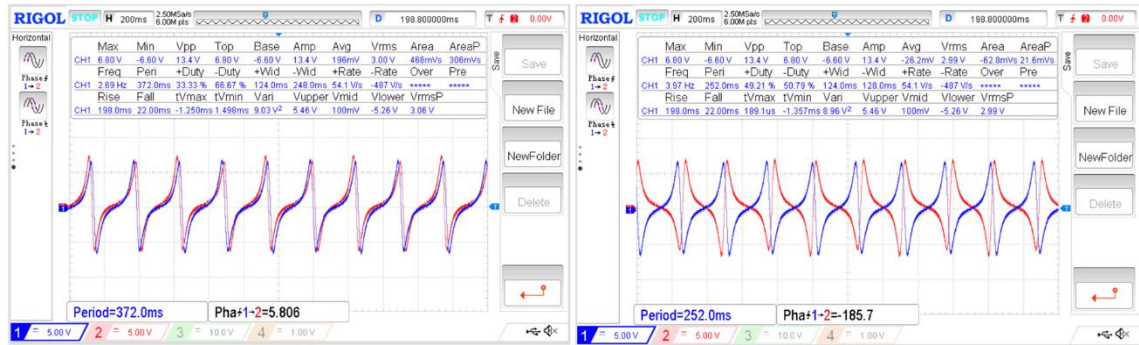


Figure 46: Sample outputs of cylinder A and D. Left image shows the overlap of A and D when they are connected in phase due to their physical orientation being 180 degrees as seen in Figures 29 and 30. Right image shows the output when cylinder D has its output connections reversed so it is 180 degrees out of phase with cylinder A.

5.3.3 Output with All Six Cylinders

The output for three adjacent cylinders is seen in Figure 47 with the output separated to. As with two cylinders, each output is 60 degrees out of phase with each other. Figure 48 shows the output of all six cylinders and from this figure, we can observe that when two cylinders are 180 degrees out of phase and connected with poles reversed as seen in V-Twin design, the output is now back in phase. This can be observed in the dashed vertical lines connecting A to D, B to E, and C to F.

In Figure 49, the left image is the output of all six cylinders post rectifier. In this image, the average voltage output is 14.0 V, however there is still significant variation in maximum and minimum voltage with the peak-to-peak voltage being 9.0 V. In Figure 49, the right image includes a smoothing capacitor, and the peak-to-peak voltage is 200 mV. In addition, with the smoothing capacitor, the average voltage increases, and the result is a steady voltage output.

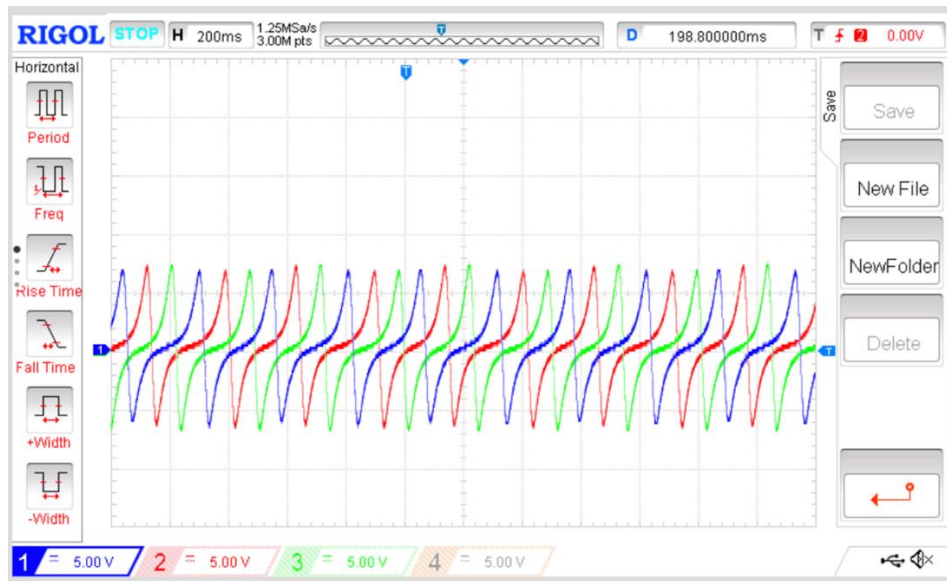


Figure 47: Sample output at 2 Hz of the outputs for cylinders A, B, and C. Each output has a 60 degree phase difference.

All Six Cylinder Outputs with no Rectifier or Smoothing

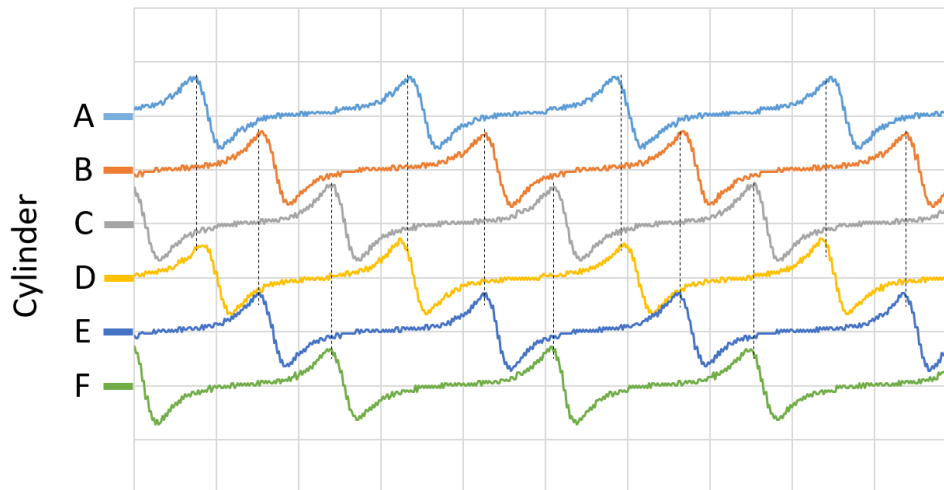


Figure 48: Sample output of all six cylinders together. Dashed lines indicated the in phase alignment for cylinders pairs: A and D, B and E, C and F. Vertical adjustment for each output does not represent amplitude. Each output's vertical adjustment is for visual clarity only.

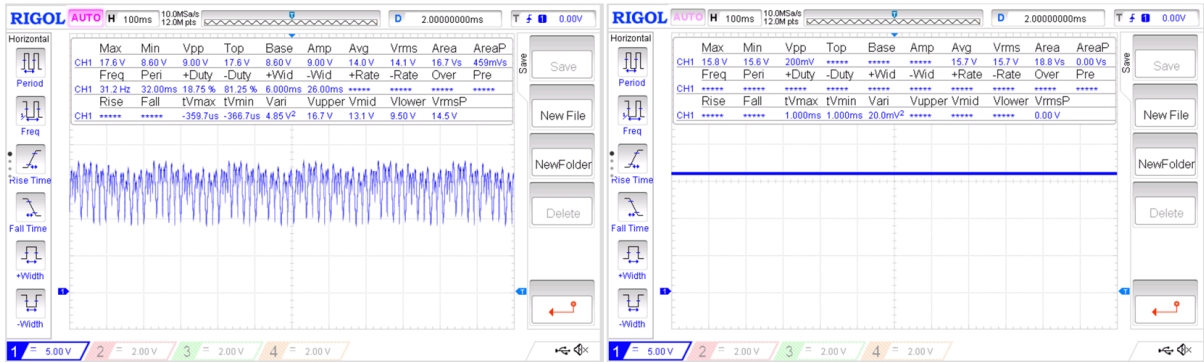


Figure 49: Sample output of all six cylinders under no load. Left image post rectifier at 6 Hz. Right image has 470 μF smoothing capacitor.

Table 6 represents the output of the system when introducing each cylinder. As each cylinder is added, the average and rms value converge. However, as seen in Figure 49, the output still has measurable variance peak-to-peak. Once a smoothing capacitor as added in the last row of Table 6, and the right image in Figure 49 the output represents a flat DC voltage output.

Table 6: Voltage output at 5 Hz under no load. A smoothing capacitor is added to the system to compare with all six cylinders.

Number of Cylinders	V_{avg}	V_{rms}	Smoothing Capacitor
1	4.60	6.86	No
2	8.54	9.91	No
3	11.20	11.50	No
4	11.90	11.80	No
5	12.50	13.30	No
6	13.30	13.40	No
6	15.00	15.00	Yes: 470 μF

Figure 50 indicates that the maximum power transfer occurs near 300 ohms at frequencies 2, 4, 6, and 8 Hz. Table 7 compares open circuit voltages at no load open circuit and with loads of 305 and 997 ohms. In addition, Table 7 outlines the transfer of ambient speeds to rotational frequency of the harvesters' fan blades. Although the harvester does allow for blade rotation under wind speeds as low as 2.3 m/s, when applying a load, the lowest operational wind speed was 2.4 m/s with a power output of 1.2 mW and a load of 305 ohms. At wind speeds of 4.9 m/s, the device's power output was 421.9 mW with a load of 305 ohms. Additionally, when applying a load to the device at higher wind speeds, the rotational frequency drops significantly. For example, at wind speeds of 4.9 m/s the no load rotational frequency was 8.41 Hz. Adding loads of 305 and 997 ohms reduces the rotational frequency to 7.25 and 7.8 respectively.

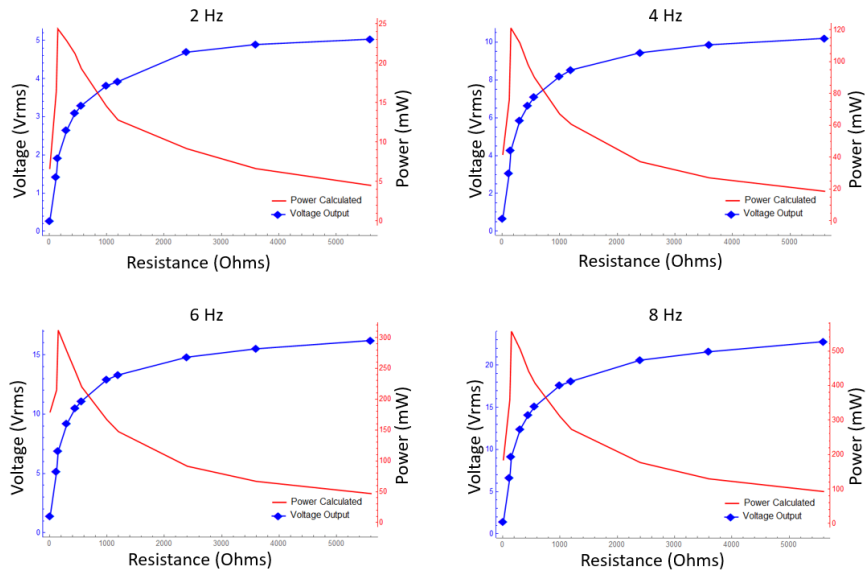


Figure 50: Voltage and power output for six cylinder output, rectifier, and smoothing capacitor over test loads ranging 10 Ohms to 5.6k Ohms and at frequencies 2, 4, 6, and 8 Hz.

Table 7: Output of harvester with all six cylinders and powered by ambient wind under no load, an optimized load of 305 Ohm, and a non-optimized load of 997 ohm.

		Ambient Wind Speed (m/s)					
		2.4	2.8	3.6	4.1	4.5	4.9
No Load (Open Circuit)	Rotational Frequency (Hz)	0.55	1.76	3.18	5.51	8.08	8.41
	Voltage Output (V)	2.6	5.62	10.7	18.2	28.2	29.0
Optimized Load (305 Ohm)	Rotational Frequency (Hz)	0.76	1.7	2.58	3.98	6.87	7.25
	Voltage Output (V_{avg})	0.611	2.32	3.84	6.11	10.8	11.4
	Power Output (mW)	1.2	17.5	47.9	121.2	378.7	421.9
Non-optimized Load (997 Ohm)	Rotational Frequency (Hz)	0.73	1.82	3.08	4.4	7.51	7.8
	Voltage Output (V_{avg})	0.741	3.36	5.63	9.23	15.7	16.3
	Power Output (mW)	0.6	11.3	31.8	85.4	247.2	266.5

5.3.4 Recharging a Device

Additional testing was done using real world devices and conditions. In these tests two devices were used as the storage and application devices from Figure 28. The first device was a smart watch with a 3.7 V, 46 mAh, WL-FBT09 lithium polymer battery. The second device was a 10,000 mAh, 10.5 W power bank charger. Under controlled conditions, using a regulated motor at 6 Hz to drive rotation, the smart watch charged

from 1% to 95% in two hours and 10 minutes averaging approximately 1.4 minutes per percent of charge. Under the same regulated 6 Hz, the power bank charged 5% in approximately 5.5 hours requiring 1.1 hours per percent. At 6 Hz, the power indicator on the 5V regulator maintained a solid on state during the charging process for both devices.

Another test was conducted using a household fan to provide a constant velocity wind source to drive the harvester. In this test, the wind speed was set to a gentle breeze of 5.3 m/s, which was near the maximum range of a level three Beaufort number. With the smart watch charging, the rotational frequency was 5.45 Hz and the charging time was approximately 4.6 minutes per percent of charge. While charging the power bank, the rotational frequency was 6.01 Hz and the charging time was approximately 110 minutes to per one percent of charge. While conducting this test, it was observed that lower rotational frequencies did not provide a constant output under load and resulted in the 5 V regulator's power indicator to periodically turning off and on.

A final set of tests were conducted in a non-controlled real world environment using near surface measurements of less than 1 m. During these tests, we placed the harvester outside and connected it to a load. In the first test, a smart watch was used as the load. During testing, the ambient wind speed was measured every 10 seconds over a 10-minute window as seen in Figure 51. Although the lack of consistency in wind speeds was not ideal, the average wind speed during testing was 2.39 m/s and the harvester was able to charge the smart watch approximately 1% every hour. During this test, it was observed that placing the smart watch on or near the harvester resulted in the vibrations created by the harvester to interfere negatively with the charging rate. The resolution was to secure the smart watch away from the harvester during charging. The second test was

conducted using an optimized load of 305 Ohm in wind speeds up to 10.1 m/s, which correlates to a Beaufort scale measurement of 5, a fresh breeze. Although the wind speeds were not consistent while testing, during measurements while the wind speeds were at 10.1 m/s, the harvester produced a power output of 1.21 W. Even if 10.1 m/s is on the upper end of the average wind speeds in the United States, several states have at or above average wind speeds near 9 m/s [78].

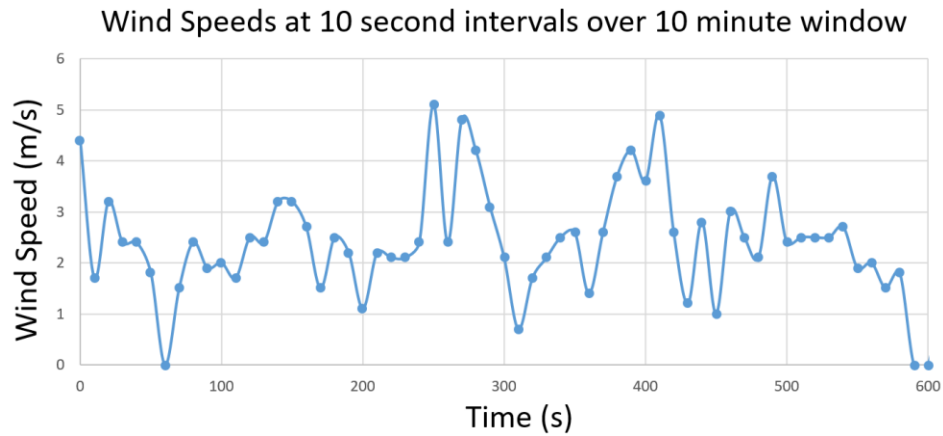


Figure 51: Outside wind speeds taken during real world test of device while charging a smart watch. Measurements taken every 10 seconds over 10 minutes. The average, maximum, and minimum wind speeds were 2.39, 5.1 and 0 m/s respectively.

5.4 Comparison to Other Small-Scale Harvesters

Due to varying sizes, design, and conversion mechanism, it is difficult to compare experimental harvesters. However, we can evaluate experimental small-scale wind driven harvesters to see their power output at various wind speeds. Table 8 presents several comparable devices along with their wind to power conversion ratios. Our device was

able to operate at low wind speeds of 2.4 under optimized load, when under these low wind speeds the normalized power output to wind speed ratio was still higher than other harvesters. As wind speeds increased, the power output and conversion ratio for the multicylinder harvester also increased. A controlled test produced 421.9 mW at wind speeds of 4.9 m/s and during the real world test with wind gust of 10.1 m/s the device hit a peak power output of 1.2 W.

Table 8: Experimental wind harvesters ranked by normalized power to wind speed ratio from lowest conversion to highest.

Experimental Design Name	Reference	Winds Speed (m/s)	Power (mW)	Normalized Power to Wind Speed Ratio	Conversion Mechanism
Vehicle-Mounted (FPEH)	[66]	18	14.5	0.209	Piezoelectric with Vibration
Vehicle-Mounted (EVEH)	[66]	18	31.8	0.221	Dynamo with Vibration
Gallopig Wind Harvester (SHPTWEH)	[68]	14	0.238	0.252	Piezoelectric – Triboelectric with Vibration
Triboelectric-Hybrid (FB-EMG)	[67]	6.96	4.23	0.467	Rotor/Stator with Rotation
Outdoor IoT Harvester	[55]	12	62	0.348	Rotor/Stator with Rotation
Small Scale Windmill	[34]	4.47	5	0.664	Piezoelectric with Vibration
V-Twin	[12]	4.1	42.2	0.793	Dynamo with Rotation
Multicylinder (low)	[Table 7]	2.4	1.2	1.003	Dynamo with Rotation
Multicylinder (Controlled Test)	[Table 7]	4.9	421.9	1.459	Dynamo with Rotation
Multicylinder (Real World Test)	N/A	10.1	1,210	1.681	Dynamo with Rotation

CHAPTER 6

COMPARISON OF ENERGY HARVESTERS

6.1 Single Crank-Slider Compared to Rotor Stator

When evaluating the output of a single-crank slider compared to a similar rotor stator, the crank-slider had lower peak-to-peak voltages and higher rms voltage. This allows the crank-slider design to use a smaller wire gauge without experiencing failure due to over current during the peak voltage moments.

6.2 Comparable Experimental Harvesters

With the various experimental harvesters employing different methods of measuring the dimensions of their devices and some projects lacking complete physical descriptions, it makes it difficult to have an accurate comparison. However, as seen in previous sections, for most cases we can observe their operational wind speeds, ambient input to power produced, conversion mechanism, and power density. The harvesters, which utilize piezoelectric had the poorest performances. From the piezoelectric group, the best performance was an output of 14.5 mW requiring 18 m/s ambient wind speed, with a power to wind speed ratio of only 0.81. The piezoelectric with the best conversion ratio utilized windmill vibrations and had a ratio of 1.12 with an output of 5 mW. Our harvester, which utilized rotation with dynamo, had the best performance of 1.21 W at the relatively high wind speed of 10.1 m/s resulting in a 119.8 power to wind speed ratio. Additionally, our harvester was able to operate at the very low wind speed of 2.4 m/s. Unfortunately, at this wind speed the ratio was one of the lowest at 0.5. Additionally, these harvesters can be evaluated using their power output per volume. Table 9 presents

the energy density of several experimental harvesters using both the mechanism dimensions and approximate footprint dimensions. The source material for several devices did not provide a complete set of dimensions for their harvester, however, we present a best approximation of their volume in column five of the table. In both cases, our final multicylinder design had the highest energy density.

Table 9: Experimental wind harvesters' energy density. The fourth column list energy density for the size of the conversion mechanism only, using dimensions given as a guide. The fifth column lists energy density for the entire footprint of each device. Due to some dimensional information missing, this column represents our closest approximation for volume.

Experimental Design Name	Reference	Winds Speed (m/s)	Energy Density for the electromechanical conversion mechanism only (W/m³)	Energy Density for approximate entire foot print of device (W/m³)
Galloping Wind Harvester (SHPTWEH)	[68]	14	N/A	0.22
Triboelectric-Hybrid (FB-EMG)	[67]	6.96	43.09	0.41
Outdoor IoT Harvester	[55]	12	72.1	3.29
Small Scale Windmill	[34]	4.47	5.09	0.91
Canyon Bridge (WEHS)	[69]	6.5	N/A	4.12
V-Twin	[12]	4.1	4.49	2.10
Multicylinder (Real World Test)	N/A	10.1	113.0	19.98

CHAPTER 7

CONCLUSIONS

Energy harvesting using ambient wind is a topic that is widely researched as a method to provide an alternative power source. Researchers are exploring a wide variety of energy conversion methods, each with their advantages and disadvantages. This research presents a novel method of incorporating a crank-slider mechanism as a method of converting rotational motion into electrical energy using induction. We started this project to expand magnetic density as a function of distance. In our initial study, we established a computational model utilizing COMSOL combined with kinematic and transduction formulas for a method to predict theoretical magnetic fields and harvester output. We find that there was no significant magnetic interference if the coils were separated by a distance greater than 6.35 mm.

Then we investigated two projects during this research, the V-Twin and the multicylinder harvesters. The V-Twin operates at wind speeds as low as 3.4 m/s, which produces 27.0 mW of power. The multicylinder harvester incorporated an alternative crank design, which allows multiple crank-sliders to be added to the system without increasing the depth of the harvester. Then we successfully added a rectifier, smoothing capacitor, and a 5 V regulator. It can produce power at wind speeds as low as 2.4 m/s and was tested at an upper limit speed of 10.1 m/s where the output produced was 1.2 mW and 1,210 mW respectively. The multicylinder harvester proved successful in real world applications. In one experiment we were efficiently able to convert wind energy into power with a maximum energy density of 19.98 W/m³ at real world wind speeds of 10.1

m/s. Under controlled tests, we charged two devices, a smart watch and a power bank. At a regulated wind speed of 5.3 m/s, the smart watch powered one percent charger every 4.6 minutes and the power bank took 110 minutes to increase each percent of power. Finally, in an uncontrolled real-world test under wind speeds averaging 2.39 m/s, the smart watch charged on average, one percent each hour. In a second uncontrolled real-world study and under an optimized load during a peak wind speed of 10.1 m/s, the harvester's output was 1.21 W.

This study demonstrated an innovative and effective approach for the harvesting of wind energy as a method of recharging small electronic devices. This design could easily be adapted to serve in remote or hazardous locations, for electronic sensors, or in various agricultural applications such as powering electric fences. The materials are readily available and can be easily assembled.

CHAPTER 8

FUTURE WORK

8.1 Improving Output of Each Cylinder

There are several aspects within this harvester that could be explored as methods to potentially improve the output. In this study, we only examined the output with one coil and one magnet per cylinder. This design could easily incorporate more coils per cylinder resulting in the magnet passing through multiple coils during each movement. Additionally, a study could examine the magnet, adjusting the size of the magnet, increasing the number of magnets for each cylinder, and varying the spacing between each magnet as they are added to each slider. By changing the number of coils and magnets, one study could investigate how modifying the stroke length affects the output. Another approach could reduce the wire gauge even further as a method to increase resistance and number of turns within the available space. However, during our experiments we found that wire gauges below 36 AWG were prone to damage during the manufacture of the coil.

8.2 Improving Output by Increasing the Number of Cylinders

In this study, we evaluated a single crank-slider harvester, a V-Twin version that incorporates two crank-sliders, and a multicylinder harvester having six total cylinders. As expected, when we increased the number of cylinders, the output also increased. The current design can be easily adapted to double the number of cylinders to a total of twelve that are all on the same plane using the current modified crank slider. In addition, additional modified crank-sliders could be added by connecting them to the exiting crank

portion from the first crank-slider. The additional crank-slider would have its own set of cylinders. While adding additional cylinders, another study could investigate how the magnets may interfere with each other by either attraction forces or changing fields interacting with nearby cylinders.

8.3 Design Change Using the Crank-Slider

In this research, the crank-sliders and cylinders are all oriented in a circle around the crank. This creates a large surface area from the components directly behind the fan, which ultimately restricts the ability of air to flow through the system. While using the crank-slider conversion mechanism, a design change could have all cylinders in a row directly behind each other. This would result in a much smaller area of resistance behind the fan and may possibly improve the wind to power conversion.

8.4 Computational Prediction

The COMSOL modeling used in this research could be expanded to include model prediction. This would allow multiple coil and magnet design configurations to be analyzed without expending time, energy, and materials on under optimized designs.

REFERENCES

1. Rovers, M. E. (2021). Rover energy. NASA. Retrieved from [https://mars.nasa.gov/mer/mission/rover/energy/#:~:text=They%20look%20almost%20like%20%22wings,in%20a%20home\)%20to%20drive.](https://mars.nasa.gov/mer/mission/rover/energy/#:~:text=They%20look%20almost%20like%20%22wings,in%20a%20home)%20to%20drive.)
2. Science, N. (2021). Mars 2020 mission perseverance rover. NASA. Retrieved from <https://mars.nasa.gov/mars2020/spacecraft/rover/electrical-power/>
3. Liu, H., Fu, H., Sun, L., Lee, C., & Yeatman, E. M. (2021). Hybrid energy harvesting technology: From materials, structural design, system integration to applications. *Renewable and sustainable energy reviews*, 137, 110473.
4. Zheng, H., Zi, Y., He, X., Guo, H., Lai, Y. C., Wang, J., ... & Wang, Z. L. (2018). Concurrent harvesting of ambient energy by hybrid nanogenerators for wearable self-powered systems and active remote sensing. *ACS applied materials & interfaces*, 10(17), 14708-14715.
5. Energy harvesting. (2021). Wikipedia. Retrieved from https://en.wikipedia.org/wiki/Energy_harvesting
6. Khan, F.U.; Ahmad, I. Review of Energy Harvesters Utilizing Bridge Vibrations. *Shock Vib.* 2016, 2016, 1340402.
7. Roundy, S. On the Effectiveness of Vibration-based Energy Harvesting. *J. Intell. Mater. Syst. Struct.* 2005, 16, 809–823.
8. Dutta, M.; Shrimoyee, P. Footstep voltage generator using piezo-electric transducers. *Int. J. Sci. Eng. Res.* 2017, 8, 117–120.

9. Crovetto, A.; Wang, F.; Hansen, O. Modeling and Optimization of an Electrostatic Energy Harvesting Device. *J. Microelectromech. Syst.* 2014, 23, 1141–1155.
10. Vidal, J. V., Turutin, A. V., Kubasov, I. V., Kislyuk, A. M., Kiselev, D. A., Malinkovich, M. D., ... & Kholkin, A. L. (2020). Dual vibration and magnetic energy harvesting with bidomain LiNbO₃-based composite. *IEEE Transactions on Ultrasonics, Ferroelectrics, and Frequency Control*, 67(6), 1219-1229.
11. Annapureddy, V.; Palneedi, H.; Hwang, G.T.; Peddigari, M.; Jeong, D.Y.; Yoon, W.H.; Kim, K.H.; Ryu, J. Magnetic energy harvesting with magnetoelectrics: An emerging technology for self-powered autonomous systems. *Sustain. Energy Fuels* 2017, 1, 2039–2052.
12. Farzidayeri, J., & Bedekar, V. (2022). Design of a V-Twin with Crank-Slider Mechanism Wind Energy Harvester Using Faraday's Law of Electromagnetic Induction for Powering Small Scale Electronic Devices. *Energies*, 15(17), 6215.
13. Hamid, Rawnak, and Mehmet Rasit Yuce. "A wearable energy harvester unit using piezoelectric–electromagnetic hybrid technique." *Sensors and Actuators A: Physical* 257 (2017): 198-207.
14. Itoh, G., Tashiro, K., Wakiwaka, H., Kumada, T., & Okishima, K. (2017, September). Prototype of magnetic energy harvesting device as a 3.3 V battery. In *2017 11th International Symposium on Linear Drives for Industry Applications (LDIA)* (pp. 1-4). IEEE.
15. Soares dos Santos, M. P., Ferreira, J. A., Simões, J. A., Pascoal, R., Torrão, J., Xue, X., & Furlani, E. P. (2016). Magnetic levitation-based electromagnetic

energy harvesting: a semi-analytical non-linear model for energy transduction. *Scientific reports*, 6(1), 18579.

16. Zhou, W., Liu, Z., Huang, Q., Jiang, Y., & Cong, Z. (2019, December). Design of Magnetic Cores for Current Transformer energy harvesting devices. In *2019 IEEE PES Asia-Pacific Power and Energy Engineering Conference (APPEEC)* (pp. 1-5). IEEE.
17. Yuan, S., Huang, Y., Zhou, J., Xu, Q., Song, C., & Yuan, G. (2017). A high-efficiency helical core for magnetic field energy harvesting. *IEEE Transactions on Power Electronics*, 32(7), 5365-5376. doi: 10.1109/TPEL.2016.2610323
18. Bedekar, V., Oliver, J., & Priya, S. (2009). Pen harvester for powering a pulse rate sensor. *Journal of Physics D: Applied Physics*, 42(10), 105105.
19. Mann, B. P., & Sims, N. D. (2009). Energy harvesting from the nonlinear oscillations of magnetic levitation. *Journal of sound and vibration*, 319(1-2), 515-530.
20. Rinard, G. A., Quine, R. W., Eaton, G. R., Eaton, S. S., Barth, E. D., Pelizzari, C. A., & Halpern, H. J. (2002). Magnet and gradient coil system for low-field epr imaging. *Concepts in Magnetic Resonance: An Educational Journal*, 15(1), 51–58.
21. Sasada, I., & Nakashima, Y. (2006). Planar coil system consisting of three coil pairs for producing a uniform magnetic field. *Journal of applied physics*, 99(8), 08D904.
22. Rovang, D., Lamppa, D., Cuneo, M., Owen, A., McKenney, J., Johnson, D., . . . others (2014). Pulsed-coil magnet systems for applying uniform 10–30 t fields to

- centimeter-scale targets on sandia's z facility. *Review of Scientific Instruments*, 85(12), 124701.
23. Tu, Y.-T., & Yeh, S.-J. (Aug. 30, 2005). Linear electric generator having an improved magnet and coil structure, and method of manufacture (Nos. US6,936,937B2). United States Patent.
 24. Ries, G. (Feb. 6, 2007). Magnet coil system for contactless movement of a magnetic body in a working space (Nos. US7,173,507B2). United States Patent.
 25. Modi, A., Singh, R., Chavan, V., Kukreja, K., Ghode, S., Manwar, K., & Kazi, F. (2016). Hexagonal coil systems for uniform magnetic field generation. In 2016 IEEE Asia-Pacific conference on applied electromagnetics (APACE) (pp. 47–51).
 26. Coey, J. (2002). Permanent magnet applications. *Journal of Magnetism and Magnetic Materials*, 248(3), 441-456. Ret
 27. Wahlström, N., Kok, M., Schön, T. B., & Gustafsson, F. (2013). Modeling magnetic fields using gaussian processes. In 2013 IEEE international conference on acoustics, speech and signal processing (p. 3522-3526). doi: 10.1109/ICASSP.2013.6638313
 28. Proca, A. B., Keyhani, A., El-Antably, A., Wenzhe Lu, & Min Dai. (2003). Analytical model for permanent magnet motors with surface mounted magnets. *IEEE Transactions on Energy Conversion*, 18(3), 386-391. doi: 10.1109/TEC.2003.815829
 29. Patel, Meet, et al. "To Utilize Vehicle Heat and Exhaust Energy." *IRJET* (2019) V6 Issue 4.

30. Metalia, N. S., & Khandwala, D. (2017). Power Generation from Dance Floor. *International Journal of Engineering Research and Technology*, 6(04), 853-856.
31. U.S. EIA (U.S. Energy Information Administration). *Independent Statistics and Analysis*; U.S. EIA: Washington, DC, USA, 2022.
32. BP Plc. *bp Statistical Review of World Energy 2020*; Addison-Wesley: London, UK, 2020.
33. Kiziroglou, M.; Yeatman, E. 17—Materials and techniques for energy harvesting. In *Functional Materials for Sustainable Energy Applications*; Kilner, J.A., Skinner, S.J., Irvine, S.J., Edwards, P.P., Eds.; Woodhead Publishing Series in Energy; Woodhead Publishing: Cambridge, UK, 2012; pp. 541–572.
34. Myers, R.; Vickers, M.; Kim, H.; Priya, S. Small scale windmill. *Appl. Phys. Lett.* 2007, 90, 054106.
35. Chen, W.T.; Gurdal, A.E.; Tuncdemir, S.; Gambal, J.; Chen, X.M.; Randall, C.A. Introducing an extremely high output power and high temperature piezoelectric bimorph energy harvester technology based on the ferroelectric system Bi(Me)O₃-PbTiO₃. *J. Appl. Phys.* 2020, 128, 144102.
36. Dinulovic, D.; Brooks, M.; Haug, M.; Petrovic, T. Rotational Electromagnetic Energy Harvesting System. *Phys. Procedia* 2015, 75, 1244–1251.
37. Luong, H.T.; Goo, N.S. Use of a magnetic force exciter to vibrate a piezocomposite generating element in a small-scale windmill. *Smart Mater. Struct.* 2012, 21, 025017.

38. Wang, X.; Pan, C.L.; Liu, Y.B.; Feng, Z.H. Electromagnetic resonant cavity wind energy harvester with optimized reed design and effective magnetic loop. *Sens. Actuators A Phys.* 2014, *205*, 63–71.
39. Chen, J. Barrel of Oil Equivalent (BOE). 2020. Available online: [https://www.investopedia.com/terms/b/barrelofoilequivalent.asp#:~:text=There%20are%2042%20gallons%20\(approximately,have%20slightly%20different%20energy%20equivalents](https://www.investopedia.com/terms/b/barrelofoilequivalent.asp#:~:text=There%20are%2042%20gallons%20(approximately,have%20slightly%20different%20energy%20equivalents) (accessed on 27 July 2022).
40. Cepnik, C.; Lausecker, R.; Wallrabe, U. Review on electrodynamic energy harvesters—A classification approach. *Micromachines* 2013, *4*, 168–196.
41. Shi, B.; Li, Z.; Fan, Y. Implantable energy-harvesting devices. *Adv. Mater.* 2018, *30*, 1801511.
42. Michaud, S.; Schneider, A.; Bertrand, R.; Lamon, P.; Siegwart, R.; Winnendael, M.v.; Schiele, A. SOLERO: Solar powered exploration rover. In Proceedings of the 7th ESA Workshop on Advanced Space Technologies for Robotics and Automation (ASTRA), Noordwijk, The Netherlands, 19–21 November 2002; ETH-Zürich: Zurich, Switzerland, 2002.
43. Lamarre, O.; Kelly, J. Overcoming the challenges of solar rover autonomy: Enabling long-duration planetary navigation. *arXiv* 2018, arXiv:1805.05451.
44. Landis, G.A. Exploring mars with solar-powered rovers. In Proceedings of the Conference Record of the Thirty-First IEEE Photovoltaic Specialists Conference, Lake Buena Vista, FL, USA, 3–7 January 2005; IEEE: New York, NY, USA, 2005; pp. 858–861.

45. Zhao, L.C.; Zou, H.X.; Yan, G.; Liu, F.R.; Tan, T.; Wei, K.X.; Zhang, W.M. Magnetic coupling and flextensional amplification mechanisms for high-robustness ambient wind energy harvesting. *Energy Convers. Manag.* 2019, *201*, 112166.
46. Izadgoshasb, I.; Lim, Y.Y.; Vasquez Padilla, R.; Sedighi, M.; Novak, J.P. Performance enhancement of a multiresonant piezoelectric energy harvester for low frequency vibrations. *Energies* 2019, *12*, 2770.
47. Fan, K.; Qu, H.; Wu, Y.; Wen, T.; Wang, F. Design and development of a rotational energy harvester for ultralow frequency vibrations and irregular human motions. *Renew. Energy* 2020, *156*, 1028–1039.
48. Li, X.; Meng, J.; Yang, C.; Zhang, H.; Zhang, L.; Song, R. A magnetically coupled electromagnetic energy harvester with low operating frequency for human body kinetic energy. *Micromachines* 2021, *12*, 1300.
49. Tang, X.; Zuo, L. Simulation and experiment validation of simultaneous vibration control and energy harvesting from buildings using tuned mass dampers. In Proceedings of the 2011 American Control Conference, San Francisco, CA, USA, 29 June–1 July 2011; IEEE: New York, NY, USA, 2011; pp. 3134–3139.
50. Sato, M.; Takemura, T.; Mizuno, T. Voltage Improvement of a Swing-Magnet-Type Generator for Harvesting Bicycle Vibrations. *Energies* 2022, *15*, 4630.
51. National Geographic Society (NGS). *Wind Energy*; NGS: Washington, DC, USA, 2022.
52. Contreras Montoya, L.T.; Hayyani, M.Y.; Issa, M.; Ilinca, A.; Ibrahim, H.; Rezkallah, M. 8—Wind power plant planning and modeling. In *Hybrid*

- Renewable Energy Systems and Microgrids*; Kabalci, E., Ed.; Academic Press: Cambridge, MA, USA, 2021; pp. 259–312.
53. Hyams, M. Wind energy in the built environment. In *Metropolitan Sustainability*; Elsevier: Amsterdam, The Netherlands, 2012; pp. 457–499.
 54. Appadurai, M.; Raj, E.F.I. Finite Element Analysis of Composite Wind Turbine Blades. In Proceedings of the 2021 7th International Conference on Electrical Energy Systems (ICEES), Virtual, 11–13 February 2021; pp. 585–589.
 55. Fang, Y.; Tang, T.; Li, Y.; Hou, C.; Wen, F.; Yang, Z.; Chen, T.; Sun, L.; Liu, H.; Lee, C. A high-performance triboelectric-electromagnetic hybrid wind energy harvester based on rotational tapered rollers aiming at outdoor IoT applications. *iScience* 2021, 24, 102300.
 56. Pozo, B.; Gárate, J.; Araujo, J.; Ferreiro, S. Energy Harvesting Technologies and Equivalent Electronic Structural Models—Review. *Electronics* 2019, 8, 486.
 57. Pozo, B.; Araujo, J.; Zessin, H.; Mateu, L.; Gárate, J.; Spies, P. Mini Wind Harvester and a Low Power Three-Phase AC/DC Converter to Power IoT Devices: Analysis, Simulation, Test and Design. *Appl. Sci.* 2020, 10, 6347.
 58. Narolia, T.; Gupta, V.; Parinov, I. Design and analysis of a shear mode piezoelectric energy harvester for rotational motion system. *J. Adv. Dielectr.* 2020, 10, 2050008.
 59. Shigley, J.E. *Series in Mechanical Engineering*; McGraw Hill Book Company Inc.: New York, NY, USA, 1961.

60. McCaslin, S.; Brown, F. Slider and Crank Mechanism. 2010. Available online: <https://demonstrations.wolfram.com/SliderAndCrankMechanism/> (accessed on 27 July 2022).
61. Saha, C.R.; O'Donnell, T.; Loder, H.; Beeby, S.; Tudor, J. Optimization of an electromagnetic energy harvesting device. *IEEE Trans. Magn.* 2006, *42*, 3509–3511.
62. Xu, Z.; Shan, X.; Chen, D.; Xie, T. A novel tunable multi-frequency hybrid vibration energy harvester using piezoelectric and electromagnetic conversion mechanisms. *Appl. Sci.* 2016, *6*, 10.
63. Teja, R. Wire Gauge Chart | American Wire Gauge (AWG) Wire Size Chart. 2021. Available online: <https://www.electronicshub.org/wire-gauge-chart/> (accessed on 27 July 2022).
64. Chen, J.; Hu, W.; Cao, D.; Zhang, B.; Huang, Q.; Chen, Z.; Blaabjerg, F. An imbalance fault detection algorithm for variable-speed wind turbines: A deep learning approach. *Energies* 2019, *12*, 2764.
65. Peigney, M.; Siegert, D. Low-frequency electromagnetic energy harvesting from highway bridge vibrations. *J. Bridge Eng.* 2020, *25*, 04020056.
66. Li, X.; Li, Z.; Bi, C.; Liu, B.; Su, Y. Study on wind energy harvesting effect of a vehicle-mounted piezo-electromagnetic hybrid energy harvester. *IEEE Access* 2020, *8*, 167631–167646.
67. Ye, C.; Dong, K.; An, J.; Yi, J.; Peng, X.; Ning, C.; Wang, Z.L. A triboelectric–electromagnetic hybrid nanogenerator with broadband working range for wind

- energy harvesting and a self-powered wind speed sensor. *ACS Energy Lett.* 2021, 6, 1443–1452.
68. Wang, Q.; Zou, H.X.; Zhao, L.C.; Li, M.; Wei, K.X.; Huang, L.P.; Zhang, W.M. A synergetic hybrid mechanism of piezoelectric and triboelectric for galloping wind energy harvesting. *Appl. Phys. Lett.* 2020, 117, 043902.
 69. Cao, H.; Wu, X.; Wu, H.; Pan, Y.; Luo, D.; Azam, A.; Zhang, Z. A Hybrid Self-Powered System Based on Wind Energy Harvesting for Low-Power Sensors on Canyon Bridges. *Int. J. Precis. Eng. Manuf. -Green Technol.* 2022.
 70. Tran, Bang, et al. "Solar-Powered Convenient Charging Station for Mobile Devices with Wireless Charging Capability." *WSEAS Transactions on Systems* 20 (2021): 260-271.
 71. Biswas, Prosenjit, et al. "Portable self-powered piezoelectric nanogenerator and self-charging photo-power pack using in situ formed multifunctional calcium phosphate nanorod-doped PVDF films." *Langmuir* 35.52 (2019): 17016-17026.
 72. Luo, Jianjun, and Zhong Lin Wang. "Recent advances in triboelectric nanogenerator based self-charging power systems." *Energy Storage Materials* 23 (2019): 617-628.
 73. Sharma, Himanshu, Ahteshamul Haque, and Zainul Abidin Jaffery. "Maximization of wireless sensor network lifetime using solar energy harvesting for smart agriculture monitoring." *Ad Hoc Networks* 94 (2019): 101966.
 74. Newell, David, and Maeve Duffy. "Review of power conversion and energy management for low-power, low-voltage energy harvesting powered wireless sensors." *IEEE Transactions on Power Electronics* 34.10 (2019): 9794-9805.

75. J. Huang, Y. Zhou, Z. Ning and H. Gharavi, "Wireless Power Transfer and Energy Harvesting: Current Status and Future Prospects," in *IEEE Wireless Communications*, vol. 26, no. 4, pp. 163-169, August 2019, doi: 10.1109/MWC.2019.1800378.
76. Majhi, Sanjit Manohar, et al. "Recent advances in energy-saving chemiresistive gas sensors: A review." *Nano Energy* 79 (2021): 105369.
77. Ahmad, Muhammad Masood, and Farid Ullah Khan. "Review of vibration-based electromagnetic–piezoelectric hybrid energy harvesters." *International Journal of Energy Research* 45.4 (2021): 5058-5097.
78. *USA Location Information*. USA.com. (n.d.). Retrieved 2023, from <http://www.usa.com/>